# Inaugural-Dissertation

zur
Erlangung der Doktorwürde

der
Naturwissenschaftlich-Mathematischen
Gesamtfakultät

der
Ruprecht-Karls-Universität
Heidelberg

vorgelegt von
Dipl.-Phys. Stefan Funk
aus Heidelberg

Tag der mündlichen Prüfung: 6. Juli 2005

# A new population of very high-energy $\gamma$-ray sources detected with H.E.S.S. in the inner part of the Milky Way

Gutachter: Prof. Dr. Werner Hofmann
Prof. Dr. Stefan Wagner

# Abstract

The H.E.S.S. experiment (High Energy Stereoscopic System) is an array of four imaging Cherenkov telescopes designed to detect $\gamma$-rays in the energy domain above 100 GeV. The telescopes utilise the stereoscopic approach, in which particle showers in the atmosphere are observed by several telescopes simultaneously, connected by a central trigger system at the hardware level. This approach greatly reduces the background of the instrument and thereby allows one to decrease the energy threshold and improve the sensitivity of the system. The functionality and performance of the central trigger of H.E.S.S. is presented. Making use of the reduced energy threshold and the improved sensitivity, a survey of the inner part of the Milky way in very high energy $\gamma$-rays was conducted in 2004 with H.E.S.S. at an unprecedented sensitivity level. The Galactic plane between $\pm 30^\circ$ in longitude and $\pm 3^\circ$ in latitude relative to the Galactic centre was observed for a total of 230 hours, reaching an average flux sensitivity of 3% of the Crab nebula at energies above 200 GeV. Fourteen new sources were detected at a significance level greater than $4\sigma$ in addition to three previously known sources in this area. Detailed spectral and morphological information for these new sources are provided, along with a discussion on possible counterparts in other wavelength bands. The distribution in galactic latitude of the detected sources appears to be consistent with a scale height in the galactic disc for the parent population of less than 100 parsec.



# Kurzfassung

Das H.E.S.S. Experiment besteht aus einem stereoskopischen System von vier Teleskopen. Ziel des Experiments ist die Untersuchung von Quellen hochenergetischer kosmischer $\gamma$-Strahlung im Energiebereich oberhalb von 100 GeV. Die eingesetzte Technik beruht auf der stereoskopischen Beobachtung von Luftschauern mit mehreren Teleskopen. Dazu werden die Teleskope bereits auf dem Triggerlevel durch einen zentralen Trigger miteinander verschaltet. Durch den Einsatz dieses zentralen Triggers werden Untergrundereignisse massiv unterdrückt, wodurch es möglich ist, die Energieschwelle zu senken und die Sensitivität zu erhöhen. Funktionsweise und Messungen zur Charakterisierung des zentralen Triggersystems werden vorgestellt. Unter Zuhilfenahme der reduzierten Energieschwelle und erhöhten Sensitivität wurde eine Durchmusterung der Galaktischen Ebene im Sommer 2004 durchgeführt. Hierbei wurde der Bereich $\pm$ 30°in galaktischer Länge und $\pm$ 3°in galaktischer Breite um das Zentrum der Milchstrasse 230 Stunden lang nach Quellen hochenergetischer $\gamma$-Strahlung abgesucht. Die durchschnittliche Sensitivität die hierbei erreicht wurde entspricht etwa 3% des Flusses des Krebs-Nebels oberhalb der Energieschwelle von 200 GeV. Vierzehn neue Quellen hochenergetischer $\gamma$-Strahlung wurden oberhalb einer Signifikanzschwelle von $4\sigma$ detektiert. Detaillierte spektrale und morpholgische Untersuchungen dieser neuen Quellen werden vorgestellt, gefolgt von einer Diskussion möglicher Gegenstücke in anderen Wellenlängenbereichen. Es wird gezeigt, dass die Verteilung der neuen Quellen in galaktischer Breite mit einer Population von Supernovaüberresten mit Skalenhöhe von 100 pc der galaktischen Ebene konsistent ist.

# Contents

# List of Figures

# Chapter 1

# Introduction

Astronomy is probably the oldest of the natural sciences with origins in the religious practices of pre-history. Early astronomy involved observing and predicting the motions of visible celestial objects, especially stars and planets. Later, the Chinese started to keep records of *guest stars*, objects that are normally too faint to be seen but suddenly flare up and become visible for a period of time. One of the most prominent of these observations was the guest star of 1054 in the constellation of Taurus which was visible for 23 days even in daylight. It was later found to be caused by the Crab Supernova. Another striking features visible to the naked eye at night is the band of faint white light stretching along the sky (see Figure 1.1). The ancient Romans called this band *Via Galactica* (road made of milk), hence the origin of the name - Milky way. As interest in astronomy grew, it became apparent, that most potential objects of study were barely visible to the naked eye. In 1609 Galileo became the first person to use an instrument to observe the sky. After constructing a 20x refractor telescope he found that the Milky Way was composed of individual stars. The disk shape of the Galaxy to which our Sun belongs was demonstrated in 1785 by William Herschel, who used a telescope to count the number of stars visible at night. He found that the number of stars were similar in any direction around the Milky Way. This result prompted him to assume that we are located near the centre of the Galaxy. We know now, however, that this conclusion is wrong, since interstellar dust absorbs the light from stars and restricts optical observations in the plane of the Milky Way. Therefore Herschel was able to observe only a tiny fraction of the system of stars surrounding us.

With modern instrumentation, astronomers can conduct observations of the Milky Way in radio and infrared wavebands, at which the electromagnetic radiation penetrates the

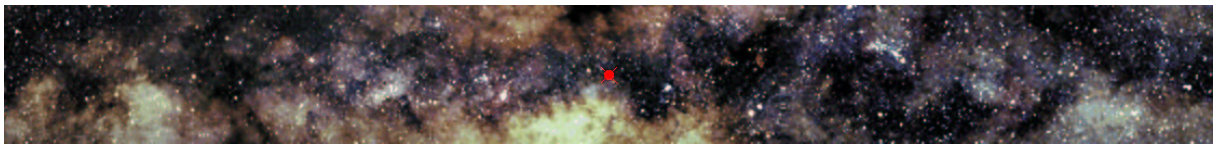

**Figure 1.1:** An optical view on the Milky Way in a band of $\pm$ 35° in longitude and $\pm$ 4° in latitude around the centre of the Galaxy. The red marker denotes the position of the Galactic Centre.

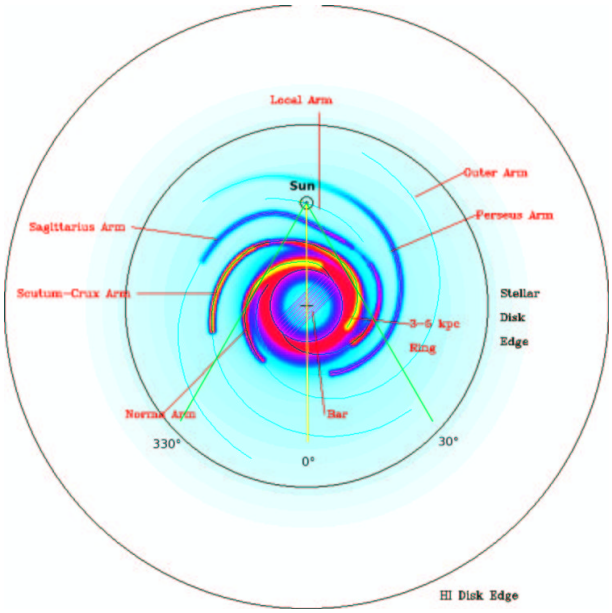


**Figure 1.2:** Schematic top view on the Milky Way from CGPS (2005).

interstellar dust. On the basis of these measurements, the Galaxy was found to be a thin circular disk of luminous matter distributed across a region of about 30000 parsec (pc) in diameter (1 pc = 3 light years), with a thickness of less than 200 pc. Our Sun was found to be located in one of the outer arms of our Galaxy which was, in total, made up by more than $10^{10}$ stars. Although the Sun lies far from the Galactic Centre, the main disk of the Galaxy extends nearly the same distance again beyond the Sun as can be seen from the schematic top view of the Galaxy in Figure 1.2.
Near the middle of the 20th century, astronomy moved to the forefront of science. Dramatic advances were spurred to a large part by the opening of new windows in the electromagnetic spectrum that are invisible to the human eye: radio waves, X-Rays, $\gamma$-rays to name a few. In 1931 radio astronomy had its beginnings, and in the late 1960s, astronomers began to use the new tool of space flight to reach UV, X-ray and other wavebands blocked by the Earth's atmosphere. In the last four decades our vision, formerly sensitive only to visible light, has broadened to encompass the entire electromagnetic spectrum.

## 1.1 Very High Energy $\gamma$-rays

The evolving astronomical discipline of $\gamma$-ray-astronomy invokes the detection of light of astronomical objects in photon energies up to $10^9$ times more energetic than visual light. This branch of modern astrophysics plays a crucial role in the exploration of non-thermal phenomena in the Universe within their most violent forms. $\gamma$-rays cover at least a range of 14 decades in energy between $\sim 0.5 \times 10^6$ eV and $\sim 10^{20}$ eV. This range is covered rather inhomogenuously by completely different detection methods and flux sensitivities. *Soft* $\gamma$-rays up to 15 MeV are observable by satellite instruments like the

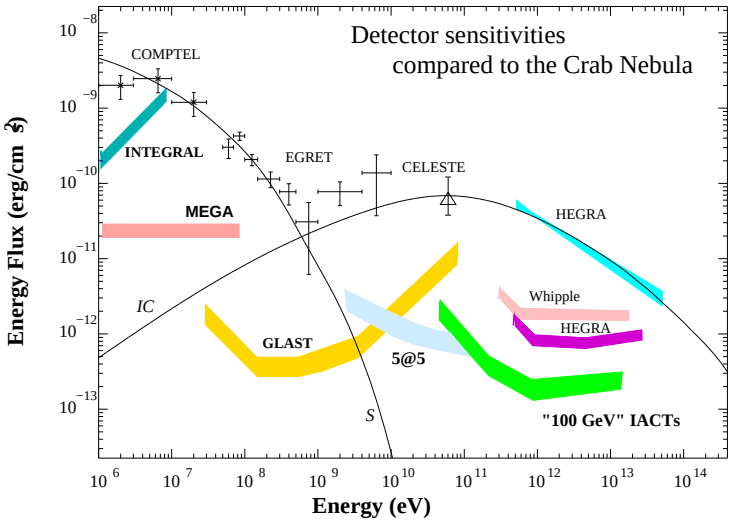


**Figure 1.3:** Energy flux sensitivities of *soft* $\gamma$-ray satellites like INTEGRAL, *hard* $\gamma$-ray satellites like EGRET and GLAST shown together with flux sensitivities of ground-based detectors like HEGRA, Whipple and the third generation of *"100 GeV"* telescopes. For comparison the predicted synchrotron (S) and inverse Compton (IC) fluxes as well as the reported $\gamma$-ray fluxes from the Crab Nebula are shown.

INTErnational Gamma-Ray Astrophysics Laboratory (INTEGRAL). *High* energy $\gamma$-rays between 30 MeV and 30 GeV can be detected by space-borne instruments like the Energetic Gamma Ray Experiment Telescope (EGRET). Future satellite missions like the Gamma-ray Large Area Space Telescope (GLAST) will extend this range even further up to $\sim$ 100 GeV. Beyond this energy, the area limitation of space-borne detectors compels the region of *very high energy* (VHE) $\gamma$-rays above 100 GeV to remain the domain of ground based astronomy. Figure 1.3 shows the detector sensitivities of different instruments, including future missions like GLAST and high-altitude ground based telescopes like 5@5 in comparison to the predicted and detected flux from the Crab Nebula (taken from Aharonian (2004)).

### 1.1.1 Production Mechanisms of VHE $\gamma$-rays

Thermal radiation of astrophysical objects for typical surface temperatures $\sim$ 5000 K is, according to Planck's radiation law, generated in visible light. For the hottest objects observed in the universe, e.g. in accretion discs around compact stars, the thermal radiation may be as energetic as X-rays in the range up to 10 keV. This is still several orders of magnitudes below the VHE $\gamma$-ray-range and therefore it is evident that non-thermal processes must be involved in the generation of VHE $\gamma$-rays. The acceleration of electrons or nuclei in astrophysical sources leads inevitably to the production of $\gamma$-rays, mainly by the decay of $\pi^0$s produced in hadronic interactions, or inverse Compton scattering of high energy electrons on background radiation fields. These processes are summarised in the following sections.

**Decay of neutral pions produced in hadronic interactions**

This channel provides a unique view on the hadron-induced component of VHE $\gamma$-radiation. This distinct role has been predicted by pioneers of the field such as Ginzburg & Syrovatskii (1963). Relativistic protons and nuclei create secondary pions ($\pi$) and kaons in inelastic collisions with matter. The neutral pions ($\pi^0$) decays immediately predominantly into two $\gamma$-rays and thus provide the main channel for the conversion of kinetic energy of hadrons to $\gamma$-rays. The spectral features of $\gamma$-rays produced through $pp \rightarrow \pi^0 \rightarrow 2\gamma$ has been intensively studied (see e.g. Aharonian (2004)). It was shown that in the energy range above 1 GeV the $\gamma$-ray spectrum follows closely the (power-law) spectrum of the parent protons. This implies that at high energies the $\gamma$-rays carry direct information about the acceleration spectrum of the progenitor particles. For an exhaustive overview on this topic, see Aharonian (2004)

**Inverse Compton scattering of electrons**

The interaction of relativistic electrons with radiation fields through Inverse Compton (IC) scattering is one of the most important $\gamma$-ray production processes in astrophysics. Ambient low energy photons are up-scattered by relativistic electrons or positrons to $\gamma$-ray energies. Since low energy photons are found in all astrophysical objects, IC is at work basically everywhere, in pulsars, Supernova remnants (SNRs), as well as in active galactic nuclei (AGN). Due to the presence of the ubiquitous 2.7 K cosmic microwave background radiation (CMBR) this process is very efficient also in the intergalactic medium.
Other production mechanisms like non-thermal bremsstrahlung of electrons and synchrotron radiation of ultra-high energy particles also contribute to the emission of $\gamma$-rays in astrophysical objects. For a description of these processes see Longair (1994). From the description of the generation processes described here, it is apparent relativistic particles must be present in the sources of VHE $\gamma$-rays. The next section will give a brief overview over particle acceleration mechanisms in astrophysical sources.

### 1.1.2 Acceleration of Charged Particles

The standard mechanism for effective particle acceleration in a shock front was originally proposed by Fermi in 1949 and adapted to Supernova shocks in the late 1970s by numerous authors, such as Bell (1978); Blandford & Eichler (1987). The process is generally known as first order Fermi acceleration (since it depends linearly on the flow velocity $U$). Its general principle is illustrated in Figure 1.4. A flow of relativistic charged particles hits a cloud of material at rest producing a shock front. The shock front moves at speed $U$ much smaller than the velocities of the high energy particles. Typical shock velocities are in the range of $U \sim 10^4$ km/s. The particles hardly notice the thin shock (the thickness of the shock is much smaller than the gyroradius of the particles). Due to turbulences behind the shock front and irregularities in front of it, the particles pass through the shock in either direction, and the velocity distributions on either side of the shock become isotropic. The key argument is that the distributions are isotropic with respect to the frame in which the flow is at rest on either side of the shock. The shocked material downstream follows the shock at speed $U_{\mathrm{down}} < U$ (for completely ionised material, assuming the

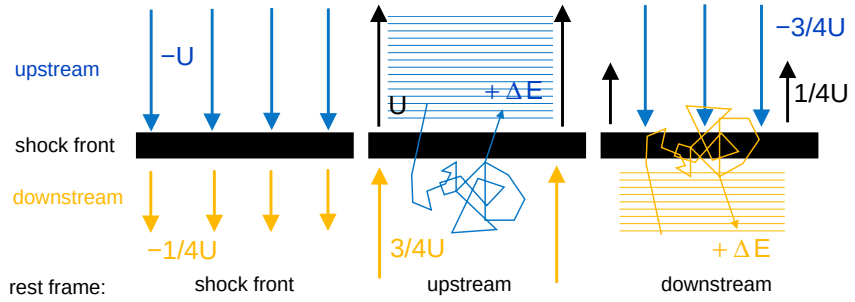


**Figure 1.4:** Illustration of the first order Fermi acceleration in a shock wave propagating with velocity $U$ into an upstream medium. **Left:** Flow of gas in the frame in which the shock front is at rest. The upstream interstellar medium moves towards the shock front with velocity $U$, the downstream medium follows (for the case of an ideal gas) with velocity $1/4U$ with respect to the shock wave. **Middle:** Rest frame of the upstream medium. The particles at rest in the upstream medium encounter gas of the downstream region advancing with velocity $3/4\ U$, get scattered by the turbulences behind the shock front become isotropic with the downstream flow and thereby gain an energy $\Delta E$. **Right:** Rest frame of the downstream medium. The velocity distribution downstream is isotropic. Particles diffusing from behind the shock front to the upstream region, encounter again gas moving towareds the shock front with velocity $3/4\ U$. Therefore the particle undergoes exactly the same process of receiving a small increase in energy $\Delta E$ when crossing the shock from downstream to upstream as it did when crossing the other way round. Every time the particle crosses the shock front it gains energy.

cloud to be an ideal gas it can be shown that $U_{\mathrm{down}} = 3/4\,U$). The shock creates plasma turbulences in the up- and down-stream region, generating magnetic inhomogeneities. The charged particles bounce off the magnetic fields and cross the shock multiple times. When viewed in the rest frame of the region (up- or down-stream ) the particle originates from, the particle diffusing into the other region gets thermalised by the flow speed of the new region and gains energy. This processes is symmetric within the rest frame of the opposite region and therefore the particle gains energy with each crossing of the shock front. The acceleration continues until the particle can escape the shock region. The net energy gain of the relativistic particle per shock crossing again under the assumption of an ideal gas can be described by:

$$\Delta E/E = \frac{2}{3}\frac{U}{c} \tag{1.1}$$

It is dependent on the energy of the particle and it can be shown that an initial monoenergetic particle spectrum evolves into a power-law spectrum $dN/dE \propto E^{-\Gamma}$ with $\Gamma = 2$. For a detailed discussion on the process of Fermi acceleration see Longair (1994).

## 1.2 Galactic Sources of VHE $\gamma$-rays

Having described the acceleration of particles and the production mechanisms of VHE $\gamma$-rays in the previous sections, known Galactic source classes of VHE $\gamma$-rays will be given in the following. Confidently detected classes of VHE $\gamma$-ray emitters in the Galaxy so far include Supernova remnants and pulsar wind nebula. These are described in the following along with the potential source class of X-ray binaries.

### 1.2.1 Supernova Remnants

In 1912 Victor Hess discovered that an electroscope discharged more rapidly as he ascended in a baloon. He attributed this effect to a source of radiation entering the atmosphere from above, cosmic rays (Hess, 1912). For this discovery he was awarded the Nobel prize in 1936. Since then a large number of experiments have precisely measured the energy spectrum and composition in different energy bands. It is well known that cosmic rays arrive isotropically from space and have an energy density of $\sim 1$ ev/cm$^{-3}$. The main component consists of protons and $\alpha$-particles. Additionally a small contribution from electrons and positrons is present, resulting in more than 99.8% of all cosmic rays being charged particles.

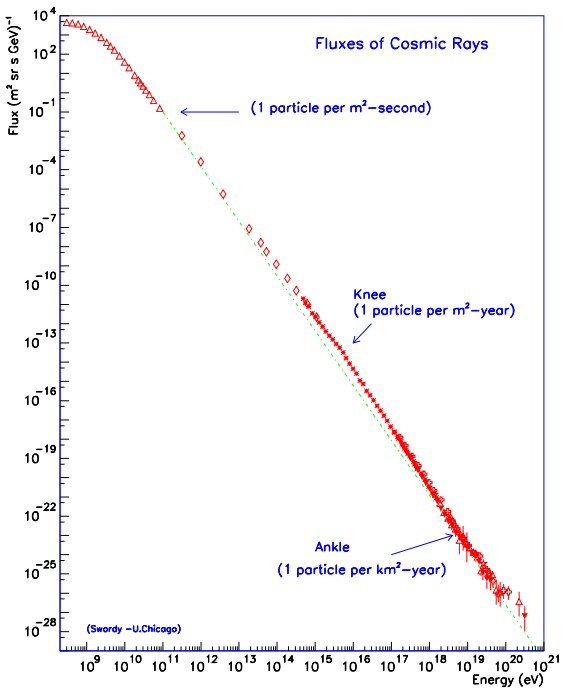


**Figure 1.5:** Energy spectrum of cosmic rays.

The energy spectrum of cosmic rays as shown in Figure 1.5 follows a nearly perfect power law over more than 10 orders of magnitude up to energies above $10^{20}$ eV. It has two distinct features, the *knee* at $10^{15}$ eV and the *ankle* at $10^{18}$ eV. The general belief is, that

cosmic rays below the knee are of galactic origin, whilst the particles above the ankle are produced outside of the disc. The following focuses on the galactic component of the cosmic radiation.

After several decades of intensive experimental and theoretical studies, knowledge about the sources of galactic cosmic rays is still rather limited. The main complication in determining the production sites and acceleration mechanism of cosmic rays arises from the diffusion of charged particles in interstellar magnetic fields. The charged component of cosmic rays lose their directional information on their way from the source to earth. Also the original source spectra of accelerated particles is significantly modified by this diffusion. Only the uncharged component of the cosmic radiation, i.e. neutrinos and $\gamma$-rays, can thus directly unveil the sites of particle acceleration.

For a long time Galactic SNRs have been considered as best candidates for the acceleration of hadronic cosmic rays up to the *knee* in the cosmic-ray particle spectrum at $\sim 10^{15}$ eV. However there is, as yet, no generally accepted evidence for the existence of energetic hadrons in these objects. SNRs are favoured as the site of cosmic-ray acceleration for two principal reasons: firstly a theoretically well established acceleration mechanism exists in the form of diffusive (first order Fermi) shock acceleration at SNR shock fronts as described in section 1.1.2 (for reviews see e.g. Blandford & Eichler (1987); Malkov & Drury (2001)), and secondly, that Galactic Supernovae and the resulting SNRs are the only known potential sources which can provide the necessary amount of energy (Ginzburg & Syrovatskii, 1963).

To explain the observed energy density of cosmic rays, Supernova explosions must convert kinetic energy in to relativistic particle energy with a conversion efficiency $\Theta$ of roughly $0.1 - 0.2$. Theoretical expectations for the $\gamma$-ray-emission of SNRs arising from hadronic interactions is given by Drury, Aharonian, & Völk (1994) as:

$$F_\gamma(> E) \approx 9 \times 10^{-11}\, \Theta \left(\frac{E}{1\ \mathrm{TeV}}\right)^{-1.1} \times\ S\,\mathrm{cm}^{-2}\mathrm{s}^{-1} \tag{1.2}$$

with

$$S = \left(\frac{E_{\mathrm{SN}}}{10^{51}\,\mathrm{erg}}\right)\left(\frac{d}{1\,\mathrm{kpc}}\right)^{-2}\left(\frac{n}{1\,\mathrm{cm}^{-3}}\right) \tag{1.3}$$

where $d$ denotes the distance to the object, $\Theta$ the conversion efficiency into kinetic energy and $E_{\mathrm{SN}}$ the total kinetic energy released by the Supernova, $n$ the density of the circumstellar medium is assumed to be uniform. This formula assumes a power-law distribution of cosmic-ray energies with a typical differential spectral index of 2.1. Calculations of the spectral index, using nonlinear kinetic theory of diffusive shock acceleration in SNRs, give a range of values around the index value 2.0 for a uniform circumstellar medium (Berezhko & Völk, 1997), and a rather more extended range of spectral index values for Supernova explosions into the wind bubble of very massive progenitor stars (Berezhko & Völk, 2002). A typical value for the amount of kinetic energy converted into cosmic rays is $\Theta\, E_{\mathrm{SN}} = 1.0\,\mathrm{to}\,2.0 \times 10^{50}$ erg (Malkov & Drury, 2001). For an SNR at a distance of $d = 1$ kpc expanding into an environment with a typical density of the interstellar medium of $n = 1$ hydrogen atom per cm$^3$, a VHE $\gamma$-ray flux similar to that from the Crab Nebula is expected. The luminosity $L_0$ of such a source is $1.3 \times 10^{34}$ erg s$^{-1}$ in the relevant energy

range between 0.2 TeV and 10 TeV. One would therefore expect that with the sensitivity level of the H.E.S.S. Galactic Plane survey (3% of the Crab flux) SNRs should be detectable out to a distance of 6 kpc (cf. 8.5 kpc to the centre of the Galaxy). For enhanced values of $n$, as for example is the case in molecular clouds, SNRs should be visible within most of the volume of the Galactic disc.
Observations of synchrotron emission in the X-ray band have provided strong evidence for the existence of $\sim$ 100 TeV electrons in shell-type SNRs, see for example Koyama et al. (1995). At TeV energies, shell-type SNRs are known to be sources of VHE $\gamma$-rays as shown by high confidence detections of the SNRs RX J1713.7-3946 and RX J0852.0-4622 (Vela Junior) by the CANGAROO (Enomoto et al., 2002; Katagiri et al., 2005) and H.E.S.S. collaborations (Aharonian et al., 2004a, 2005c). These observations provided the first direct proof of particle acceleration in SNR shock fronts. These detections, however, have not yet provided direct evidence for the existence of accelerated hadrons, since it is difficult to disentangle the relative contribution of electrons and hadrons. Extended multiwavelength data, especially in the GeV region as well as an increase in the number of TeV detected shell-type SNRs, would help to clarify the picture.

### 1.2.2 Pulsars and Plerions

Pulsars, rapidly rotating neutrons stars left over, e.g., after a Supernova explosion and their associated pulsar wind nebulae (PWN) have long been investigated as sources of VHE $\gamma$-rays (see e.g. Harding (1996); Aharonian, Atoyan, & Kifune (1997)). Pulsars are highly magnetised and act like unipolar inductors effectively emitting high energy $\gamma$-rays. The pulsar-generated outflow - the pulsar wind - interacts with the ambient medium, generating a shock region where particles are accelerated. Such objects should therefore exhibit a pulsed component of radiation - from the immediate vicinity of the pulsar - together with an unpulsed component from the shock region and beyond (commonly referred to as the *Plerion*). The detection of unpulsed emission from the Crab Nebula as the first VHE $\gamma$-ray source in 1989 by the Whipple collaboration (Weekes et al., 1989) confirmed these predictions. The Crab Nebula, as the brightest stable VHE $\gamma$-ray source, remains the best-studied object of this class of particle accelerators. The central Crab pulsar has a spin-down luminosity of $5 \times 10^{38}$ ergs s$^{-1}$ which is efficiently converted into radiation. The emission of the Crab Nebula is predominantly produced by non-thermal processes since the large magnetic field in the nebula of $B \sim 160\mu$G implies a large component of synchrotron emission. The synchrotron origin of multi-MeV photons requires the existence of relativistic electrons up to energies of $10^{16}$ eV. These PeV electrons inevitably radiate via inverse Compton scattering of the same electrons leading to VHE $\gamma$-ray radiation.

### 1.2.3 X-ray Binaries

X-ray binaries have been traditionally treated as thermal sources, transforming the gravitational energy of accretion onto a compact object into X-ray emission radiated by the hot accreting plasma. The discovery of galactic objects with relativistic jets (*micro-quasars*) revealed that non-thermal high-energy processes play an important role in these

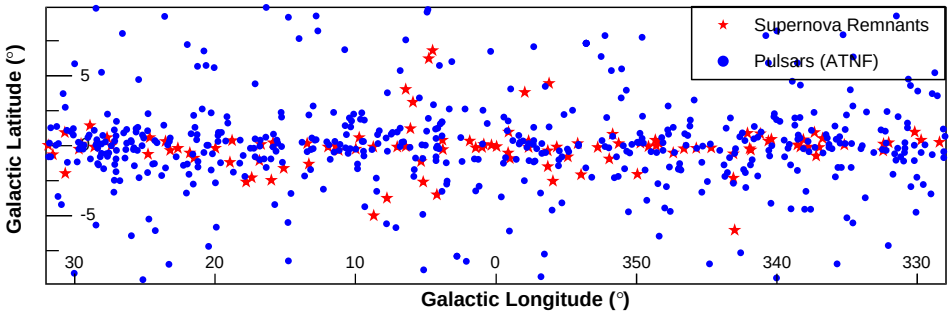


**Figure 1.6:** The distribution of Galactic SNRs and pulsars in the inner 30 degrees of the Galactic Plane.

accretion-powered objects. Models of X-ray binaries with synchrotron radio jets predict hard non-thermal X-rays produced by synchrotron radiation of ultrarelativistic multi-TeV electrons. Under certain conditions these electrons may effectively radiate VHE $\gamma$-rays through inverse Compton scattering.

## 1.3 The Milky Way in VHE $\gamma$-rays

Most of the potential galactic $\gamma$-ray sources such as SNRs and pulsars are associated with massive star formation and therefore cluster along the Galactic Plane, especially concentrated in the direction towards the centre of our Galaxy. Within an opening angle of 30°, the bulge of the Galaxy, as well as part of the Norma arm are in the line of sight (see Figure 1.2 which schematically gives a top view of the Milky Way along with the position of the Sun). In total 91 SNRs and 389 pulsars are catalogued within the inner 60° in galactic longitude and 6° in galactic latitude (Green, 2004; Manchester et al., 2005) as shown in Figure 1.6. In the following our knowledge of the Milky Way in $\gamma$-rays before the start of the H.E.S.S. instrument in 2002 is briefly summarised.
At high energy $\gamma$-rays, above 30 MeV, observations by EGRET (Hartman et al., 1999) revealed a population of sources clustering along the Galactic Plane. The only firmly identified Galactic sources detected by EGRET are pulsars (mainly identified by their characteristic pulsation period), proposed associations exist with SNRs and microquasars. However, the majority of the 271 EGRET sources summarised in the 3rd EGRET catalogue (Hartman et al., 1999), especially the ones located in the Galactic Plane, remain unidentified, mainly due to the relatively poor spatial resolution of the instrument of $\gtrsim 1°$. Figure 1.7 shows the sky as seen by EGRET above 100 MeV. The most prominent feature in this map is the broad band of diffuse emission running along the Galactic Plane presumably stemming from interaction of cosmic rays with ambient gas and photon fields. At TeV energies the Milagro water-Cherenkov detector (Atkins et al., 2004) and the Tibet air-shower array (Amenomori et al., 2002) have been used to perform large-scale surveys. Whilst these instruments have the advantage of a very wide field of view ($\sim 1$ steradian), the sensitivity reached by these surveys is rather limited, reaching a flux limit comparable to the level of the Crab Nebula, $\sim 3 \times 10^{-10}$ cm$^{-2}$ s$^{-1}$ (for $E > 200$ GeV), in one year of observations. Both surveys covered $\sim 2\pi$ sterad of the northern sky and revealed no

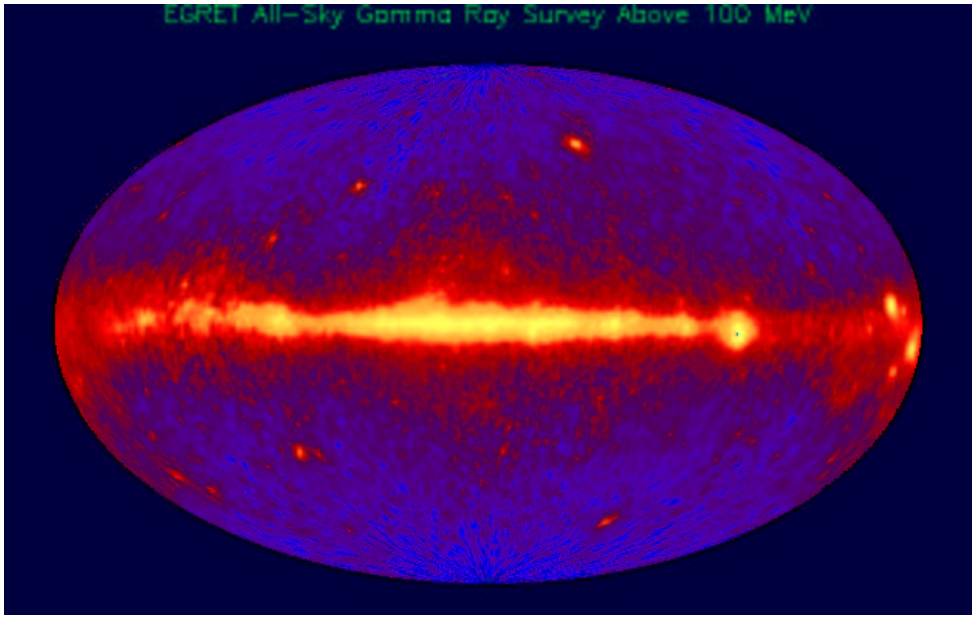


**Figure 1.7:** Universe as seen by EGRET in high energy $\gamma$-rays above 100 MeV. The diffuse band of emission along the Galactic Plane has been attributed to cosmic ray interactions with ambient gas and photon fields.

prominent $\gamma$-ray sources. However, some evidence for $\gamma$-ray emission was found by the Milagro Collaboration from a region in the Cygnus constellation and another region close to the Crab Nebula (Smith et al., 2005). Recently the detection of diffuse emission from the Galactic Plane with Milagro has been reported (Fleysher et al., 2005).
The HEGRA instrument was the first array of imaging Cherenkov telescopes to be used to survey a part of the Galactic Plane (Aharonian et al., 2002b). The range of galactic longitudes ($l$) between $-2^\circ < l < 85^\circ$ was observed. Due to the location of HEGRA in the northern hemisphere and the resulting large zenith angles for observations of the centre of the Galactic Plane the sensitivity was reduced for the central part of the Galaxy. No sources of VHE $\gamma$-rays were found in this survey, and upper limits between 15% of the Crab flux for galactic longitudes $l > 30^\circ$ and more than 30% of the Crab flux in the inner part of the Milky Way were derived.
Until the completion of the High Energy Stereoscopic System H.E.S.S. (for a description see Hinton (2004)) in early 2004, no VHE $\gamma$-ray survey of the southern sky, or of the central region of the Galaxy had been performed. The situation of VHE $\gamma$-ray astronomy before the H.E.S.S. survey is comparable with the situation of X-ray astronomy in the 1960s. The improvement in detector sensitivity mainly through the advent of space-borne satellite detectors, has rapidly increased the number of known sources. In VHE regime, despite the large number of known SNRs and pulsars in our Galaxy, the actual number of detected $\gamma$-ray sources was limited to only a handful of objects (for a review, see e.g. Weekes (2001)). Large parts of the sky remain unexplored *terra incognita* in the VHE $\gamma$-ray regime for flux sensitivities below 50% of the Crab flux. Figure 1.8 shows schematically the sources detected in the Galactic Plane before the H.E.S.S. survey. From this map it is evident, that $\gamma$-ray astronomy in our Galaxy before the completion of

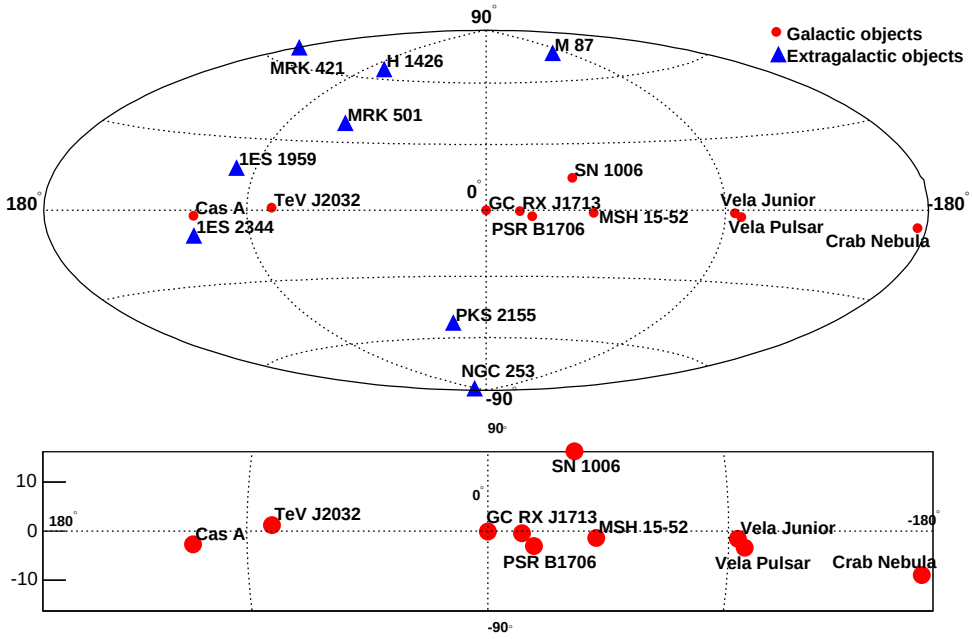


**Figure 1.8:** Known sources of VHE $\gamma$-radiation before the completion of the H.E.S.S. telescope system. In the upper panel the circles denote galactic objects whereas the triangles denote extragalactic objects. It can be seen, that only a very sparse number of known sources were present in the universe.

H.E.S.S. was an *astronomy of a few sources*.
For all these reasons a survey of the inner part of the Galaxy provides an efficient way to search for $\gamma$-ray emission in order to investigate properties of source classes and search for yet unknown types of galactic VHE $\gamma$-ray emitters. The completion of the H.E.S.S. telescope system with its large field of view of 5°, its location in the southern hemisphere and its improved sensitivity in comparison to previous instruments made it possible to conduct the first systematic sensitive survey of the inner 30° of the Galactic Plane. The results of this survey with the H.E.S.S. instrument between May and July 2004, at a flux sensitivity below 3% of the Crab flux on the Galactic Plane are described in this work. Fifteen new sources of VHE $\gamma$-rays are found at statistical significances above $4\sigma$ thereby essentially more than doubling the number of known galactic sources.
Following this introduction into the field, a brief summary of Cherenkov astronomy and the detection principle of Imaging Atmospheric Cherenkov telescopes, along with a description of the H.E.S.S. instrument is given in Chapter 2. One important piece of the detector is the central trigger system which has been developed and commissioned in the context of this thesis. Its functionality and performance is summarised in chapter 3. The techniques employed to analyse the data taken in the H.E.S.S. survey of the Galactic Plane are summarised in chapter 4 followed by the results of the survey in chapter 5. A discussion of the results is given in chapter 6, together with a summary and an outlook for future observations.

# Chapter 2

# The imaging Cherenkov technique

The direct detection of VHE $\gamma$-rays on the ground is not possible, since they are completely absorbed by interactions with the atmosphere of the earth. Therefore satellite experiments are required for the direct detection of $\gamma$-rays. However, for energies above some 10 GeV, the flux of $\gamma$-rays is so low, that the detection area of satellites (in the order of square metres) becomes too small to detect a significant number of $\gamma$-rays in reasonable timescales. A different detection technique is needed for the energy range above tens of GeV and here the Imaging Atmospheric Cherenkov technique proves to be the most promising way. This detection technique records the Cherenkov light of secondary particles, generated by interaction of the primary $\gamma$-ray (or cosmic ray) with the atmosphere's particles. The general physical aspects of the interaction processes and their properties are presented in the following section 2.1. Section 2.2 gives a general introduction on the Imaging Atmospheric Cherenkov technique followed by a description of the H.E.S.S. telescope system in section 2.3, as an example of an instrument that makes use of this technique.

## 2.1 Air Showers

As a VHE particle hits the earth's atmosphere it interacts with atmospheric nuclei (typically in a *first interaction* height of about 10-20 km) thereby creating secondary particles. For a primary particle at TeV energies, these secondary particles in turn interact again with atmospheric nuclei to generate a cascade of particles, commonly referred to as an *air shower*. The evolution of air showers is mainly governed by the available energy and the loss processes that lead eventually to a dying out of the shower. The origin and development of air showers is described in section 2.1.1. The energy of the primary particle is partly converted into kinetic energy of the secondary particles, and therefore these move faster than the speed of light in air and emit Cherenkov radiation that can be detected on the ground. The emission of Cherenkov light is described in section 2.1.2.

### 2.1.1 Origin and Development of Air Showers

#### Interactions of Cosmic Particles with the Atmosphere

Strong, electromagnetic, and weak interactions lead to the development of air showers. In these interactions, secondary particles are created that interact again with atmospheric particles to create an *air shower*. The main interaction processes that lead to the development of air showers are bremsstrahlung and pair production in the case of $\gamma$-rays and electrons and additionally hadronic interactions in the case of protons. These interactions are briefly discussed in the following.

- *Bremsstrahlung* is the main particle production mechanism of $\gamma$-rays. A charged particle gets deflected by the coulomb field of a nucleus while travelling through matter. This deflection is an effective acceleration, which leads to the emission of bremsstrahlung in form of photons. The energy loss in this process is proportional to the energy of the particle. The constant of proportionality is combined into the *radiation length*: $X_0|_{\text{brems}}$. After the particle has travelled a distance of $x = X_0|_{\text{brems}}$ in matter, it has on the average emitted a fraction of $1/e$ of its starting energy in form of bremsstrahlung. The radiation length for electrons in air is $X_0|_{\text{brems}} = 37.2$ g/ cm$^2$, which corresponds to 300 metres at sea level. The photons generated by bremsstrahlung from the high-energetic electrons are emitted in a cone in the forward direction. The average opening angle of the cone is $\langle\Theta\rangle = 1/\gamma = \mu c^2/E$, with $\mu$ being the particle mass. The energy loss by Bremsstrahlung is inversely proportional to the squared mass of the particle. Therefore this process has mainly an effect on electrons and positrons.

- *Pair Production* is the main particle production mechanism of photons at high energy. If the energy of the photon is at least twice as high as the rest mass of the electron, the photon can convert into an electron-positron pair. Because of momentum and energy conservation this process is only possible in the field of another particle, that takes the recoil as the third reaction partner. The amplitude for pair production and bremsstrahlung are related by a crossing symmetry, resulting in a pair production radiation length which is a factor 9/7 larger than the bremsstrahlung radiation length. The average opening angle under which the electron-positron pair is emitted follows the same relation as for bremsstrahlung.

- *Hadronic Interaction* mostly destroy the nuclei involved for the energies relevant in an air shower. Numerous subatomic particles (mainly pions) as well as nuclear fragments are generated.

#### Electromagnetic Showers

An electromagnetic shower forms whenever a particle that interacts via electromagnetic interaction has a sufficiently large energy and hits matter. A cascade of secondary particles produced by the interaction processes described in the previous paragraph builds up. The number of particles grows exponentially. These particles lose energy by the particle production mechanisms and by ionisation. The increase in the number of particles stops

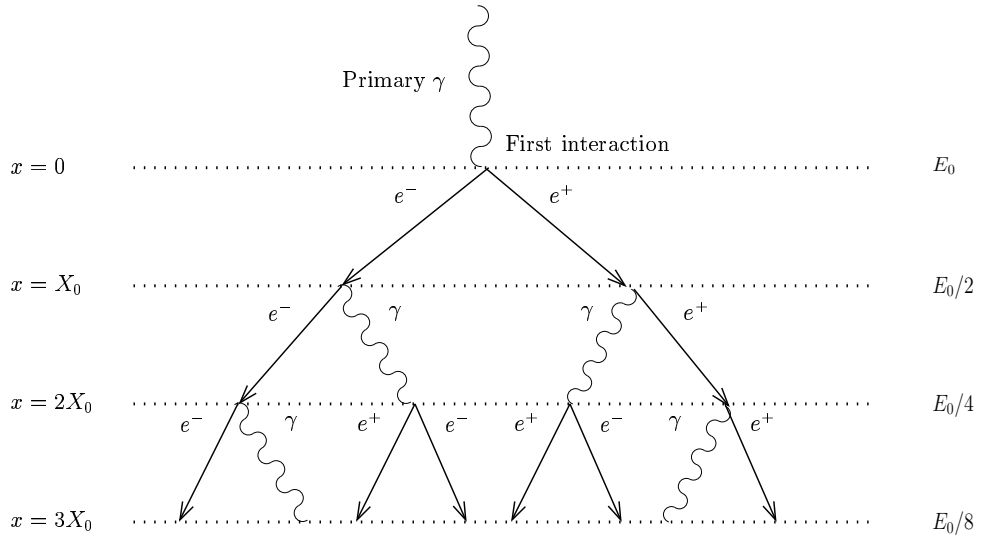


**Figure 2.1:** Illustration of the shower model according to Bethe and Heitler. Bremsstrahlung and pair production are considered, the radiation lengths for both processes are set equal.

if the average energy falls below the "critical energy" $E_c$, where the loss of energy per unit length by bremsstrahlung falls below the loss of energy per unit length by ionisation. In this case no new particles are created but the particles lose energy mainly by ionisation and the shower dies out.
A simple shower model was first introduced by Bethe & Heitler (1954) and relies on very basic assumptions. The main properties of an air shower can however be understood in this model. Only bremsstrahlung and pair production are considered. Energy loss by ionisation is neglected which is a valid approximation for high energetic particles. Both the radiation length for bremsstrahlung and pair production are set to $X_0$, neglecting the factor 9/7 that relates them.
In this model, a primary $\gamma$-ray enters the atmosphere and generates within one radiation length an electron-positron pair via pair production. Hereby its energy $E_0$ is assumed to be equally divided between the two particles. By bremsstrahlung both the electron and positron generate in turn after exactly one radiation length a photon containing half of their energy (see Figure 2.1).
After $m$ radiation lengths $X_0$ the cascade consists of:

$$N(m) = 2^m \text{ Particles having energy } E(m) = E_0 \cdot 2^{-m} \tag{2.1}$$

The depth $m_{\max}$ of the maximum of the shower in the atmosphere in units of the radiation length is given by:

$$E(m_{\max}) = E_0 \cdot 2^{-m_{\max}} \stackrel{!}{=} E_c \quad \rightarrow \quad m_{\max} = \frac{\ln\left(E_0/E_c\right)}{\ln 2} \tag{2.2}$$

at this depth $m_{\max}$, the shower consists of $N_{\max}$ particles

$$N_{\max} = e^{m_{\max} \cdot \ln 2} = \frac{E_0}{E_c} \tag{2.3}$$

This simple shower model illustrates several important properties of an air shower:

- The number of particles in the shower grows exponentially until reaching the shower maximum. The maximum number of shower particles $N_{\max}$ is proportional to the energy $E_0$ of the primary $\gamma$-ray.
- The atmospheric depth of the shower maximum $m_{\max}$ is proportional to the logarithm of the energy $E_0$ of the primary $\gamma$-ray.

To give some numbers, in air the critical energy $E_c \sim 81$ MeV, the timescale on which a complete electromagnetic shower evolves is in the order of microseconds, the typical height of the first interaction for a 1 TeV particle is $\sim 25$ km above sea level, whereas the height of the shower maximum is $\sim 8$ km.

### Hadronic Showers

The shower development for hadrons hitting the earth's atmosphere differs from the shower development for photons and electrons. Hadrons interact nearly only via strong interaction with the nuclei of air molecules. These interactions are much more complex, and hadronic as well as electromagnetic subshowers evolve. In the first interaction of the hadron with a particle of the earth's atmosphere, strong interaction is dominating, and, apart from fragments of the target nucleus, mainly mesons like pions and kaons, but also nucleons (neutrons and protons) and hyperons ($\Delta$, $\Lambda$, $\Sigma$, $\Xi$), are created. From these secondary particles that also interact strongly, a hadronic cascade is generated.
An important role in the development of the hadron induced shower play the neutral pions ($\pi^0$) that are generated at a fraction of about one third of all generated pions. The neutral pions decay almost instantly after a mean lifetime of $(8.4 \pm 0.6) \cdot 10^{-17}$ seconds into two photons as depicted in Figure 2.2. The photons generate electromagnetic subshowers by the interaction mechanisms described in the previous paragraph.
The charged pions ($\pi^{\pm}$) have a much longer lifetime and decay after $2.6 \cdot 10^{-8}$ seconds mainly into muons ($\mu^{\pm}$) which in turn decay into electrons and neutrinos. The longer lifetime of the charged pions results in an increasing probability of new interactions with the nuclei of the air molecules during their lifetime. These interactions give rise to hadronic subshowers in the hadronic cascade. The different types of subshowers of a hadronic shower can be seen in Figure 2.2. The $\mu^{\pm}$ generated in the hadronic interaction do not interact strongly and lose their energy mainly by ionisation processes. This makes them the *penetrating* part of the cosmic radiation, since they can reach the ground level.

### Differences Between Electromagnetic and Hadronic Showers

- The interaction length of hadrons is larger than the radiation length for photons ($\approx 85$ g/cm$^2$ compared to $\approx 35$ g/cm$^2$), and therefore the hadrons penetrate deeper into the atmosphere, leading to a larger maximum shower depth $m_{\max}$.
- In the strong hadronic interaction a non-negligible part of the kinetic energy is lost by the generation of new particles like muons ($\mu^{\pm}$), other mesons, and secondary hadrons.

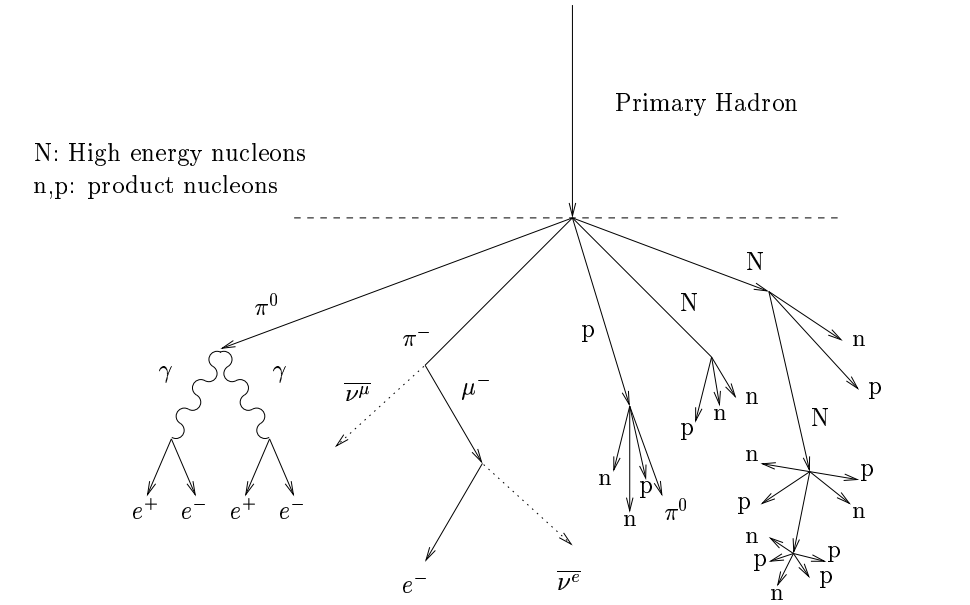


**Figure 2.2:** A primary hadron generates a hadronic cascade. The length of the arrows does not correspond to the lifetime of the particle.

- The lateral development of electromagnetic showers is determined by elastic multiple coulomb scattering of electrons. The mean scattering angle of electrons with energies close to the critical energy $E_c$ is rather small and hence the lateral spread of the electromagnetic shower is small. The secondary particles participating in the strong component of the hadronic shower receive a higher transverse momentum in their production. According to Heisenberg's uncertainty principle an extended target adds to the interaction a typical transverse momentum that corresponds to its size. The size of 1 fm corresponds to 200 MeV, which is the mean transverse momentum of the particles in strong interactions. Therefore the lateral extension of the hadronic shower is much larger. The difference in the lateral extension of electromagnetic and hadronic showers becomes apparent in Figure 2.3 that shows the particle trajectories for simulated photon- and proton-induced air showers.

- complex multiparticle processes are involved in the development of the hadronic shower in contrast to mainly three-particle processes like bremsstrahlung and pair production in the electromagnetic shower. Therefore the hadronic shower is less regular, has larger fluctuations, and contains electromagnetic subshowers that are created by neutral pion decays (see Figure 2.3).

### 2.1.2 The Emission of Cherenkov Light

Charged relativistic particles travelling at a velocity $v$ exceeding the phase velocity of light $c$ in that medium emits Cherenkov light. In the classical picture, the charged particle polarises the surrounding medium and induces constructive interference of electromagnetic

waves. The speed of light in air depends on the pressure and therefore on the height above sea level. At sea level it has a value of 99.97 % of the speed of light in vacuum.
The Cherenkov light is emitted on a cone with a characteristic angle $\Theta_c$ between the Cherenkov light front and the particle's path:

$$\cos(\Theta_c) = \frac{c_n \cdot \Delta t}{v \cdot \Delta t} = \frac{c_n}{v} = \frac{c}{n \cdot v} = \frac{1}{\beta \cdot n} \tag{2.4}$$

Here $n$ is the refraction index of the medium the particle travels through, $v$ the velocity of the particle and $\beta = v/c$ the velocity in units of the speed of light in vacuum. From (2.4) it is apparent that a threshold exists for the emission of Cherenkov light. Since $\cos(\Theta_c)$ must be smaller than 1, Cherenkov light is emitted if the particle velocity $\beta$ fulfils $\beta > \frac{1}{n}$. The Cherenkov angle $\Theta_c$ grows with growing $\beta$ until the maximum angle $\Theta_{c,\max}$ has been reached for ultrarelativistic particles with $\beta \simeq 1$:

$$\Theta_{c,\max} = \arccos\left(\frac{1}{n}\right) \tag{2.5}$$

The minimum energy of a particle moving in a medium to emit Cherenkov radiation is thus given by:

$$E_{\min} = \gamma_{\min} m_o c^2 = \frac{m_0 c^2}{\sqrt{1 - n^{-2}}}. \tag{2.6}$$

Due to the linear dependence on the particle's mass $m_0$, low mass particles such as electrons dominate the Cherenkov emission. The number of photons emitted per unit length $l$ and per unit wavelength $\lambda$ can be calculated using the Frank-Tamm formula:

$$\frac{dN}{dx d\lambda} = 2\pi\alpha Z^2 \frac{1}{\lambda^2}\left(1 - \frac{1}{\beta^2 n^2(\lambda)}\right) \tag{2.7}$$

where $\alpha$ is the fine structure constant and $Z$ the particle's charge. Due to the $1/\lambda^2$-dependence of the number of photons emitted, the peak of the $\frac{dN}{dx d\lambda}$ distribution lies in the UV region. Strong absorption processes of UV radiation in the atmosphere lead to a maximum number of Cherenkov photons emitted in the blue region of the electromagnetic spectrum at about 330 nm.
When crossing the atmosphere, the shower particles cross a medium that continuously changes its refraction index $n$ on the way to the ground. Under the very simplified assumption of an isothermic atmosphere the refraction index was first given by (Halley, 1686):

$$n(h) = 1 + n_0 e^{-h/h_0}, \qquad n_0 = 0.00029, h_0 = 7250\text{m} \tag{2.8}$$

with $h$ being the height above sea level. With decreasing height, the refraction index $n$ of the air increases due to the increasing density and therefore the emission angle $\Theta_c$ of the Cherenkov light increases according to (2.4). For electromagnetic showers, where the secondary particles are emitted mainly in the direction of the primary particle, this leads to a focusing of the Cherenkov light on a cone. Scattering processes lead to a smearing of the light distribution. The light cone of a $\gamma$-ray shower has a homogeneous light distribution in a radius between 80 m and 120 m around the shower axis and decreases

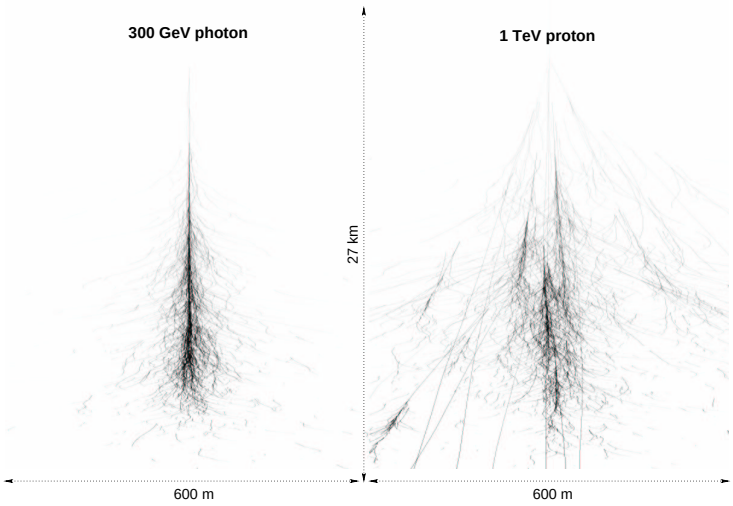


**Figure 2.3:** Longitudinal shower development (particle trajectories) for a simulated 300 GeV photon and 1 TeV proton (Bernlöhr, 2001).

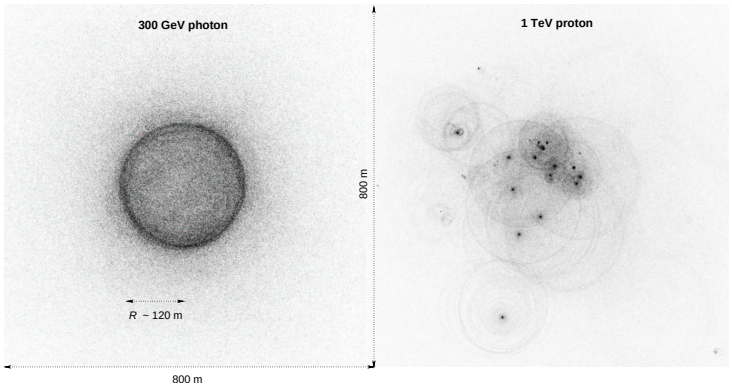


**Figure 2.4:** Simulated lateral Cherenkov light density of the same vertical showers as in Figure 2.3 at 1800 m asl. (Bernlöhr, 2001).

slightly towards the axis. Figure 2.4 shows the Cherenkov light intensity distribution on the ground for simulated photon- and proton-induced air showers.
For hadronic showers the situation is different as secondary particles receive a higher transverse momentum and are therefore more widely spread. Furthermore electromagnetic subshowers are created so that the Cherenkov light emission exhibits larger fluctuations. An additional component to the Cherenkov light on the ground is added by the secondary $\mu^{\pm}$. Since these do not interact strongly and have a rather large livetime of $2.2 \times 10^{-6}$ s, they often reach the ground with sufficient energy to emit Cherenkov radiation in a cone surrounding their path.
The Cherenkov radiation emitted by the secondary particles does not necessarily reach the ground due to absorption processes and scattering. These processes include Mie scattering, Rayleigh scattering and absorption by ozone. As an example, for a primary photon at TeV energy ($10^{12}\,eV$), only about 100 photons per square metre reach the ground at a height of 2 km above sea level.

## 2.2 Imaging Atmospheric Cherenkov Technique

Present instruments in the field of ground-based $\gamma$-ray astronomy are sensitive to photons with energies above $\sim$50–100 GeV. The most sensitive of these instruments are Imaging Atmospheric Cherenkov Telescopes (IACT) or arrays of such telescopes. The pioneering experiment in this field was the Whipple telescope (Weekes et al., 1989), which achieved an energy threshold of around 350 GeV. Significant improvement in sensitivity and energy resolution of the IACT technique was achieved in the last generation of instruments by HEGRA (Daum et al., 1997) through the introduction of stereoscopy, where showers are imaged simultaneously by multiple Cherenkov telescopes. This technique provides a more accurate measurement of shower parameters such as energy and direction and leads to an improved $\gamma$-ray sensitivity. The current generation of instruments aims to lower the energy threshold to below 100 GeV. All new major installations have larger mirror areas than previous generation instruments and are based on the stereoscopic approach (H.E.S.S. (Hinton, 2004), VERITAS (Weekes et al., 2002) and CANGAROO-III (Kubo et al., 2004)) or plan to adopt stereoscopy (MAGIC, phase II (Lorenz et al., 2004)). Figure 1.3 shows a comparison of the energy ranges and sensitivities for previous generation IACTs like Whipple and HEGRA and current generation instruments like H.E.S.S. and VERITAS (denoted "100 GeV IACTs").

### 2.2.1 Detection Principle

IACTs image the Cherenkov light emitted by atmospheric particle showers initiated by $\gamma$-rays or hadrons. The Cherenkov light of an air shower is beamed around the direction of the incident primary particle and illuminates an area of about 250 m diameter on the ground, as discussed in the previous section. Mirrors reflect the Cherenkov light onto a camera containing fast photo-detectors. The detection principle is shown in figure 2.5. The larger the mirror area, the larger the collection area for the detection of the Cherenkov photons and therefore the lower the energy threshold of the system. The Cherenkov

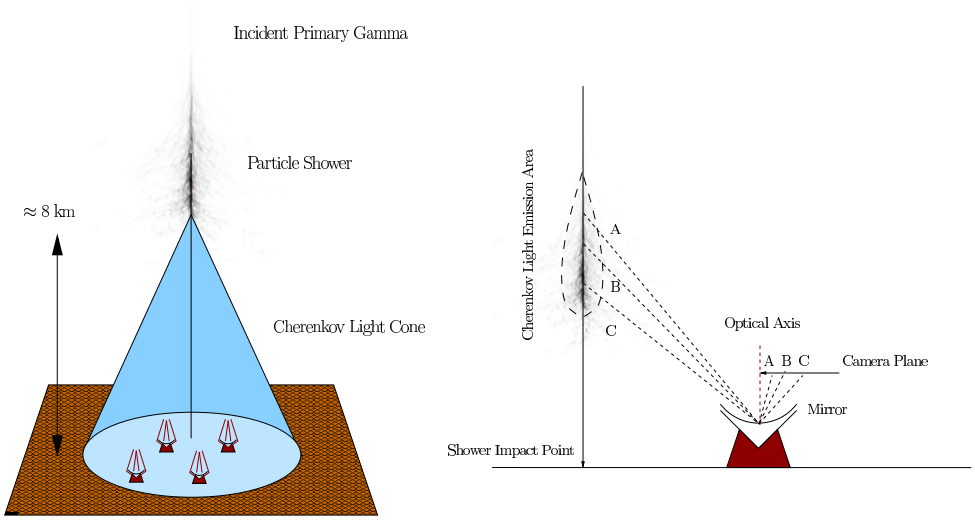


**Figure 2.5: Left:** Detection principle of $\gamma$-rays, using the Imaging Cherenkov technique. The primary $\gamma$-ray hitting the earth's atmosphere generates an air shower. The particles in the air shower emit Cherenkov light on a cone that can be detected by telescopes on the ground. **Right:** Mirrors reflect the Cherenkov light onto a camera in the focal plane. The camera records an image of the light intensity distribution. The mirrors have the properties that light emitted under the same angle towards the optical axis of the telescope get reflected to the same position in the camera.

photons arrive within a very short time interval of a few nanoseconds. For this reason, fast photon detectors and electronics are required to distinguish the Cherenkov light from such air-showers from fluctuations of the night sky background light (NSB). Photomultiplier tubes (PMTs) are currently the most appropriate light sensors for IACT cameras.

### 2.2.2 Triggering Cherenkov Telescopes

The triggering of Cherenkov telescopes makes use of the extremely short duration (a few nanoseconds) of the Cherenkov light signal from air-showers. A typical requirement for triggering the readout of a telescope is that a minimum number of pixels exhibit a signal larger than a given threshold (typically a few photoelectrons), within a short time window, to reduce random triggers from the night sky background. Following a trigger, signals are digitised and read out, resulting in a dead-time ranging from a few $\mu$s to a few ms, depending on the design of the data acquisition system.
The trigger rate (and therefore the dead-time) of IACTs is dominated by background events. For instruments with energy thresholds in the TeV range, hadronic air-showers produce the majority of this background. At the lower energy thresholds reached by telescopes of larger mirror area, single muons passing close to the Cherenkov telescope become a sizable part of the background. In a system of telescopes, the requirement that two telescopes (separated e.g. by $\sim$100 m) both trigger within a short time window leads to a significant reduction in the rate of background events. Since hadronic showers have

**Figure 2.6:** A picture of the H.E.S.S. site.

a more inhomogeneous light pool, the coincidence requirement disfavours such events in comparison to $\gamma$-ray events. Single muons are almost completely rejected by a telescope multiplicity requirement.

Given this reduction in background and the advantages of stereoscopic reconstruction (see for example (Aharonian et al., 1999)), it is necessary to select multiple-telescope events at least for off-line analysis. In a system with non-negligible read-out dead-time it is desirable to select coincident events at the hardware level. A system level coincidence trigger has the additional advantages of greatly reducing the network, disc space, and CPU time requirements of the system.

### 2.2.3 Data taking with IACTs

Observations with Cherenkov telescopes are generally conducted in moonless nights, due to the need for darkness to be able to detect the very faint flashes of Cherenkov light. Each observation night is typically split into runs of 20 to 30 minutes duration during which the Cherenkov telescope system tracks a given astrophysical target or position in the sky. Ideally all other configuration parameters of the telescope system are kept constant during a run. The simplest observation strategy consists of *on/off*-observations of an astronomical object. Runs with the system pointing at the astronomical object (*on*-runs) and runs with the system pointing at an *off*-region (*off*-runs) are performed alternatingly. The off-runs can then be used to derive a background estimation for the on-runs. To reduce the effect of systematic error, the region in the sky observed in the off-runs should be chosen such that the observation is performed at the same elevation of the telescope system as the on-runs. For a detector with a large enough homogeneous field of view, a more appropriate observation strategy is the *wobble*-mode. Here the pointing direction of the system is offset from the astronomical object of interest by a small amount (typical values between $0.5^\circ$ and $1.0^\circ$) alternating in different directions in consecutive runs. The background estimation can then be taken from the same data set (e.g. from a position mirrored with respect to the pointing direction of the system). The advantage of the wobble-mode observation is the elimination of off-source observations for the background estimation and therefore a doubling of the observation time available for on-source observations. Background determination techniques are discussed in section 4.2.

## 2.3 The H.E.S.S. Telescope System

The H.E.S.S. system is a third generation project of IACTs designated for observations of VHE $\gamma$-rays in the energy range between 100 GeV and several tens of TeV. The name of the project is a tribute to Victor Hess who discovered the cosmic radiation in 1912. H.E.S.S. is a stereoscopic system of four telescopes. Multiple telescopes view the same air shower simultaneously. The H.E.S.S. telescope system started operation with one telescope in summer 2002, was completed with the installation of the fourth telescope in December 2003 and has been used for routine data taking since then. At the moment of the publication of this work, H.E.S.S. is the most sensitive and precise instruments of its kind world-wide.
The main advantageous features of H.E.S.S. are:

- The large field of view of the system, covering a space angle of 5°
- The high pixelisation of the H.E.S.S. camera, in comparison to previous instruments which improves the resolution of air shower images
- The low energy threshold of $<$ 100 GeV for zenith observation due to the large mirror area of the telescopes and the usage of a stereoscopic trigger as shown in chapter 3

Additionally H.E.S.S. has the advantage of being located in the southern hemisphere. Therefore the interesting central part of the Galactic Plane with a high density of interesting objects culminates directly at zenith in the Namibian autumn and winter. This provides optimal observation conditions for the central part of the Galaxy in the long winter nights.

### 2.3.1 Site Location

The H.E.S.S. telescope system is situated 1800 m above sea level in the Khomas Highland in Namibia at 23°16'18" southern longitude, 16°30'00" eastern latitude (see Figure 2.7). This site was chosen for its height, its clear cloudless nights and low humidity (Wiedner, 1998). It has been shown that 57% of the moonless darktime was absolutely cloud-free and that in 94% of the nights, the relative humidity was below 90%.

### 2.3.2 Telescope Mechanics

The four H.E.S.S. telescopes are arranged in a square with 120 m side length, to provide multiple stereoscopic views of air showers. The telescope spacing represents a compromise between the effective collection area and large base length required for good stereoscopic viewing of the showers, and the requirement that two or more telescopes are hit by light generated by a single air shower. Showers emit their Cherenkov light mainly at a height between 10 km and 6 km and at a corresponding distance from the telescopes; hence even the 120 m spacing results in rather small angles between different views. On the other hand, given the 250 m diameter of the Cherenkov light pool on the ground (see


**Figure 2.7:** Location of the H.E.S.S. site in Namibia in southern Africa.

**Figure 2.8:** One H.E.S.S. telescope

Figure 2.4), a larger spacing would make it increasingly unlikely that multiple telescopes are illuminated simultaneously. Each telescope has a dish of 13 m diameter, mounted in a rotating frame on a circular rail for movement in the azimuth direction. The telescope is driven by friction drives acting on the 15.0 m diameter drive rails. For both axes the telescope can reach an angular velocity of 100°/min. Shaft encoders measure the actual position of the telescope with shaft encoders in step sizes of 10″. It has been shown (Bolz, 2004), that the accuracy of the drive system for tracking of astronomical objects is better than 3″. However, systematic uncertainties such as the deformation of the dish and the camera arms deteriorate the pointing accuracy, and hence the precision to which $\gamma$-ray sources can be located, to $\sim$ 20″. A photograph of a H.E.S.S. telescope is shown in Figure 2.8.

### 2.3.3 Mirror System

The H.E.S.S. reflector consists of 380 round mirror facets of 60 cm diameter resulting in an area of 107 m$^2$ per telescope as shown in Figure 2.9 (left). The average reflectivity of the mirrors is $\sim$ 80% (for wavelength above 330 nm). The mirror elements are made of aluminised glass with a quartz coating and are arranged in a Davies-Cotton (Davis & Cotton, 1957) design (on a sphere with the radius of the focal length $f$), which provides

**Figure 2.9: Left:** Close-up view on the mirrors of a H.E.S.S. telescope. **Middle:** The camera of one H.E.S.S. telescope with open lid. **Right:** Close-up view on the photomultipliers and Winston cones of the first H.E.S.S. camera.

good imaging also for off-axis rays. The mirror system has a focal length of 15 m and a focal length to diameter ratio of 1.2. Each mirror facet is mounted on a motor-controlled support unit, which can be used to align the individual mirrors. The alignment is performed by tracking a bright star with the telescope system and recording its image in the focal plane with a CCD camera mounted in the centre of the dish. Each mirror spot can be identified separately and can then be driven to its nominal position in the centre of the field of view. The optical point spread function (PSF) of the resulting image by all mirrors in the focal plane is well contained within the camera pixel size of 2.8 mrad and with a value of 0.25 mrad on-axis well within its specifications. The optical PSF depends on the offset in the camera due to spherical aberrations of the reflector. Furthermore it depends on the elevation of the telescope due to deformations of the dish structure but is for all practical observation pointing positions within the pixel size.

### 2.3.4 The H.E.S.S. Camera

The cameras of the H.E.S.S. telescopes serve to capture and record the Cherenkov images of air showers. The camera body of 1.4 m diameter houses the complete trigger and readout electronics. Typical observations of the system record images at a rate of 250 Hz while keeping the dead time below 10%. The design criteria of the camera include:

- a pixel size (0.16°) small enough to resolve image details.
- a large field of view (5° opening angle) to allow observation of extended sources

Each camera consists of 960 pixels and has a triggering scheme that allows the identification of the compact Cherenkov images which arrive within a timescale of nanoseconds. The complete electronics for image digitisation, readout and triggering is integrated into the camera. The pixels of the H.E.S.S. camera are photomultipliers that record the intensity of the incident light. Winston cones (hexagonally shaped light guides) are used to close the gaps between the circular pixels. Individual photons are recorded using the PMTs with a quantum efficiency of $\sim$ 25%. The signal pulse from the PMT is fed into

three different channels, one into the trigger channel of the camera and two into the acquisition system with different gains. By using a high gain and a low gain channel the linear response of the PMT is increased to a dynamic range of up to 2000 photoelectrons (pe). A picture of a H.E.S.S. camera is shown in Figure 2.9 (middle and left).

### 2.3.5 The System Trigger of H.E.S.S.

The trigger of H.E.S.S. is a two-level system. At the first level, telescopes independently form *local triggers* (see section 3.1.2), at the second level a multi-telescope coincidence decision is taken by the central trigger system (CTS). The CTS reduces random triggers due to night sky background as well as single telescope triggers by muons already at the hardware level. This in turn gives the opportunity to reduce the camera trigger thresholds and thus lower the energy threshold of the instrument. In addition to the formation of the system level trigger, the CTS is responsible for dead-time measurement and event synchronisation.
The H.E.S.S. CTS consists of hardware in a central station located in the control building of the array and of interface modules located in each camera. The central station is designed to serve up to 8 telescopes arranged in arbitrary sub-arrays, to accommodate the expansion of the H.E.S.S. telescope system beyond phase I. The communication between the central station and the interface modules is done via an optical fibre system built from standard components with one duplex pair per telescope. The trigger system of H.E.S.S. is described in detail in chapter 3.

Additional components of the H.E.S.S. telescope system are described in (Hinton, 2004).

### 2.3.6 Monte-Carlo Simulations

The H.E.S.S. Monte-Carlo calculations used in this work are split into two parts: CORSIKA (COsmic Ray SImulations for KAscade) (Heck et al., 1998) is a detailed Monte-Carlo program to study the evolution of air showers in the atmosphere initiated by photons, protons, nuclei, or other particles. CORSIKA was originally developed to perform simulations for the KASCADE experiment at Karlsruhe and has been refined over the past decade. CORSICA takes into account environmental parameters, such as atmospheric absorption and geomagnetic field strength and can be used with various particle interaction models. The electromagnetic part of the interactions is based on QED calculations. Major uncertainties are introduced by the simulation of hadronic interactions, since the processes in air showers are dominated by low momentum transfers. These currently can not be described by pertubative QCD. CORSICA therefore uses phenomenological models depending on the energy of the interactions (like VENUS (Werner, 1993) or GHEISA (Fesefeldt, 1985)).
*Sim_hessarray* (Bernlöhr, 2005) simulates the response of an array of H.E.S.S. telescopes to Cherenkov light of air showers with a very high level of detail. The simulation takes into account the reflector layout, the shadow of the camera support structure, mirror reflectivity and optical point spread function as well as the quantum efficiency of the PMTs and the pulse shapes of the PMT signals.

# Chapter 3

# The Trigger System of H.E.S.S.

The trigger system of the H.E.S.S. system is an important part of the instrument and enables to reduce the H.E.S.S. energy threshold and increase the sensitivity. In the following its main properties are discussed.

## 3.1 Components of the H.E.S.S. trigger system

### 3.1.1 Basic data flow

Information on all telescope triggers arrives at the central station. If a valid coincidence occurs, the central station distributes this information to all telescopes and the cameras of those telescopes which participated in this system event are read out. To enable the measurement of the system dead-time, cameras provide their current readout status together with the trigger signal (i.e. whether the camera is *busy* acquiring a previous event or *active* and able to read out this event). The camera trigger and readout status information is stored for each telescope on an event by event basis in a FiFo. From these data the dead-time of the system can be derived. The data flow between the cameras and the central trigger system is shown schematically in Figure 3.1.
To provide a synchronisation mechanism, the CTS assigns for each event a unique, system-wide event number, which is distributed via the trigger hardware to all telescopes. The event number is read by the camera together with the pixel data of each telescope and is used in the process of building a system event from the individual telescope data. An absolute time-stamp for the system event is provided by a GPS clock in the central station.

### 3.1.2 The H.E.S.S. Camera trigger

The trigger of the H.E.S.S. cameras (Vincent et al., 2003) is derived from a multiplicity trigger within overlapping *sectors*, each containing 64 pixels. A camera trigger occurs if the signals in $M$ pixels within a sector (*sector threshold*) exceed a threshold of $N$ photoelectrons (*pixel threshold*). The time-window for the multiplicity trigger is determined from the requirement of a minimum integrated charge above a programmable threshold. For a typical PMT pulse shape the effective trigger window is 1.3 ns (with a jitter of 0.14 ns). This rather narrow gate is possible due to the sorting of PMTs by high voltage

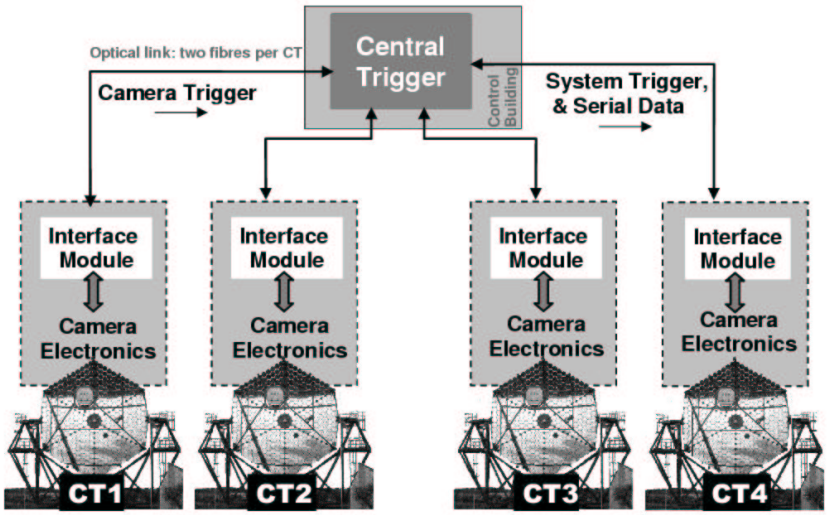


**Figure 3.1:** Schematic of the data flow in the H.E.S.S. central trigger system.

within the camera. This sorting minimises the time dispersion introduced by different PMT transit times. The narrow gate guarantees maximum NSB suppression.
The trigger sectors overlap to ensure a homogeneous trigger efficiency across the field-of-view of the camera. The sector and pixel thresholds are programmable and are in the range of a few photoelectrons for a minimum multiplicity of typically 2 to 4 pixels. The PMT signals are sampled using 1 GHz Analogue Ring Samplers (ARS) (Feinstein et al., 2003) with a ring buffer depth of 128 cells. Following a camera trigger, the ring buffer is stopped and the content of the ring buffer, within a programmable time window (normally 16 ns) around the signal, is digitised, summed and written to an FPGA buffer. This process takes $\approx 273$ $\mu$s. During the first 10 $\mu$s, it is possible to interrupt the digitisation with an external reset signal. In this case, the readout of the analogue memories is stopped and the sampling restarted. After digitisation, the transfer of all buffered data into a global FiFo memory requires another 141 $\mu$s. The total dead-time, including interrupt handling and data acquisition preprocessing is 446 $\mu$s for an event that is read out, or 5.5 $\mu$s for an event that is discarded.
After read out, the camera is ready for the next event. Further data processing within the camera is done asynchronously, including the transmission of data via optical fibre to the PC processor farm located in the control building.

### 3.1.3 Camera Interface

An interface module (illustrated schematically in Figure 3.2) is contained within the body of each camera and is responsible for encoding and transmission of camera triggers and decoding and relaying pulses from the central station. TTL trigger pulses are received from the camera together with a TTL level indicating the current readout status. This

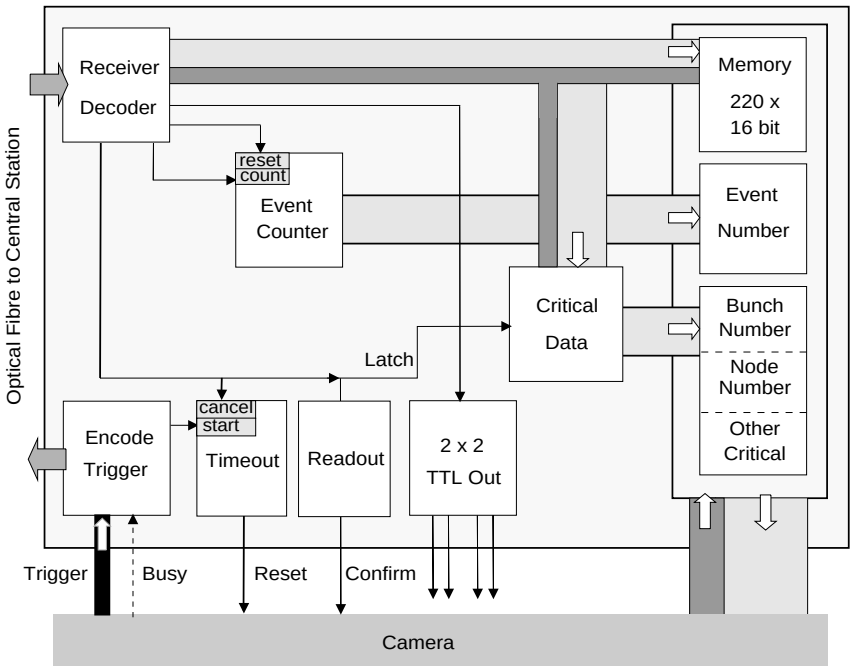


**Figure 3.2:** Schematic illustration of the camera interface module of the H.E.S.S. system trigger. The trigger path is shown in black, data flow is shown in pale grey and addressing in darker grey. Pulses are shown as solid lines.

information is transformed into a width-encoded pulse which is sent via optical fibre to the central station.
Information from the central station is received via a second fibre. Two transmission types are used: a system trigger pulse and a serial data word used to control the interface module and pass data to the camera. The system trigger is also pulse width encoded: the telescopes that have sent active triggers receive *readout* pulses, and all other telescopes receive a *count* pulse. In either case a local event counter is incremented in the interface module and is, therefore, synchronised to the system event counter. In the case of a *readout* pulse, the event counter is latched into an output register on the interface module, where it is read by the camera electronics and written into the data stream.
If a telescope sends an active trigger but no system coincidence occurs, the interface module sends a reset signal to the camera after an adjustable delay, dictated by the round-trip time of pulses between the telescopes and the control building (4.2 $\mu$s) plus the time required to make a coincidence decision (330 ns). If a reset signal is sent, the camera discards the event and is immediately ready for a new trigger and readout.
The serial transmission mechanism is used to periodically reset the event counter and update synchronously a *bunch number* and a *node number* in the interface modules of all telescopes. Both numbers are latched into the memory of the interface module by the arrival of a readout pulse. The node number identifies to which node of the computer farm data should be sent for processing. The combination of the event counter and bunch number provides a unique system wide event identifier which is used for event-building at the farm computer specified as the receiving node.

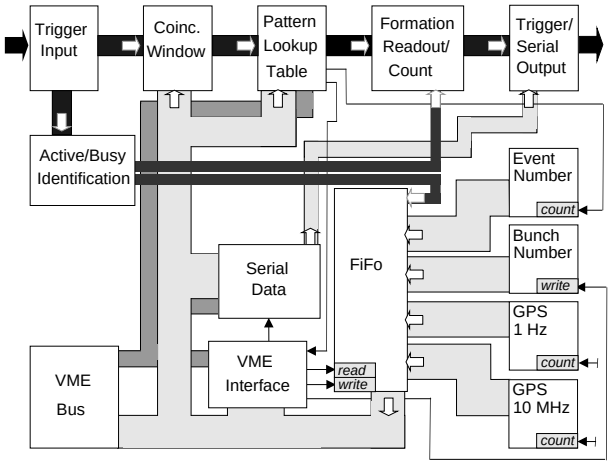


**Figure 3.3:** The flow of information in the H.E.S.S. central coincidence module. The two trigger paths are shown in black. Data flow is shown in pale grey and addressing in darker grey. Pulses are shown as solid lines.

In case a count pulse is lost, the bunch number and the reset of the event counter ensure that the synchronisation of events is recovered after a few seconds.

### 3.1.4 Central Station

The central station hardware consists of the following custom-built VME modules:

- Optical/TTL converter module
- Programmable delay module
- Coincidence trigger module
- Telescope trigger scaler

together with a GPS clock for absolute timing.
Incoming pulses from the optical fibre are converted in the optical converter to TTL pulses. The programmable delay (up to 1 $\mu$s in steps of 1 ns) compensates for the (fixed) delays due to different optical fibre lengths and the (varying) differences in the arrival times of the Cherenkov light front at the individual telescopes. Calculation of the variable component is based on the current pointing direction of the telescope system.
After this delay compensation, telescope triggers enter the coincidence module where they are duplicated and follow two paths (see Figure 3.3). The coincidence path checks if the system trigger condition is fulfilled within the coincidence window, without regard to the busy status of the telescope. The coincidence window is generated by adjusting the width of the incoming pulses to a programmable duration and requiring a minimum overlap of 10 ns. The trigger condition is checked using a programmable lookup table in which all allowed coincidence patterns are stored. This system has the advantage that independent sub-arrays of telescopes can be served simultaneously. The second path

identifies the active or busy status of the telescopes and writes this information (together with the event and bunch numbers and a GPS time-stamp) into a FiFo for every system coincidence. Once this information has been written to the FiFo, the trigger module is ready to accept new triggers, about 330 ns after the coincidence occurred. The FiFo has a depth of 16000 events and is read out asynchronously. The readout time per event is 4.5 $\mu$s, allowing for a maximum sustained rate of 200 kHz. When a system trigger occurs, *readout* and *count* pulses are sent via the optical converter module to the interface modules in each camera.
Event time-stamps are provided by a commercial *GPS167 Meinberg* GPS receiver. This clock provides 1 Hz and 10 MHz TTL signals synchronised to the UTC second. These signals are used as inputs for the corresponding counters in the coincidence module to provided relative timing. An absolute reference time is obtained by serial readout of a complete date/time string from the clock via RS232. The precision of the system has been verified by simultaneous operation of two such clocks and using the optical pulsed emission of the Crab Pulsar as an absolute reference (Franzen et al., 2003). The long term accuracy of the system is $< 2\mu$s.
Only coincident events are recorded by the coincidence module. Individual telescope trigger rates (both *active* and *busy*) are monitored separately using a custom-built VME scaler.

## 3.2 System Trigger Characterisation

Since December 2003, the H.E.S.S. detector has been operating as a four telescope system using the system trigger described here[1]. During March 2004, a number of technical measurements were made with the aim of characterising the complete H.E.S.S. trigger. These measurements used hadronic air-shower events to provide an end-to-end test of the system and are described in detail below.

### 3.2.1 Telescope Delays and Coincidence Window

An efficient and unbiased multi-telescope trigger must provide a coincidence window wide enough that no valid Cherenkov coincidences are lost. On the other hand, the window should be narrow enough to avoid an unacceptable rate of random telescope coincidences. The minimum achievable window is dictated by the intrinsic spread in the arrival times of telescope triggers at the central station. This spread results mainly from the width and curvature of the Cherenkov wave front and the field-of-view of the cameras, and for H.E.S.S. has an r.m.s. of close to 10 ns. The telescope trigger delay compensation – which depends on the pointing direction – is updated frequently enough (in steps of 1 ns) that there is no additional contribution to this spread.
To demonstrate the correct calculation of the compensation delays, the following procedure was applied to all pairs of telescopes. Air-shower data was taken with telescopes tracking an astronomical target. A rather narrow coincidence window was used and a

[1]The system level trigger was installed in July 2003 and operated until December 2003 with 2-3 telescopes, and since then with the complete 4-telescope system.

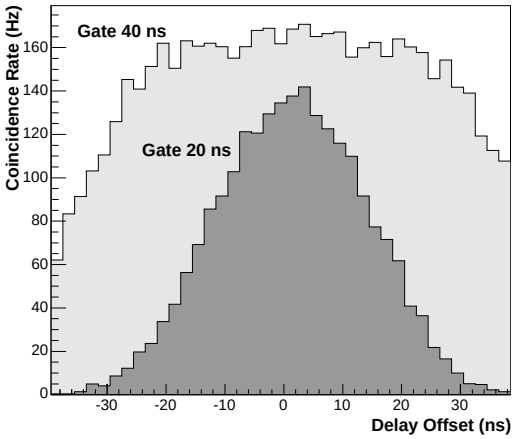


**Figure 3.4:** System rate versus relative delay between a pair of telescopes for coincidence windows of 20 ns and 40 ns.

varying offset was artificially added to the programmed delays. The resulting curve of system rate versus delay offset for one pair of telescopes is shown in Figure 3.4 for two different coincidence windows.
For the 20 ns window, the delay offset which results in a maximum system rate is $1.5 \pm 0.5$ ns. The 40 ns window is significantly wider than the intrinsic spread in arrival times ($\approx$ 10 ns rms) and hence a clear plateau is evident, where the system rate is insensitive to an offset in the telescope delays.
To avoid any bias from the system trigger on the selection of showers, the operating coincidence gate is set to 80 ns. For typical individual telescope rates of 1 kHz, this window introduces an acceptable accidental coincidence rate of 1 Hz for the 4-telescope system.

### 3.2.2 Dead-time Determination

For the determination of spectra and fluxes of astrophysical $\gamma$-ray sources, an accurate measurement of the system dead-time is required. Every Cherenkov event triggering the H.E.S.S. array is recorded by the central trigger system - regardless of the readout status of the cameras. The CTS stores information on which telescopes were able to provide data for a given event, as well as on those that triggered but were busy with the readout of a previous event. This information is used to determine the system dead-time.
Figure 3.5 shows the distribution of time differences between consecutive events in a run involving only a single telescope. The distribution of all triggers is well described by an exponential as expected. The distribution of events where the telescope was read out is also exponential but with a sharp cut-off at the camera readout dead-time of 446 $\mu$s.

### 3.2.3 Trigger Threshold and Trigger Rates

The selection of the trigger threshold has direct implications for the energy threshold of the array. A low energy threshold is clearly desirable for astrophysical reasons, however

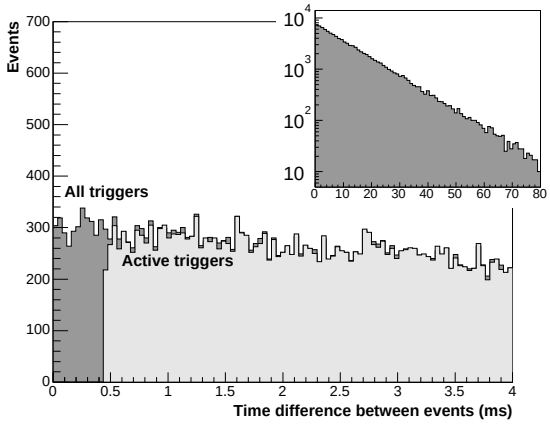


**Figure 3.5:** Distribution of time differences between consecutive events for a single telescope. The dark grey histogram shows all events triggering the system, the light grey histogram shows only events for which the telescope was read out. The inset shows the same distributions but with a logarithmic scale to highlight the exponential behaviour.

the trigger threshold must be set high enough that the trigger rate is both stable and manageable. In the low threshold regime where night sky background triggers dominate, the rate is expected to be both very high and unstable. Measurements of the dependence of the system trigger rate on all available parameters dictating the threshold are therefore crucial in determining the optimal operating parameters.

The adjustable parameters which directly affect the energy threshold and trigger rate of the system are: the camera pixel and sector thresholds (see section 3.1.2), and the telescope multiplicity requirement. The measurements described below involve variation of these parameters. All were made with all four telescopes of the system tracking a relatively dark region of the sky close to zenith.

Figure 3.6 shows how the rates of individual telescopes and the system rate depend on the pixel threshold. Curves are shown for minimum telescope multiplicities of 2 and 3. The pixel threshold is quoted in units of photoelectrons (p.e.), defined as the mean amplitude of a single photoelectron signal at the pixel comparator (21 mV). In all curves, two regimes are clearly present: a smooth power law dependence at higher thresholds and a rapid increase in rate below $\approx 4$ p.e. For low pixel thresholds, the camera triggers are dominated by pixel coincidences due to night sky background fluctuations and the system rate is dominated by accidental telescope coincidences. For higher pixel thresholds, random pixel coincidences in the cameras are rare and Cherenkov events from cosmic ray air-showers dominate.

The small dispersion in single telescope rates (in the air-shower dominated regime) that is evident in Figure 3.6 demonstrates the homogeneity of the array. Inter-telescope differences in mirror reflectivity and pixel efficiency are at a level of less than 10%.

Figure 3.7 shows a comparison of system rate versus pixel threshold for three sector thresholds (pixel multiplicities). For a threshold of 2 pixels, the transition between the NSB and air-shower regimes is rather gradual. For such a condition the system trigger may

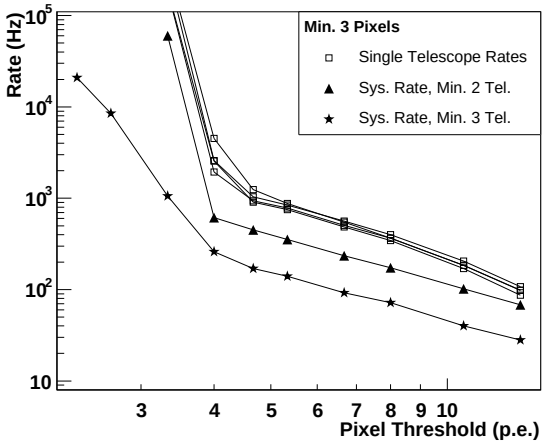


**Figure 3.6:** Single telescope rates and system rate (for a sector threshold of 3 pixels) against pixel threshold. The system rate is shown for telescope multiplicities 2 and 3. Statistical error bars are in all cases smaller than the symbols.

be affected by NSB fluctuations for a wide range of possible pixel thresholds. As expected, at a higher sector threshold of 4 pixels, a lower operating pixel threshold is attainable. For sector multiplicities of 3 and 4, similar minimum image sizes and system trigger rates are attainable (within the air-shower dominated regime). As a sector threshold of 3 preferentially selects the more compact images typical of gamma-ray initiated showers, this threshold is preferred.

Figure 3.7 also shows the expected rate of accidental coincidences for a sector threshold of 3 pixels, calculated using the measured single telescope rates and the system coincidence window of 80 ns. The measured system trigger rate at a 3.4 photoelectron threshold is in good agreement with the predicted rate of accidentals, indicating that the system trigger behaves as expected, even at this extremely high rate (50 kHz). The open circles show the system trigger rate predicted by Monte-Carlo simulations using CORSIKA (Heck et al., 1998) and *Sim_hessarray* (Bernlöhr, 2005) (see section 2.3.6), combined with the expected accidental rate. The comparison of the predicted and measured rates provides an end-to-end test of the simulations and the good agreement is encouraging.

The measurements described above were all made in a relatively dark region of the sky, away from the galactic plane. In such regions the median pixel NSB determined from pixel currents (Aharonian et al., 2004c) is close to $9.2 \times 10^7$ photoelectrons $s^{-1}$ per pixel, compared with the expected value of $8.5 \pm 1.3 \times 10^7$ photoelectrons $s^{-1}$ per pixel (Preuss et al., 2002). However, as $\gamma$-ray observations of all parts of the sky are planned with H.E.S.S. the system must operate stably in much brighter regions of the sky. In a field-of-view with many bright stars or with increased diffuse emission, NSB triggers may occur at higher pixel threshold than in a dark region. To study this effect, the rate versus threshold measurements described above were repeated in the particularly bright region around $\eta$ Carinae. In this region the transition to NSB dominance occurs close to 4.7 p.e. for a sector threshold of 3 pixels.

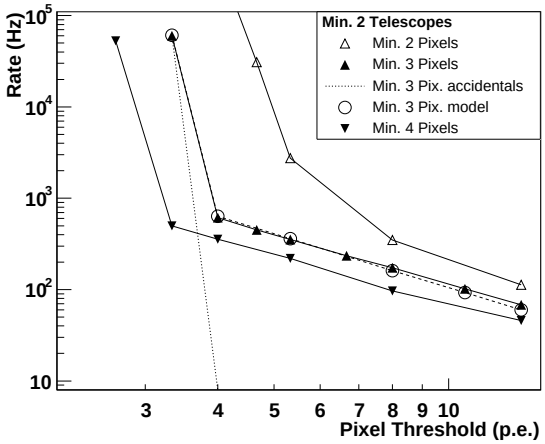


**Figure 3.7:** System trigger rate against pixel threshold for three sector thresholds. For a sector threshold of 3 pixels the predicted rate from accidental telescope coincidences is shown along with the simulated rate for this configuration (open circles). The statistical error bars are smaller than the symbols for all measured curves.

To avoid significant NSB trigger rates in bright regions of the sky and as a compromise between higher $\gamma$-ray collection efficiency and reduced energy threshold, a configuration of sector threshold 3, pixel threshold 5.3, and telescope multiplicity 2 was chosen for H.E.S.S. observations.

### 3.2.4 Zenith Angle Dependence

The measurements described in the previous section were performed close to zenith. Standard H.E.S.S. observations take place in a zenith angle range of 0-35°. In certain circumstances this range is extended as far as 60°. At large zenith angles, air-showers are observed through a much greater atmospheric column depth. Cherenkov photons from such showers suffer more from scattering and absorption and have a larger (and dimmer) footprint on the ground. As a consequence of the reduced density of photons in the light pool, the effective energy threshold of the system is increased. On the other hand, the larger light pool diameter results in an improved effective collection area.

Figure 3.8 shows the rate of the system (and the mean single telescope rate) as a function of the cosine of the zenith angle. A smooth, monotonic decrease is evident for the single telescope and multiplicity-2 rates as expected from the increasing absorption of showers and the steep energy spectrum of the hadronic background. The solid and dashed lines in Figure 3.8 shows the predicted behaviour assuming two different atmospheric transmission tables calculated using MODTRAN (Bernlöhr, 2000). The solid line is based on a rather conservative assumption of aerosol content (maritime haze, boundary layer starting at sea level). The dotted line corresponds to a clearer atmosphere (desert haze, boundary layer starting at 1800 m). The difference between the two predictions indicates the current uncertainty in our understanding of the atmosphere at the H.E.S.S. site which are in the

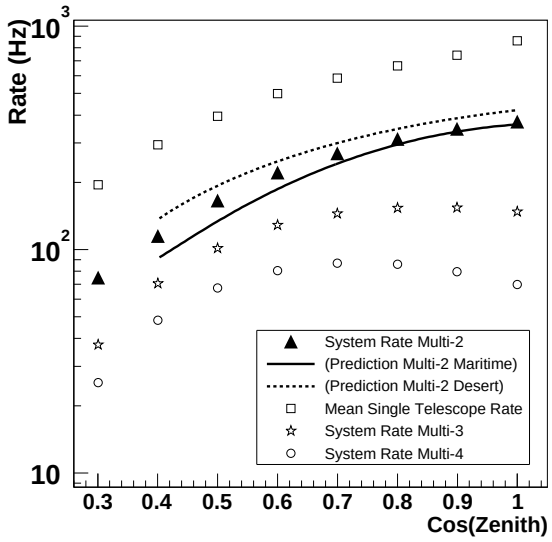


**Figure 3.8:** Mean single telescope and system rate against cosine zenith for telescope multiplicities of 2, 3 and 4. The solid and dashed lines show the rate predicted for multiplicity-2 using two different atmospheric models. These data were taken with telescopes pointing to the north. All statistical error bars are smaller than the plotted symbols.

order of 20%.
The increased diameter of the Cherenkov light pool at large zenith angles leads to an increased average telescope multiplicity. This effect is apparent from a comparison of the telescope multiplicity-2 rate with the curves for larger telescope multiplicity in Figure 3.8, indeed the multiplicity-4 rate reaches its maximum at 40° zenith angle.

### 3.2.5 Convergent Telescope Pointing

The simplest pointing strategy for a telescope array is to track a target with all telescope axes parallel. All measurements described above employed this observation mode. However, given a typical emission height of Cherenkov photons ∼10 km above the observation level, a more effective strategy may be to *cant* the telescopes towards each other slightly (Lampeitl et al., 1999). Given the altitude and array spacing of H.E.S.S. the convergent angle required to maximise the overlap of the telescope field-of-views at the height of maximum shower development is around 0.7°. Figure 3.9 shows the measured dependence of system trigger rate on the canting angle between telescopes. The maximum trigger rate occurs at a canting angle of 0.65°, corresponding to convergence at a point 10.5 km above the H.E.S.S. site. The solid curve shows a fit of a simple geometrical model of overlapping telescope field-of-views.
Maximising the overlap of telescope field-of-views results in $\gamma$-ray images that typically lie closer to the centre of the cameras and increases the average number of usable images in the analysis. This in turn leads to improved angular resolution and hence to better sensitivity. Convergence to a fixed atmospheric depth of 270 $\mathrm{g\,cm^{-2}}$ (the depth of max-

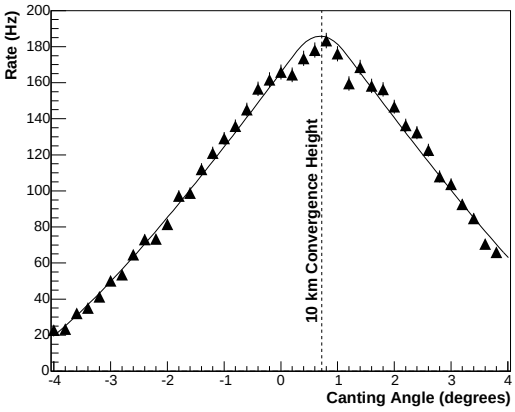


**Figure 3.9:** System rate as a function of the relative alignment of the telescope axes for two telescopes separated by 120 m. The inclination of the telescopes takes place in the plane connecting the two telescopes. Positive values refer to convergent telescope pointing. The solid line is a fit to the data of a simple geometrical model.

imum Cherenkov photon emission for an average 100 GeV $\gamma$-ray shower) is planned for future H.E.S.S. observations.

## 3.3 Implications for System Performance

The operation of a multiplicity-2 telescope trigger for the H.E.S.S. system has many implications. A major consequence is the removal of single muon events at the trigger level. Single muon images have a characteristically narrow distribution of surface brightness. As a consequence they are limited to a small region in the parameter (image *length*)/(image *size*) (following the definition of image parameters of Hillas (1985)). Figure 3.10 shows the distribution of $length/size$ with and without a telescope multiplicity requirement for fixed camera trigger conditions. For telescope multiplicity-1 there is a large peak at around $3 \times 10^{-5}$ radians/photoelectron. This peak is produced by images of single muons as can be seen by comparison with the curve for simulated muons shown in Figure 3.10. The tail to the right of the peak is likely produced by more complex shower images that are still dominated by a single muon. From the telescope multiplicity-2 curve in Figure 3.10 it is clear that a multi-telescope trigger is extremely effective at removing such background events; the peak attributed to single muon images is almost completely absent.
The reduction in background evident in Figure 3.10 leads to a lower system trigger rate at a given threshold and hence to reduced readout dead-time. Figure 3.11 compares the incurred system dead-time versus pixel threshold with and without a telescope multiplicity requirement.
The dashed line shows the dead-time, calculated defining a *live* system trigger as one where at least 2 telescopes were read out. For the solid curve a more conservative requirement, that all triggered telescopes were read out, was applied. To achieve an acceptable dead-time fraction of 10–15% without a system level trigger, the pixel threshold would have to

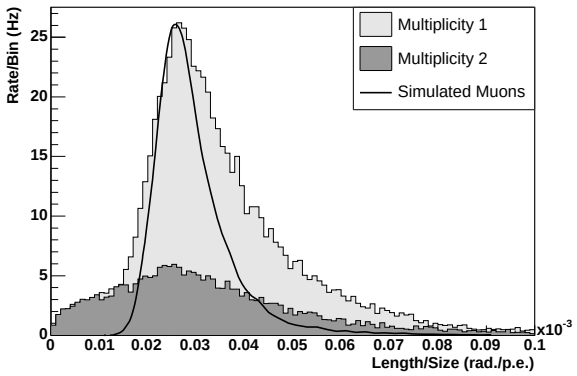


**Figure 3.10:** Distribution of *length*/*size* of images for telescope multiplicity 1 and 2. The distribution of simulated single muons is shown by the solid curve.

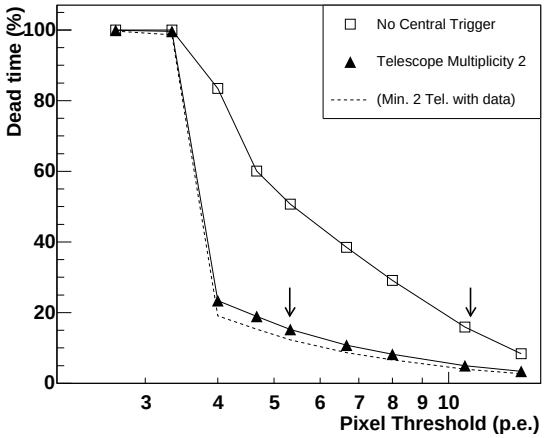


**Figure 3.11:** Derived system dead-time as a function of pixel trigger threshold (for a fixed sector threshold of 3 pixels), with and without a system level trigger. The dashed and solid curves are calculated using different definitions of the system dead-time (see text). The left arrow shows the current operating pixel threshold of H.E.S.S. the right arrow shows the threshold corresponding to the same system dead-time with no telescope multiplicity requirement.

| Configuration | Camera Trigger Condition | System Rate (Hz) | Crab $\gamma$-ray Rate ($\mathrm{min}^{-1}$) Predicted Pre-cuts | Predicted Post-cuts | Measured Post-cuts |
|---|---|---|---|---|---|
| Single Telescope | 6.7 pe, 4 pix | 170 | 9.1±1.6 | 3.0±0.5 | 3.8±0.1 |
| 2-Tel. Soft. | 6.7 pe, 4 pix | 50 (280) | 5.6±1.0 | 3.6±0.7 | |
| 2-Tel. Hard. | 5.3 pe, 3 pix | 90 | 13.5±2.4 | 6.7±1.2 | |
| 3-Tel. Hard. | 5.3 pe, 3 pix | 180 | 20.2±3.7 | 11.8±2.1 | 10.4±0.3 |
| 4-Tel. Hard. | 5.3 pe, 3 pix | 270 | 25.9±4.7 | 15.6±2.8 | |

**Table 3.1:** Comparisons of the performance of different H.E.S.S. configurations. The typical system trigger rate is given together with the predicted (and measured) $\gamma$-ray rate from the Crab Nebula (at 47° zenith angle). The predicted rates are calculated using the spectrum published by the HEGRA collaboration (Aharonian et al., 2000), the errors shown are statistical only. *Soft.* and *Hard.* refer to software and hardware 2-telescope multiplicity requirements. For the *2-Tel. Soft.* configuration the trigger rate including single telescope events is shown in parentheses.

be increased by a factor ∼2. As the energy threshold of the instrument scales roughly with the pixel threshold, operation of H.E.S.S. with a central trigger significantly increases the sensitive energy range of the array.

During the construction and commissioning phase of H.E.S.S. , $\gamma$-ray observations have been made using several array configurations. The improvements in performance associated with the development of H.E.S.S. from a single telescope system to a full array, are illustrated in table 3.1. The rate of $\gamma$-rays expected from the Crab Nebula is used as a figure of merit in this table. Observations of the Crab Nebula by H.E.S.S. have been used to confirm the performance predicted by air-shower and detector simulations. The improvement in performance between the *2-Tel. Soft.* and *2-Tel. Hard.* configurations is solely a consequence of the introduction of the system level trigger.

Figure 3.12 illustrates the decreasing energy threshold of the array during the commissioning phase. With the complete 4-telescope H.E.S.S. phase-I system a hardware energy threshold of 100 GeV is achieved at zenith. After $\gamma$-ray selection cuts the threshold increases to 125 GeV. In comparison, the post-cuts threshold for data taken with a single H.E.S.S. telescope is 265 GeV. For this configuration a *length/size* cut is imposed to reject single muons off-line, at the expense of an increased analysis threshold.

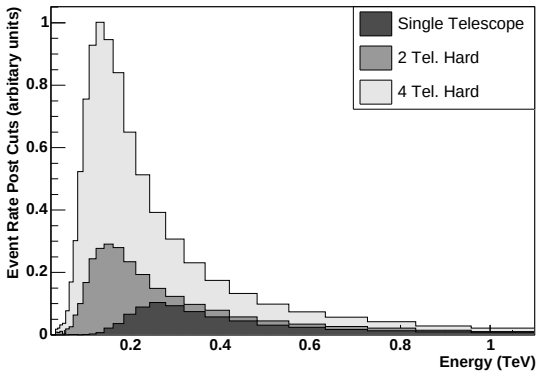


**Figure 3.12:** Post-cuts differential rate expected on the basis of detailed simulations for a Crab-like source at zenith, for different H.E.S.S. configurations. The energy threshold is conventionally defined as the peak in this distribution and is 265 GeV, 145 GeV and 125 GeV for the single telescope, 2-telescope and 4-telescope configurations respectively.

# Chapter 4

# Data Analysis

To analyse $\gamma$-ray data several steps in the analysis have to be performed. The analysis described here is comprised of the reconstruction of type, direction and energy of the primary particle as described in section 4.1, followed by the modelling of the background as described in section 4.2. For sources of $\gamma$-rays the position has to be accurately determined as described in section 4.3, followed by a determination of the energy spectrum of the emission region as described in section 4.4. Some basic performance properties of the H.E.S.S. telescope system are given in section 4.6.

## 4.1 Reconstruction

As previously stated, only secondary products of the primary particle can be recorded with IACTs. The main aim and difficulty for IACTs is therefore to fully reconstruct properties like type, energy and direction of the primary from the light of the Cherenkov air shower. The use of more than one telescope significantly improves the ability to reconstruct these properties as the shower can be recorded under different viewing angles. For $\gamma$-ray initiated showers the light yield at the ground is roughly proportional to the energy of the primary particle. $\gamma$-ray showers are observed against a background of much more numerous hadronic showers. This background can be greatly reduced using the morphology of air-shower images. Unless otherwise stated, the Monte-Carlo simulated $\gamma$-rays used in the following to examplify the performance of the system were simulated with an energy spectrum of a Crab-like photon index of 2.6 at a zenith angle of 20°.

### 4.1.1 Image Cleaning

After calibration of the light intensity distribution in the camera, the image is cleaned of noisy pixels that have intensities unrelated to the Cherenkov image and are likely to be caused by photomultiplier noise or night sky background. The process of image cleaning is typically based on two threshold values $T_{\text{high}}$ (usually around 10 photoelectrons) and $T_{\text{low}}$ (usually around 5 photoelectrons). These threshold values correspond to the number of photoelectrons in a given pixel. The image cleaning method categorises each pixel of the image in the following way:

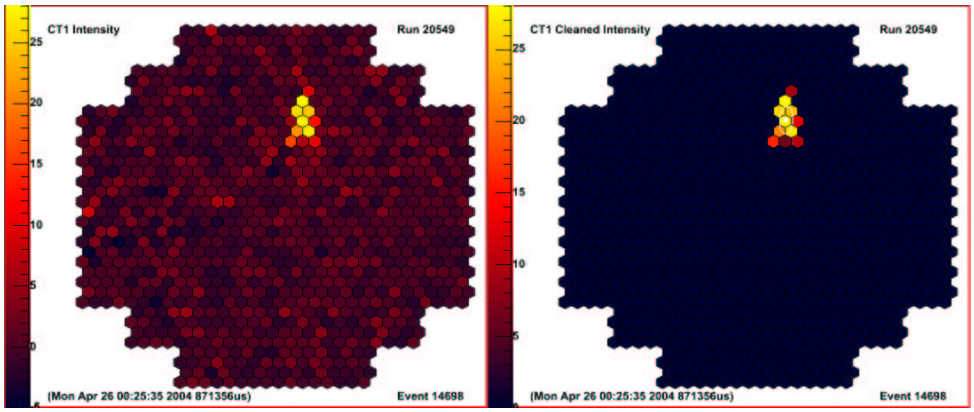


**Figure 4.1: Left:** Intensity distribution of a $\gamma$-ray candidate event in one camera. The colour denotes the pixel intensity in photoelectrons. **Right:** Same event after image cleaning using tailcuts of $T_{\text{high}} = 10$ and $T_{\text{low}} = 5$. Also shown is the resulting (white) Hillas ellipse, parametrised as described in the next paragraph.

- pixels containing more photoelectrons than $T_{\text{high}}$ with a neighbouring pixel above $T_{\text{low}}$ are kept in the image.
- pixels containing more photoelectrons than $T_{\text{low}}$ but less than $T_{\text{high}}$ with a neighbouring pixel above $T_{\text{high}}$ are kept in the image.
- in addition to the two fixed threshold values, a NSB threshold is used to prevent the inclusion of pixels suffering from bright star light. Only pixels passing the two first cuts and have an intensity of more than $3\sigma$ of the pedestal RMS are kept.
- all other pixels are discarded and not considered in the calculation of the Hillas parameters that will be presented in the following paragraph.

Figure 4.1 shows a camera image for a $\gamma$-ray candidate before and after image cleaning. The cleaning process leads to a large reduction in the number of pixels present in the image.

### 4.1.2 Hillas Parameters

A standard method for parametrisation of the light intensity distribution in the cameras is the *Hillas parameterisation* (Hillas, 1985), which are calculated after cleaning the camera image from noise. The Cherenkov light intensity distribution for $\gamma$-ray induced showers in the camera is in a first approximation elliptical. This ellipse can be characterised by parameters which can be written in terms of moments of the light intensity distribution. The parameters correspond to position, orientation, shape and brightness of the image in the camera. Figure 4.2 shows the basic Hillas parameters:

The position of the Hillas ellipse in the camera is given by the centre of gravity ($COG$) of the light intensity distribution. The parameter *length* $L$ specifies the rms length of

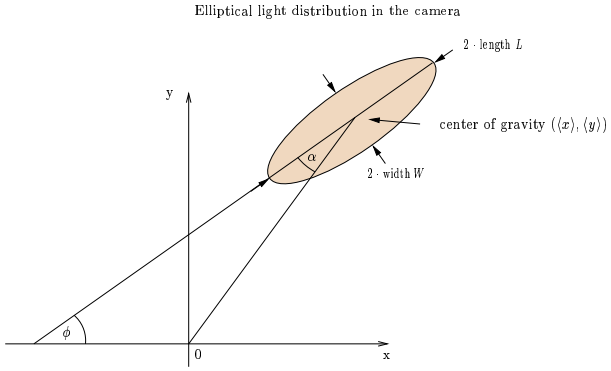


**Figure 4.2:** Hillas parameters characterise the elliptical light intensity distribution in the camera.

the major axis of the ellipse, while the parameter *width* $W$ represents that of the minor axis. Some Hillas parameters contain information about the direction of the shower (e.g., $\alpha$), while others contain information about its size (e.g., size ($Si$), width ($W$), length ($L$)). Therefore some Hillas parameters can be used to characterise shower parameters like energy and direction, while others allow the estimation of the primary particle's type as will be described in the following.

### 4.1.3 Direction Reconstruction

As the stereoscopic technique requires more than one camera of the system to be triggered by the Cherenkov light of the same air shower, the direction reconstruction makes use of this simultaneous viewing of the shower from different angles. For each shower image the origin of the shower is located on the major axis of the ellipse. Therefore by intersecting the major axis of the ellipses from the different cameras, a precise determination of the shower direction can be achieved (see Figure 4.3). Similarly the impact point of the shower on the ground (the *core*) can be determined. Each shower image determines a plane orthogonal to the camera plane. This plane contains also the shower axis and therefore also the shower core. The shower planes intersect the ground in a straight line, on which also the shower core must be located. Therefore one can apply the same mechanism as used for the determination of the shower direction to derive the position of the shower core. Typical values for the angular resolution of stereoscopic telescope systems are in the order of 0.1° and 10 m for the core location.

### 4.1.4 Energy Reconstruction

To estimate the energy, the relation between the particle's energy and the recorded signal in the camera has to be determined from Monte-Carlo simulations. The energy of the observed $\gamma$-rays are determined using the mean of the energies independently estimated for each telescope with a typical event resolution of $\sim$15%. Energies are parametrised from Monte-Carlo simulations using the image amplitude, the reconstructed impact parameter of the event (i.e. the distance of the shower core to the position of the telescope) and the zenith angle of observation for the telescope system. Figure 4.4 (left) shows for two

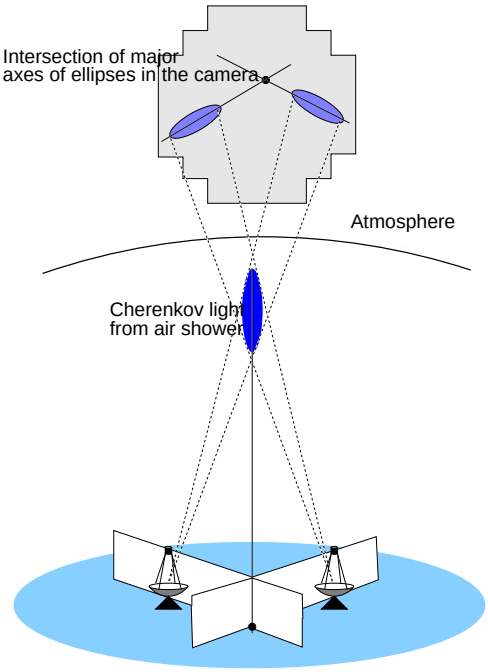


**Figure 4.3:** Schematic description of the shower reconstruction.

different sets of cuts (as will be described in the following) the distribution of the error $\Delta E$ in the reconstructed energy for Monte-Carlo simulated $\gamma$-ray showers, given by

$$\Delta E = \left(E_{\mathrm{reco}} - E_{\mathrm{sim}}\right) / E_{\mathrm{sim}} \tag{4.1}$$

Figure 4.4 (middle) shows for the *standard cuts* as described in section 4.1.5 the distribution of $\Delta E$ as a function of the simulated energy $E_{\mathrm{sim}}$. It can be seen, that the energy reconstruction gets better with increasing energy as expected, since on average more light is collected in each camera leading to smaller statistical fluctuations in the image size. Additionally the intrinsic shower fluctuations also decrease with increasing energy. The energy resolution of the system, defined as the root mean square (rms) of the distribution has a value of 16% at this zenith angle. The energy bias is defined as the mean value of the error distribution as shown in Figure 4.4 (right) as a function of the true energy. For energies close to the threshold there is an unavoidable bias due to the effect of the sharp image amplitude cut preferentially selecting events with energies reconstructed with too large a value since only upward fluctuations are considered. The reconstructed energy is sensitive to various systematic effects, as for example:

- Atmospheric effects. The interaction of particles and the propagation of the Cherenkov light in the atmosphere introduces the largest uncertainty in the determination of the energy. Monte-Carlo simulations of air showers in the atmosphere are used to predict the light yield as a function of energy and shower position relative to the detector, assuming good and stable weather conditions. The uncertainties arising from the atmosphere are in the order of 20% as discussed in the previous chapter and can be seen from figure 3.8.

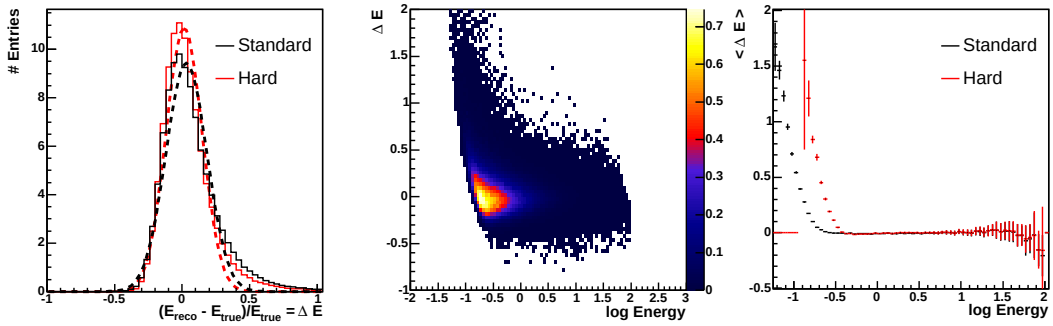


**Figure 4.4: Left:** Distribution of $\Delta E$ (as defined in the text) for all energies for standard (black) and hard cuts, along with Gaussian fits to the distributions. The mean and rms for the standard cuts are ($0.03 \pm 0.02$ and $0.15 \pm 0.01$ respectively) and for hard cuts are ($0.014 \pm 0.017$ and $0.13 \pm 0.01$ respectively), proving that the hard cuts have a slightly better energy resolution as expected. **Middle:** For standard cuts, distribution of $\Delta E$ as a function of the true energy normalised to a percentage. **Right:** Profile plot of the distribution shown in the central panel. This shows the energy bias, given by the mean of the $\Delta E$ distribution. It can be seen from this curve, that the hard cuts have a higher energy threshold due to the increased size cut of 200 pe on the total image amplitude.

- The optical response of the instrument. The response of the system to Cherenkov light is amongst others affected by the reflectivity of the mirrors and the Winston cones, and by shadowing of the telescope masts. This response is monitored by studying Cherenkov light from single muons passing close to the telescope in dedicated Muon-runs in which no coincidence between telescopes is required. The analysis of muons in the determination of the telescope response is described in detail in Bolz (2004).

- The camera response. The single photon-electron gain of PMTs is monitored by a LED system mounted in front of the camera. Differences between the PMTs of a camera (due to differences in quantum efficiencies of the PMTs and reflectivity of the Winston cones) are flatfielded, using a laser mounted on the telescope dish. The calibration scheme is described in detail in Aharonian et al. (2004c).

### 4.1.5 Gamma-Hadron Separation

In a stereoscopic system, the vast majority of recorded events result from hadronic cosmic-rays. To reduce this much more numerous cosmic-ray background, whilst keeping a large fraction of the $\gamma$-ray induced images, cuts on image parameters have to be applied. The H.E.S.S. standard analysis cuts applies cuts on the total image amplitude (size) in each camera to reject poorly reconstructed events at the expense of a higher energy threshold. The effect of truncation of images by the camera edge is reduced by an additional cut on the distance of the centre of gravity of images from the centre of the camera (nominal

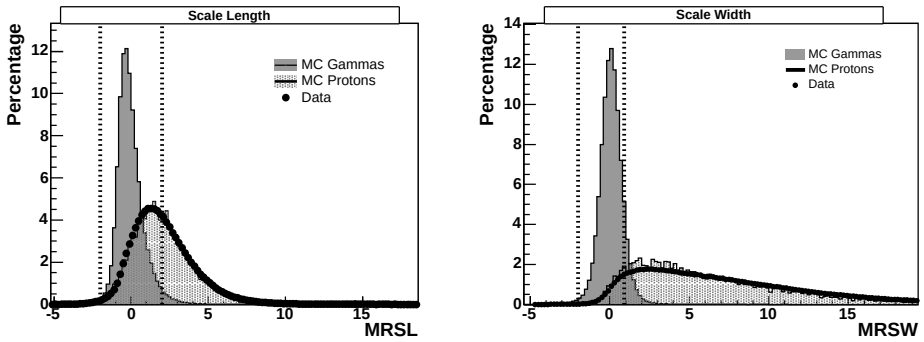


**Figure 4.5:** Distribution of MRSL (left) and MRSW (right) for Monte-Carlo simulated $\gamma$-rays and protons and for off-source data without application of any image cuts.

distance cut, typically at 2°).

The principle cuts separating the $\gamma$-ray signal from the hadronic background are applied on the parameters mean reduced scaled width (MRSW) and length (MRSL). These parameters are defined as the mean of the difference in standard deviations for each telescope of the width (length) observed in the image from that which is expected from $\gamma$-ray simulations based on image intensity, reconstructed impact parameter and zenith angle of the shower. These cuts are commonly referred to as *shape cuts* and result in a selection of $\gamma$-*like* events. The cuts make use of the difference in the shape of the light intensity distribution of $\gamma$-rays and hadrons as described in section 2.1.2. The cuts are optimised to maximise the detection significance for typical sources. Figure 4.5 shows the distributions of MRSW and MRSL for Monte-Carlo simulated $\gamma$-rays, protons and for real data without application of cuts. The reasonable agreement of the simulated protons with the measured background shows that the background is well understood. It should be noted that the optimum selection cuts depend on the assumed $\gamma$-ray energy spectrum. The cuts used in this work have been optimised for source with a power-law spectrum of photon index 2.6. Finally a directional cut on $\theta^2$, the square of the angular difference between the reconstructed shower position and the source position, can be applied and is equivalent to placing the data into a round angular bin centred on the source position. Since the charged component of the cosmic rays arrive isotropically as opposed to the $\gamma$-rays, this cut can be used to further suppress the residual hadronic background.

Two different sets of cuts are employed in this work, *standard* and *hard* cuts. These two sets differ in the size cut and the $\theta^2$ cut used. The standard cuts use a size cut of 80 pe and an optimal $\theta^2$ cut of 0.02°, whereas the hard cuts use a size cut of 200 pe and a $\theta^2$ cut of 0.01°. The hard cuts have the advantage of reducing the background by a factor of 7 and yield optimum sensitivity for weak sources, provided that the source energy spectra are not significantly steeper than that of the Crab Nebula. The standard cuts have the advantage of a lower energy threshold in comparison to the hard cuts which is especially desirable in the determination of energy spectra. The cuts are summarised in Table 4.1.

The difference between the two sets of cuts can be quantified by the cut efficiency for $\gamma$-rays and for protons. The $\gamma$-ray efficiency can be determined from application of the cuts on Monte-Carlo simulated $\gamma$-rays. The proton efficiency has to be derived from

| Configuration | MRSL | | MRSW | | $\theta^2$ | Image Amp. | Distance |
|---|---|---|---|---|---|---|---|
| | Min | Max | Min | Max | Max ($deg.^2$) | Min (p.e.) | Max (deg.) |
| Standard | -2.0 | 2.0 | -2.0 | 0.9 | 0.02 | 80 | 2.0 |
| Hard | -2.0 | 2.0 | -2.0 | 0.9 | 0.01 | 200 | 2.0 |

**Table 4.1:** Optimised $\gamma$-ray selection cuts for point sources. Cuts are applied on MRSW and MRSL, as well as on the distance ($\theta$) from the reconstructed shower position to the source. A minimum of two telescopes passing the cuts on image amplitude and distance from the centre of the field of view, are also required.

| Configuration | $\epsilon_\gamma$ | $\epsilon_{\gamma,\mathrm{reco}}$ | $\epsilon_{\mathrm{CR}}$ | $\epsilon_{\mathrm{CR},>2\mathrm{tel}}$ | $\epsilon_{\mathrm{CR,reco}}$ |
|---|---|---|---|---|---|
| Standard (no $\theta^2$) | 48.9 | 85.8 | 2.2 | 2.4 | 6.1 |
| Standard | 34.4 | 60.4 | 0.009 | 0.009 | 0.02 |
| Hard (no $\theta^2$) | 15.3 | 79.7 | 0.21 | 0.23 | 1.3 |
| Hard | 12.8 | 66.4 | 0.0007 | 0.0007 | 0.004 |

**Table 4.2:** Efficiencies in percent for the different sets of cuts with and without a $\theta^2$ cut. The $\gamma$-ray Monte-Carlo simulations used for the determination of the $\gamma$-ray efficiencies ($\epsilon_\gamma$, $\epsilon_{\gamma,\mathrm{reco}}$) were simulated at a zenith angle of 20° and a camera offset of 0.5° with a power law energy spectrum of photon index 2.6. The background data are taken from off-runs taken at similar zenith angles and camera offsets.

real Cherenkov data directly, since the proton-rejection is so efficient that the Monte-Carlo statistics for protons are not sufficient. Table 4.2 summarises the efficiencies of the different sets of cuts for $\gamma$-rays and protons. The efficiencies are shown for standard and hard cuts with and without a $\theta^2$ cut (since this cut can be varied, depending on the extension of the emission region). Efficiencies are shown for Monte-Carlo $\gamma$-rays ($\epsilon_\gamma$), and for Monte-Carlo $\gamma$-rays that pass the cuts on the size and the nominal distance ($\epsilon_{\gamma,\mathrm{reco}}$). Note that all Monte-Carlo $\gamma$-rays provide at least two telescopes triggered and with data. For off-source data the efficiency are shown for all events ($\epsilon_{\mathrm{CR}}$), for all events with at least two telescopes providing data ($\epsilon_{\mathrm{CR},>2\mathrm{tel}}$) and for all events passing the size and the nominal distance cut ($\epsilon_{\mathrm{CR,reco}}$). The data used for the estimation of the background rejection efficiency were taken at zenith angles of $\sim 20°$ and camera offset of 0.5° to match the Monte-Carlo simulations used.

## 4.2 Background Modelling

After the selection of the dataset, the calibration, and the Hillas parametrisation of images, the $\gamma$-ray signal has to be extracted from the vast background of cosmic-ray induced air showers. To reduce the background level significantly without cutting away too much of the signal, appropriate cuts on selected parameters have to be used as described in section 4.1.5.

After application of image selection cuts, the events passing cuts are so-called *$\gamma$-ray like*, meaning that the events look like $\gamma$-rays in terms of the parameter used for cuts. Different background estimation techniques can be used to determine the $\gamma$-ray-like background that is still contained.

### 4.2.1 Signal determination

A $\gamma$-ray signal consists of a number of excess events $N_\gamma$ above the background level, consisting of cosmic-ray induced air showers. Since $N_\gamma$ cannot be determined by counting events on an event-by-event basis, a statistical approach is used, by which the number of events $N_{\text{on}}$ in a circular region (defined by $\theta_{\text{cut}}$) is compared to the number of background events $\alpha N_{\text{off}}$ estimated for that circular region on the basis of the number of events $N_{\text{off}}$ in a suitable off-source region. This approach has to be taken since $N_{\text{on}}$ also contains background events. The excess $N_\gamma$ can be estimated by

$$N_\gamma = N_{\text{on}} - \alpha N_{\text{off}} \tag{4.2}$$

with $\alpha$ being a normalisation factor. This background normalisation accounts for the fact, that the solid angle and/or the exposure time $t$ may differ for the on- and the off-source counts. Additionally, the acceptance $\epsilon_\gamma$ for $\gamma$-ray like showers varies within the field of view of the system (the position in the field of view being defined as $\psi_x, \psi_y$ in two rectangular directions), with zenith angle $\Phi$ and exposure time $t$. This has to be corrected for, if different regions in the field of view are used for the determination of $N_{\text{on}}$ and $N_{\text{off}}$. All these dependencies are fed into the background normalisation $\alpha$ as will be described in the following. To summarise, $\alpha$ can be written as:

$$\alpha = \frac{\int_{\text{on}} \epsilon_\gamma(\psi_x, \psi_y, \Phi, t) d\psi_x d\psi_y d\Phi dt}{\int_{\text{off}} \epsilon_\gamma(\psi_x, \psi_y, \Phi, t) d\psi_x d\psi_y d\Phi dt} \tag{4.3}$$

For *wobble*-observations, in which the background is estimated from within the field of view and therefore the exposure time is the same and the zenith angle very similar for the on- and off-data, this can be reduced to:

$$\alpha = \frac{\int_{\text{on}} \epsilon_\gamma(\psi_x, \psi_y, ) d\psi_x d\psi_y}{\int_{\text{off}} \epsilon_\gamma(\psi_x, \psi_y) d\psi_x d\psi_y} \tag{4.4}$$

The significance $S_\gamma$ of a signal above the background can determined by the approach given in Li & Ma (1983) as:

$$S_\gamma = \sqrt{2} \left( N_{\text{on}} \ln \left( \frac{(1+\alpha) N_{\text{on}}}{\alpha (N_{\text{on}} + N_{\text{off}})} \right) + N_{\text{off}} \ln \left( \frac{(1+\alpha) N_{\text{off}}}{N_{\text{on}} + N_{\text{off}}} \right) \right)^{1/2} \tag{4.5}$$

By determining $N_{\text{on}}$, $\alpha$ and $N_{\text{off}}$ for each position in a region of the sky, a two-dimensional excess and significance map of that region can be compiled. The background modelling starts with the histogram of reconstructed directions of all events as shown in Figure 4.6 (left) with the Galactic Centre region as an example (in the future referred to as *raw on-map*, containing in each histogram bin the number of $\gamma$-ray candidates $N$). A correlated

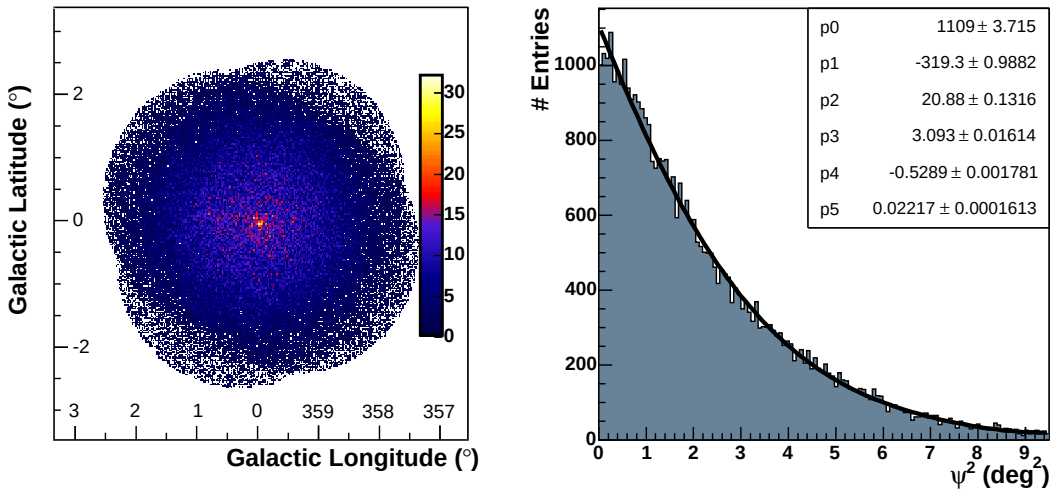


**Figure 4.6: Left:** Reconstructed directions of all $\gamma$-ray like events for the Galactic Centre region (raw on-map). The circular structure is introduced by the application of a cut on the reconstructed direction at 2° to avoid systematic effects at the edge of the field of view. The four different pointing positions around the Galactic Centre are apparent. **Right:** Distribution of squared angular distance $\psi$ of reconstructed event direction from the pointing direction of the system (acceptance curve), generated by adding up several runs (but always with respect to the pointing direction of the given run).

on-map (containing $N_{\mathrm{on}}$ for each test position) is constructed from the raw on-map by filling in each bin the number of events with reconstructed direction in a circle with radius $\theta$ around the centre of this bin:

$$N_{\mathrm{on}}(i,j) = \sum_{k,l} N(k,l) \qquad : (k,l) \in \text{Circle} \quad r = \theta \tag{4.6}$$

To determine the normalisation factor $\alpha$ and the background level (for the $\alpha$-map and the off-map), different techniques can be applied as will be shown below. Common to all background techniques is that it is important to avoid contamination by a $\gamma$-ray signal in the background region. Therefore exclusion regions $R_{\mathrm{ex}}$ were defined around positions of all known $\gamma$-ray sources. These regions were excluded in the estimation of the background levels, and the normalisation factor $\alpha$ correspondingly adjusted.

### 4.2.2 The system acceptance

As can be seen from equation 4.4, the normalisation factor $\alpha$ generally depends on the acceptance $\epsilon_\gamma$ for $\gamma$-ray like showers. This acceptance function is not homogeneous within the field of view. In fact it drops rather rapidly towards the edge. This is to be expected, since the phase space for shower images pointing to a given position in the camera decreases towards the edge. For any background determination method, for which different

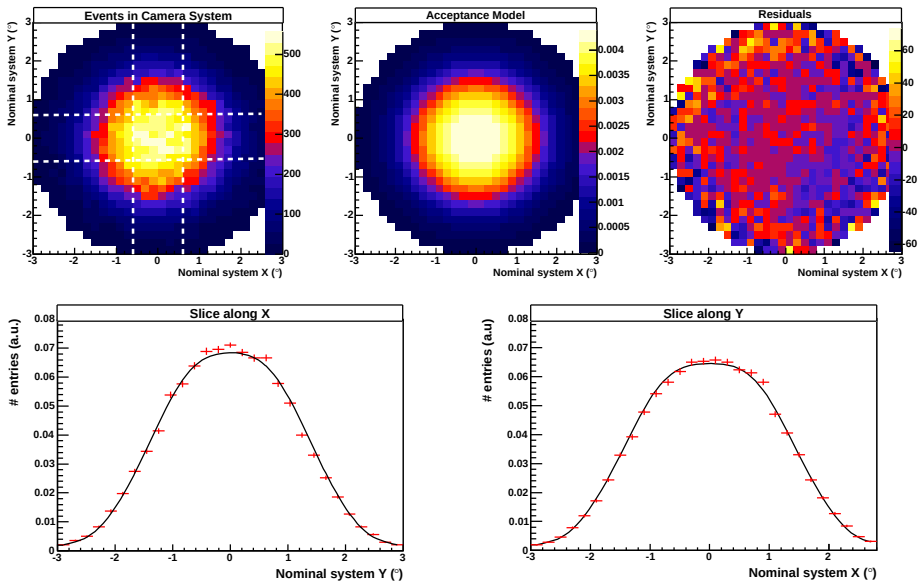


**Figure 4.7: Top Left:** Reconstructed directions of all $\gamma$-ray like events in the field of view (nominal system) in degrees for a target on the Galactic Plane without bright $\gamma$-ray sources in the field of view (centered on $l = 357.0°$, $b = 0°$). **Top Centre:** Model for the camera acceptance in the same system, generated by adding up the run-wise acceptance model curves. **Top Right:** Residuals between the reconstructed directions as shown in the top left panel and the acceptance model as shown in the top centre panel in percent. **Bottom:** Slices through the reconstructed directions (red) as shown in the top left panel and through the acceptance model (black) as shown in the top centre panel through the model. The width of the slices is 1.2° and is shown in the top left panel. **Bottom Left:** Slice along the x-direction. **Bottom Right:** Slice along the y-direction.

positions in the field of view are used to estimate the background, the relative acceptance function must be known precisely. It should be noted that we require only relative acceptance corrections.
Figure 4.6 (left) shows the distribution of reconstructed directions for $\gamma$-ray-like events, passing all cuts. The acceptance drops from the centre toward the edge of the field of view. To simplify equation 4.4, in the following the acceptance function was assumed to be radially symmetric for each single pointing (only a function of the distance $\psi$ to the centre of the field of view) and modelled by fitting the distribution of the angular distance between the event direction and the pointing direction of the system by a 5th order polynomial function as shown in Figure 4.6 (right). The background normalisation $\alpha$ simplifies for radial symmetry of the $\gamma$-efficiency $\epsilon_\gamma$ to:

$$\alpha = \frac{\int_{\text{on}} \epsilon_\gamma(\psi) d\psi}{\int_{\text{off}} \epsilon_\gamma(\psi) d\psi} \tag{4.7}$$

A simple check of the radial symmetry for a field of view on the Galactic Plane without

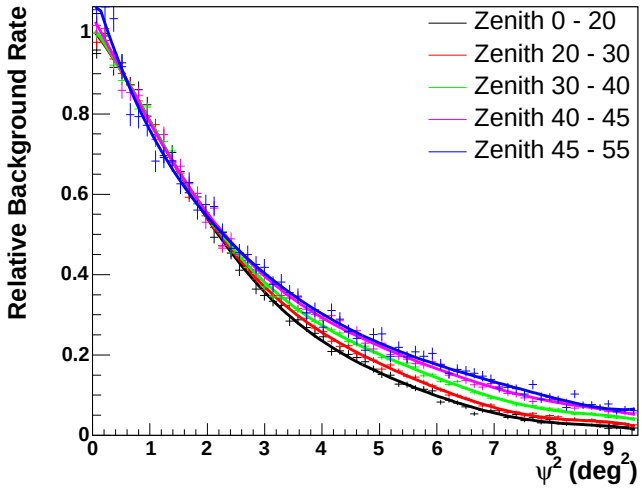


**Figure 4.8:** Model for the acceptance curve for different zenith angle bands, derived from off-runs or runs with no strong $\gamma$-ray source within the field of view.

strong $\gamma$-ray sources (centered on $l = 357.0°$, $b = 0°$) is shown in Figure 4.7. The top row shows the two-dimensional distribution of the reconstructed directions in the field of view (nominal system) on the left and the corresponding model for the camera acceptance, generated from the acceptance curve of the single pointings in the central panel. The deviation between the measured camera acceptance for this dataset and the assumed one, given by the model of the camera acceptance (derived from off-source runs) is shown in the top right panel expressed by the residuals between the two distributions in percent. A linear gradient at the 20% level can be seen from top left to right bottom, a direction that does not correspond to the zenith direction. Linear gradients have not been taken into account in this work and introduce a systematic error in the determination of the acceptance curve. The bottom row shows slices of width 1.2° along the x-direction (left) and along the y-direction(right) through the histogram of the reconstructed directions (in red) and through the acceptance model histogram (in black). The position of the slices are indicated as white dashed lines in the top right panel. The histograms are normalised by the integral of the entries in the slices. The agreement between the slices shows that the radial asymmetry is a reasonable assumption. The acceptance curve depends on various parameters as will be discussed in the following.

### 4.2.3 The zenith dependence of the acceptance

Figure 4.8 shows the acceptance function, derived from off-runs for different zenith angle bands. A slight steepening with decreasing zenith angle can be seen in this figure. This is due to the images getting more compact for larger zenith angles and therefore the images move slightly further out before being rejected by the nominal distance cut. The acceptance curves shown in Figure 4.8, are used in the following as a model for the acceptance function. These curves are normalised to the integral in the inner 1°.

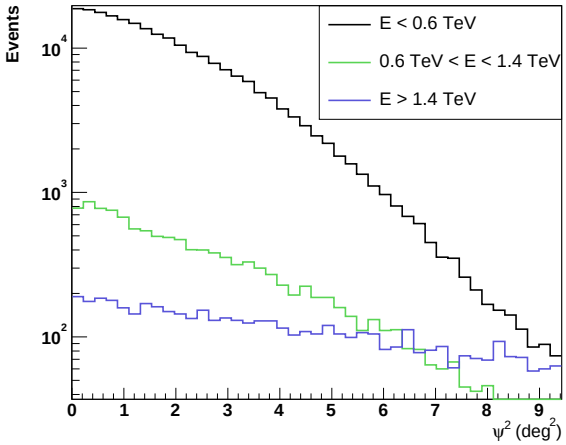


**Figure 4.9:** Acceptance curve for different energy bands.

### The energy dependence of the acceptance

An additional complication in the usage of the radial acceptance function arises from the fact that the acceptance changes with energy. Figure 4.9 shows in a logarithmic representation the acceptance curve for three different energy bands ($E < 0.6$ TeV, 0.6 TeV $< E <$ 1.4 TeV, $E >$ 1.4 TeV). With increasing energy the overall number of events decreases and the acceptance curve becomes flatter. For larger energies, showers with larger impact distances still trigger the telescopes. Therefore the probability for reconstructing the direction of an event further out from the centre of the field of view increases, which flattens out the acceptance curve. For spectrum determination using background methods that make use of the relative acceptance function within the field of view, the energy dependence of the acceptance should be taken into account; such methods are, however, not used here.

### The effect of bright stars

All background estimates presented here rely on the homogeneity of the ($\gamma$-ray or hadron) acceptance across the FoV. While detector acceptance inhomogeneities are typically of the order of 3% or less, they may reach 20% in special cases such as large zenith angle observations or strong sky brightness variations due to stars. Figure 4.10 shows as an example the event rate in arbitrary units as a function of the distance to bright stars in the FoV, for different bands of stellar V-band magnitude. The curves were derived from the H.E.S.S. Galactic Plane survey dataset, averaging over all stars in the respective magnitude interval. As can be seen from Figure 4.10, for stars with v-magnitude smaller than 5, the event rate at the position of the star decreases noticeably. This effect can be explained as a consequence of the camera switching off pixels if a bright star is illuminating the pixel. For events in which the shower core is located close to one of the telescopes, the event for that telescope will have a hole in the middle of its Hillas ellipse due to pixels being switched of by the star. For two-telescope events the shower core is frequently close to one of the telescopes, since the spacing of the telescope is close to the diameter of

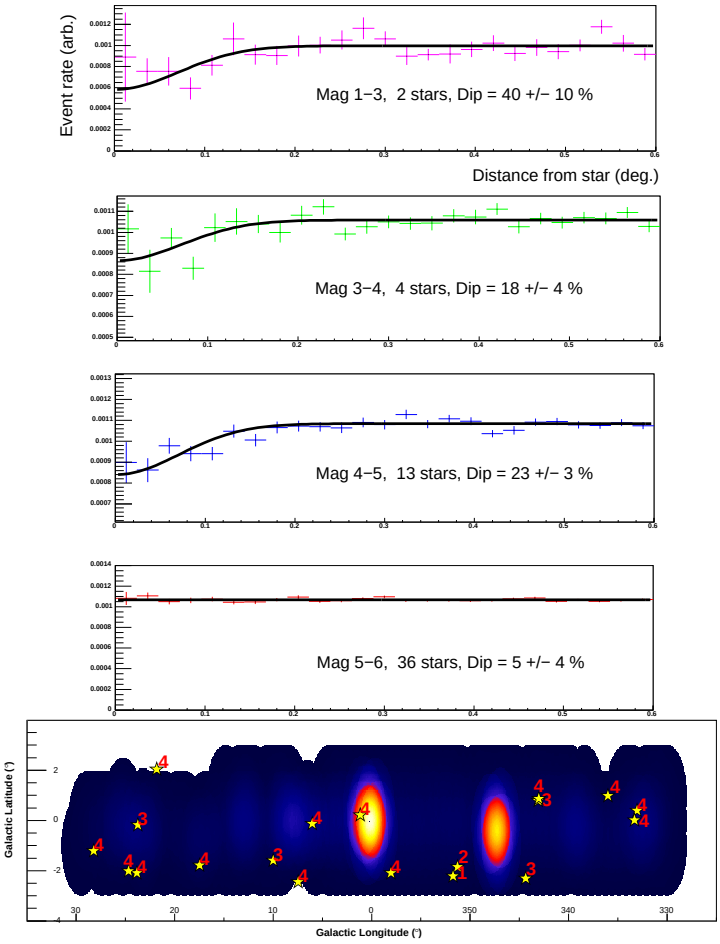


**Figure 4.10:** Effect of bright stars on the event rate of the system for standard cuts. Shown is the event rate in arbitrary units as a function of the distance to bright stars for different V-magnitude bands. The bottom panel shows the position of the stars in the Galactic Plane survey region.

the enhanced ring of the Cherenkov light pool. An event with the hole in the middle of the Hillas ellipse might a) be thrown away by the image cleaning or b) fail the shape cuts‘. Therefore less events are reconstructed in the direction of the star. The effect increases with increasing brightness of the star, but it should be noted, that in the 1-3 V-magnitude band only 2 stars are present in the whole survey data as can be seen from the bottom panel of Figure 4.10 and these stars are located well off the Galactic Plane. The histograms shown in Figure 4.10 are derived using standard cuts. For hard cuts the effect is less severe. This is evident, since the influence of individual pixels that are switched off is smaller for the bigger images present with the increased size cut of 200 pe. For the hard cuts, no dip of stars can be seen in the Magnitude 4 to 5 band. For the Magnitude 3 to 4 and magnitude 1 to 3 band, the event statistics for the hard cuts is insufficient to draw firm conclusions. The effect of stars has not been taken into account in the analysis and this might cause a dip in the significance and excess map at the positions of bright stars with a ring of positive significances and excesses around this dip.

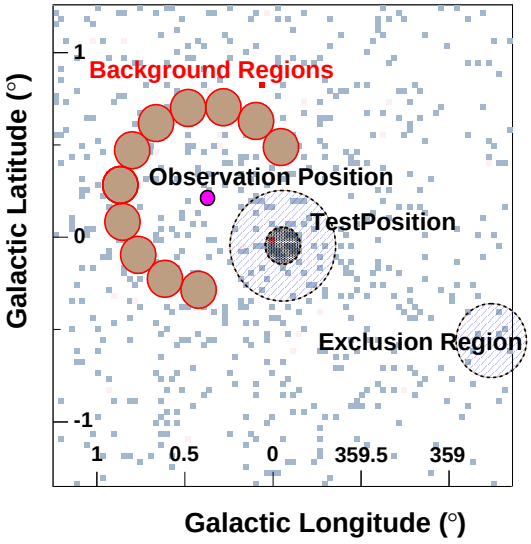


**Figure 4.11:** Off regions used in the region background model for the Galactic Centre region for a run with wobble offset 0.5° from the Galactic Centre. Also shown is the observation position (as purple circle) and two exclusion regions in the Galactic Centre area in dashed blue.

### 4.2.4 One-dimensional Region Background Model

For *wobble*-observations, the position of the source is offset from the centre of the field of view, and, under the assumption of rotational symmetry in the system acceptance, a background estimation from within the same field of view can be provided. The simplest approach in this regard is to mirror the position of the source across the centre of the field of view. In this case the single background position of the same area as the on-region (given by the $\theta$ cut), is located at the same distance to the centre as the on-region and thus has the same acceptance as the on-region. In order to reduce the statistical fluctuations in the background counts $N_{\text{off}}$, it is desirable to use an area as off-region that is larger than the on-region. This increase in area is accounted for in a decrease in the $\alpha$ normalisation. For this purpose a number of off-regions (of the same size and shape as the on-region) are distributed on a ring around the centre of the field of view, with the radius of this ring being equal to the wobble offset as illustrated in Figure 4.11. On this ring, a maximum number of off-regions $n_{\text{off}}$ are inserted, depending on the wobble offset and the size of the on-region and taking into account possible exclusion regions as described above. A minimum distance between the on- and off-regions of 0.1° is required to avoid contamination of the off events with $\gamma$-rays. For a wobble offset of 0.5° and a hard point source $\theta$-cut of 0.1°, a typical number of $n_{\text{off}} = 11$ off-regions can be fit onto the ring. $N_{\text{off}}$ is calculated by summation of all events within the off regions. The background normalisation $\alpha$ is simply given by the ratio of the solid angles $\alpha = 1/n_{\text{off}}$. No correction for the acceptance is needed since regions with same offset from the centre of the field of view are used. It should be noted, that the advantage of this method is that it is independent of the exact shape of the acceptance function. It simply relies

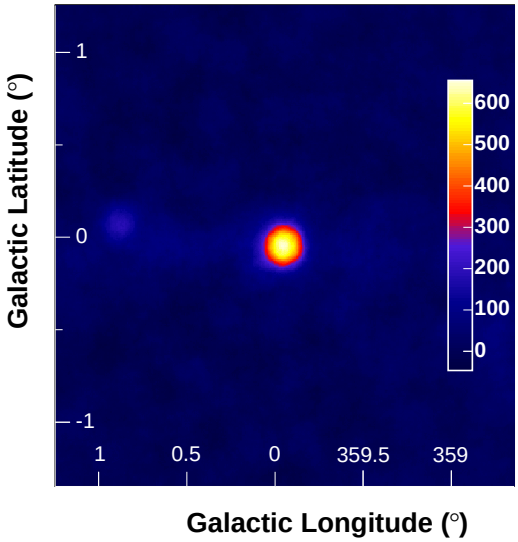


**Figure 4.12:** Excess map of the Galactic Centre region generated with the acceptance background technique.

on the assumption of radial symmetry of the acceptance. Additionally the distribution of offsets from the centre in the on- and off-events is the same. This makes the region background model especially suited for the background estimation in conjunction with the determination of energy spectra.

### 4.2.5 Two-dimensional Acceptance Background

To derive a two-dimensional excess map of a region on the sky in $\gamma$-rays, the background for each position in the sky must be determined. The simplest approach for a background determination technique is to account only for the fact, that the acceptance changes within the field of view and use the acceptance map as background model. The acceptance curve models for the different zenith angle bands as shown in Figure 4.8 are used for the background estimation. Given an observation at a certain zenith angle, a model background is created by interpolating linearly between the two nearest zenith angle bands. A run-wise two-dimensional background map is then created by rotating the model background around each pointing direction of the system. The normalisation factor $\alpha$ is arbitrary and should be derived in a way that the on- and the off-map agree away from $\gamma$-ray sources. Figure 4.12 shows an excess map of the Galactic Centre region, generated using the acceptance background technique. It should be noted, that this background estimation technique is less robust than other two-dimensional background methods, since it is susceptible to linear gradients in the system acceptance.

### 4.2.6 Ring Background Model

Another background determination technique is the *Ring Background Model*. In this method, the off-counts $N_{\text{off}}$ for a given position in the sky are derived from a ring around

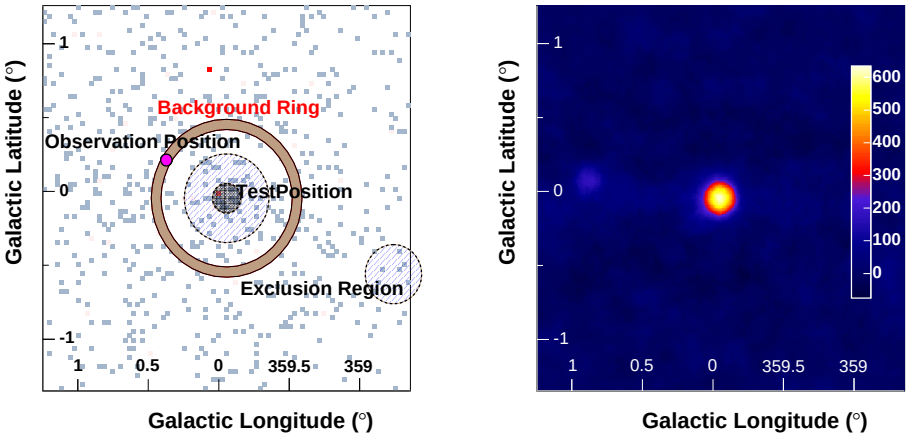


**Figure 4.13: Left:** illustration of the background region used for the analysis with the ring background technique. **Right:** Excess map of the Galactic Centre region generated with the ring background technique.

that position in the sky. The off-map is derived by summing all events in a torus of radius $R_{\text{ring}}$ in the raw on-map.

$$N_{\text{off}}(i,j) = \sum_{k,l} N(k,l) \qquad : (k,l) \in \text{Ring} \wedge (k,l) \notin R_{\text{ex}} \tag{4.8}$$

The mean radius of the torus has typically a value of 0.5 °, the inner and outer radius are adapted such that the ratio of the area of on-region to off-region is $\approx 1/7$. Within the ring the acceptance can not be assumed to be constant, since the ring covers areas with different offsets from the observation position. Therefore an acceptance function must be used in the determination of the normalisation $\alpha$ for each bin. For the calculation of $\alpha$ the acceptance map is integrated in a circle of radius $\theta$ and in a ring with the same size as in the calculation of $N_{\text{off}}$, again taking into account exclusion regions $R_{\text{ex}}$. The ratio of these two values gives the normalisation factor $\alpha$. In this way, the ratio of the areas is taken into account as well as the system acceptance for the grid points that are used for the background estimation.

$$\alpha(i,j) = \frac{\sum\limits_{k,l}^{k,l \in \text{circle}} \epsilon(k,l)}{\sum\limits_{k,l}^{k,l \in \text{Ring}} \epsilon(k,l)} \qquad (k,l) \notin R_{\text{ex}} \tag{4.9}$$

with $\epsilon(k,l)$ denoting the content in the acceptance map of bin $k,l$. Figure 4.13 shows an excess map of the Galactic Centre region, generated using the ring background technique. The ring background method has the advantage of providing a simple prescription for the background determination. It is not very sensitive to deviations of the actual relative acceptance from the model acceptance function, since it only relies on the relative normalisation in a limited nearby area around the source bin in the FoV. Any linear gradients in

the system acceptance are averaged out. However, when testing larger source extensions, larger ring radii are required, demanding better accuracy for the relative acceptance correction across a larger portion of the FoV. For the determination of the energy spectrum, this method is disfavoured, since the acceptance curve changes with energy (as shown in Figure 4.9). Additionally, the off events have a different distribution of offset from the centre of the field of view than the on events. Since the effective areas used for the spectral analysis depend on the camera offset, the different offset distribution introduce an additional systematic uncertainty. Finally, the problem of changing acceptance with energy as shown in Figure 4.9 has to be taken into account when determining an energy spectrum using this technique. The systematic error on the photon index determination has been found to be 0.05 for a wobble offset of 0.5°. This number was derived by placing a strong Monte-Carlo $\gamma$-ray source artificially in an empty field of view.

### 4.2.7 Template Background Model

An alternative technique is employed by the *Template* background model. Instead of estimating the background from spatially different regions in the FoV using $\gamma$-ray candidates, the background level is estimated using events that are normally removed by the cosmic-ray background rejection criterion based on the scaled image width and length, but with reconstructed directions falling within the on-region (Rowell, 2003). For this purpose two raw sky maps are filled. One for the *signal* regime (containing all events that pass the standard $\gamma$-selection cuts), ie. the correlated on-map (as for the other techniques), the other for the *background* regime (containing all events that pass a background cut, which selects events which are far away from $\gamma$-ray like events in the scaled parameter phase space. The number of off events $N_{\text{off}}$ can directly be taken from an integration in a circle with radius $\theta$ in this background map. For the normalisation factor $\alpha$ a radial acceptance curve for the background regime, as well as for the signal regime must be determined. The normalisation factor $\alpha$ takes into account the relative acceptance of the two regimes (Rowell, 2003). The template background technique has the advantage that it is better suited to very extended sources than the ring background method, since no need for an enlarged ring with increasing systematic uncertainties of the relative acceptance on the ring applies. It is, however, sensitive to uncertainties in the relative acceptance determination between the signal and background regime across the FoV. For the estimation of energy spectra the background estimate must consist of events with a similar distribution of estimated energies to the background events of the source region. The template background estimate does not meet this criterion since the events in the background regime will differ in estimated energy from those in the signal regime. Also the problem of the acceptance curve changing with energy is present as in the case of the ring background but more severely since it applies to the signal as well as to the background regime. Therefore this method is not used to reconstruct energy spectra. Figure 4.14 shows an excess map of the Galactic Centre region, derived using the template background technique.
To summarise the background modelling technique, it should be noted, that it is appropriate to have different background estimation techniques, since different purposes require different estimations. The one-dimensional region background model is currently used to derive energy spectra, while the ring-background is a robust tool to derive two-dimensional

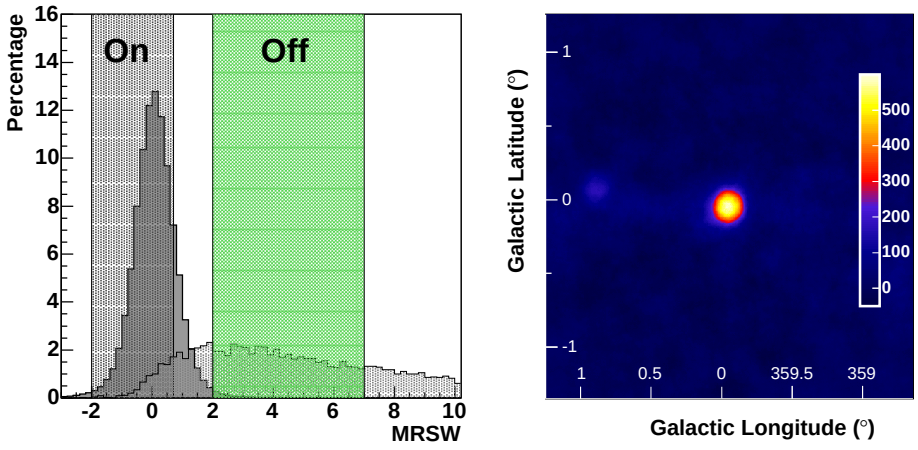


**Figure 4.14: Left:** Illustration of the events, used for the on- and for the off-estimation for the template background method in the different MRSW regimes. **Right:** Excess map of the Galactic Centre region generated with the template background technique.

excess and significance maps of sources that are not too extended with respect to the PSF ($< 0.2°$). For very extended sources, the template background is a more appropriate tool. For the Galactic Centre dataset the different background estimation techniques are in good agreement as can be seen from the different excess maps.

## 4.3 Position Fitting

For the exact localisation of the $\gamma$-ray signal, several source fitting techniques have been implemented and is described in the following. All methods assume that the centroid of the $\gamma$-ray emission is not energy dependent. The source position and intrinsic width $\sigma_{\text{source}}$ of the source were fit simultaneously under the assumption that the emission region exhibits an intensity profile of a radially symmetric Gaussian form, given by:

$$I(\theta^2) = K_{\text{source}} e^{-\theta^2/2\sigma^2_{\text{source}}} \tag{4.10}$$

For the fitting procedure, this single-Gaussian emission profile (of width $\sigma_{\text{source}}$) was convolved with a double Gaussian of the form $\propto K_1 e^{\theta^2/2\sigma_1^2} + K_2 e^{\theta^2/2\sigma_2^2}$, describing the PSF of the system (derived from Monte-Carlo simulations as will be shown in section 4.5.1). This convolution can be written as:

$$N_\gamma(x,y) = \text{PSF}_{\text{2D}}(x,y) = K_{\text{source}} \left[ e^{-\frac{\theta^2}{2(\sigma_1^2+\sigma^2_{\text{source}})}} + \frac{K_2}{K_1}\frac{\sigma_2^2}{\sigma_1^2}\frac{\sigma_1^2+\sigma^2_{\text{source}}}{\sigma_2^2+\sigma^2_{\text{source}}} e^{-\frac{\theta^2}{2(\sigma_2^2+\sigma^2_{\text{source}})}} \right] \tag{4.11}$$

with

$$\theta^2 = [(X_0 - x)a]^2 + (Y_0 - y)^2 \tag{4.12}$$

where x, y is a coordinate system on the sky (Galactic or RADec coordinates) and a scale factor $a = 1/\cos(y)$, resulting from the spherical character of this coordinate system on

the sky with non-Cartesian metrics. Free parameters of the fit are the source position $X_0$, $Y_0$, the source width $\sigma_{\text{source}}$ and the normalisation $K_{\text{source}}$. The PSF used for the fitting was taken from Monte-Carlo simulations matching the mean zenith angle and offset of each dataset as closely as possible. It should be noted that the model PSF used for the fitting procedure is consistent with the excesses observed for the point-like sources the Crab Nebula and the active galaxy PKS 2155–304 (Aharonian et al., 2005e).

### 4.3.1 Fit to the excess map

The uncorrelated two-dimensional excess map is fit with $\text{PSF}_{\text{2D}}(x, y)$. For the fit to the excess map, a likelihood fit can not be used since the excess map does not contain counting statistics. Therefore the binning needs to be coarse enough to have sufficient statistics in each bin, such that a Gaussian approximation is valid. The disadvantage of this approach is that a systematic error stemming from the binning of the events might be introduced. A typical value for the bin size used in this approach is 0.02°. In addition to the approach described here, an elongated Gaussian can be fit to the excess map to test for an emission region with an elliptical shape.

### 4.3.2 Fit to the raw on-map assuming a flat background

Here the raw on-map is fit with the same function as in the fit of the excess map (see section 4.3.1) with an additional constant fixed offset $B_0$. This constant offset is derived from a ring around the source position. In the raw on-map Poisson statistics are applicable, therefore a likelihood fit can be used and fine binning is desirable to reduce possible systematic effects arising from binning. A typical value for the bin size used in this approach is 0.005°. The function used for the fitting is of the form:

$$N_\gamma(x, y) = \text{PSF}_{\text{2D}}(x, y) + B_0 \tag{4.13}$$

### 4.3.3 Fit to the raw on-map, using a Gaussian background

Again in this method the raw on-map is fit with a function similar the fit to the excess map, but with a non-constant offset. This offset is determined in a previous step from a fit of a two-dimensional single Gaussian to the background map (resulting in the fit parameters $K_{\text{back}}$, $X_{\text{back}}$, $Y_{\text{back}}$ and $\sigma_{\text{back}}$). This background map is generally determined by the ring background method but could also come from any other background method. Again a likelihood fit is used and fine binning of size 0.005° is appropriate. The function used for the fitting is of the form:

$$N_\gamma(x, y) = \text{PSF}_{\text{2D}}(x, y) + K_{\text{back}} e^{-\left[((X_{\text{back}}-x)a)^2+(Y_{\text{back}}-y)^2\right]/2\sigma^2_{\text{back}}} \tag{4.14}$$

Free parameters in this fit are the again source position $X_0$, $Y_0$, the source width $\sigma_{\text{source}}$ and the normalisation $K_{\text{source}}$. Figure 4.15 shows a background map as determined from the ring background model, along with the resulting two-dimensional fit of a Gaussian.

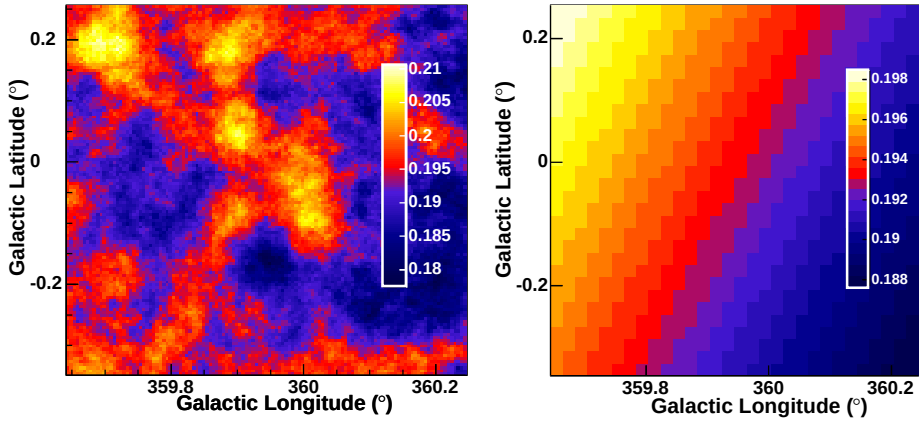


**Figure 4.15: Left:** Background map, determined by the ring background model for the Galactic Centre region.**Right:** Two-dimensional fit of a Gaussian to the background map.

### 4.3.4 Test of the methods using a Monte-Carlo simulation

The fitting methods described above were tested using a Monte-Carlo simulation of a Gaussian emission region with width $\sigma_{\text{source}}$ to generate the excess and/or raw sky maps on which the different fitting algorithms were applied. The procedure to generate these Monte-Carlo maps is as follows:

- Start with a background map (e.g. as determined from the ring background method). This background map has been generated from real data, taking into account exclusion regions for possible sources in the field of view. The advantage of using a real background map determined from data is that the fitting procedure is tested under realistic conditions.

- Fill the raw sky map (with a binning adapted to the fitting algorithm under test) by sampling from this background map. The number of sampled events was adjusted such that the number of events per bin in the resulting raw sky map is realistic.

- A signal is added to the raw sky map by randomly sampling from a Gaussian with a specified width $\sigma_{\text{source}}$, numerically smeared with the PSF of the instrument (for the zenith angle and offset corresponding to the observations associated with the background map that was used). The strength of the signal was varied by specification of the total number of excess events $N_\gamma$.

- From the raw on-map and the background map an excess map can be created. At this stage all the two-dimensional maps necessary to test the fitting procedure are created. Figure 4.16 shows an excess map, generated with this procedure (with an excess $N_\gamma$ of 30000 and a source width $\sigma_{\text{source}}$ of 0.04).

- The fitting procedures as described above is applied to these maps and is repeated many times and the results stored.

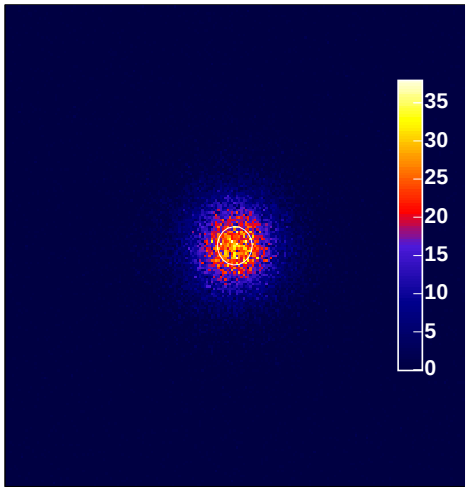


**Figure 4.16:** Excess map, generated using the Monte-Carlo simulation procedure as described in 4.3.4 for an excess of 30000 counts and a source width $\sigma_{\text{source}}$ of 0.04° (shown as white circle).

The main question to be answered by this Monte-Carlo approach is, whether the statistical errors determined in the fitting procedure are correct. As an example, the results obtained using the fit method described in section 4.3.3 (Fit to the raw on-map, using a realistic background) will be given . This fitting procedure is the default algorithm, since it proved to be most robust. It was used for the determination of the position and source width of the Galactic sources described later. The background map as determined using the ring background method for the new source HESS J1813-178 was used. The other fit methods yield comparable results.

Figure 4.17 shows as an example the results of the Monte-Carlo simulation for a typical excess of $N_\gamma = 300$ events with a width $\sigma_{\text{source}}$ of 0.04° and hard cuts. The histograms show the deviation of the reconstructed with respect to the true value for Right Ascension (RA) in blue, Declination (Dec) in Red and the width $\sigma_{\text{source}}$ in green. A very small deviation of the mean from 0 is present in the reconstructed Declination.

To study the effect of the size of the source on the quality of the fit, an excess of $N_\gamma = 600$ in case of the standard cuts and $N_\gamma = 300$ in case of the hard cuts was used in the following and $\sigma_{\text{source}}$ was varied in steps of 0.01° from 0° to 0.2°. The factor of 1/2 between standard and hard cuts is a typical value for the ratio of excesses for an $E^{-2.0}$ spectrum.

Figure 4.18 (left) shows the angular distance of the reconstructed source position as a function of the width of the source $\sigma_{\text{source}}$ for hard and standard cuts. It can be clearly seen, that the accuracy with which the position is reconstructed deteriorates with increasing $\sigma_{\text{source}}$. This is expected, since for a fixed excess as used here, the signal to noise decreases and additionally the error on the mean degrades like $\propto \frac{\sigma_{\text{source}}}{\sqrt{(N)}}$. Also seen from this figure can be that the hard cuts seem to give better results on average, mainly because of a better background suppression and better angular resolution. For $\sigma_{\text{source}} < 0.1°$, the

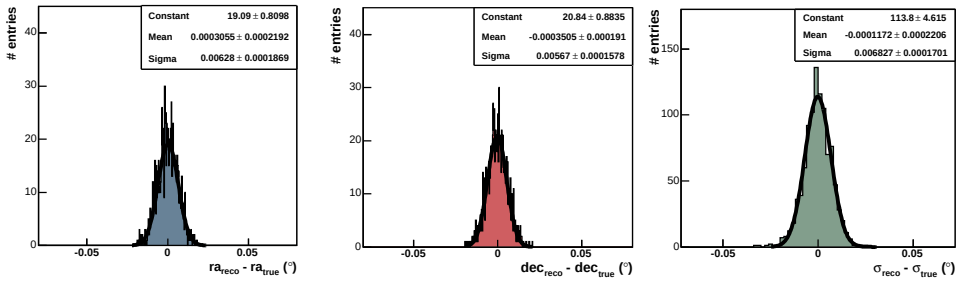


**Figure 4.17:** Example of the distribution of the deviation of the reconstructed from the true position and source width for one parameter set ($N_\gamma = 300$, hard cuts, $\sigma_{\text{source}} = 0.04°$. A small bias is present in the reconstructed Declination, the other parameters behave as expected.

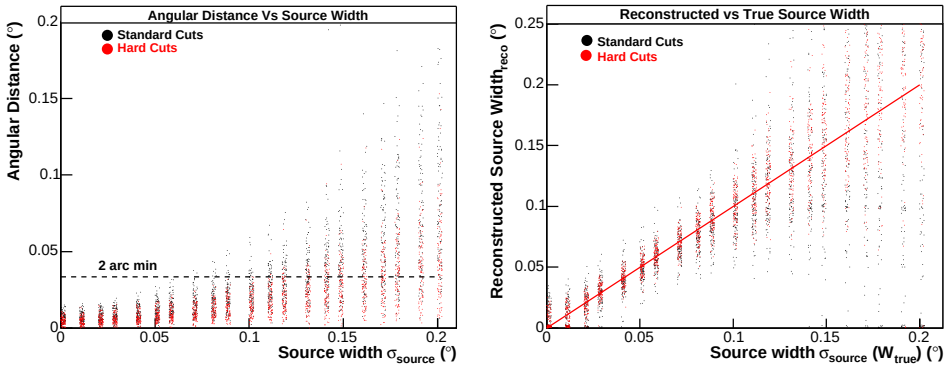


**Figure 4.18: Left:** Angular error in degrees of the reconstructed position of the simulated excess with constant number of excess events $N_\gamma = 600$ for standard cuts (red) and $N_\gamma = 300$ for hard cuts (black). **Right:** Reconstructed source width $\sigma_{\text{source}}$ as a function of true source width again for the two sets of cuts. The red line shows a one-to-one correspondance.

position accuracy is better than 2 arc minutes. Figure 4.18 (right) shows the reconstructed source width $\sigma_{\text{source}}$ plotted as a function of true source width. The red line shows the desired case of a one-to-one correlation. Again hard cuts perform better in the sense that the spread around the straight line is smaller than for standard cuts. A general agreement between the reconstructed and true widths is visible, again deteriorating with increasing source width.

To summarise this behaviour, Figure 4.19 shows again for the two sets of cuts, the rms error ($\delta$) from the true value for the RA position, the Dec position and the source width $\sigma_{\text{source}}$, defined as:

$$\delta^2 = (< true - reco >_{\text{mean}})^2 + (< true - reco >_{\text{rms}})^2 \tag{4.15}$$

Again the better performance of the hard cuts, as well as the deterioration with increased $\sigma_{\text{source}}$ is apparent.

To check the statistical errors returned from the positional fits, the deviation of the reconstructed value from the true value in terms of the statistical error on the reconstructed

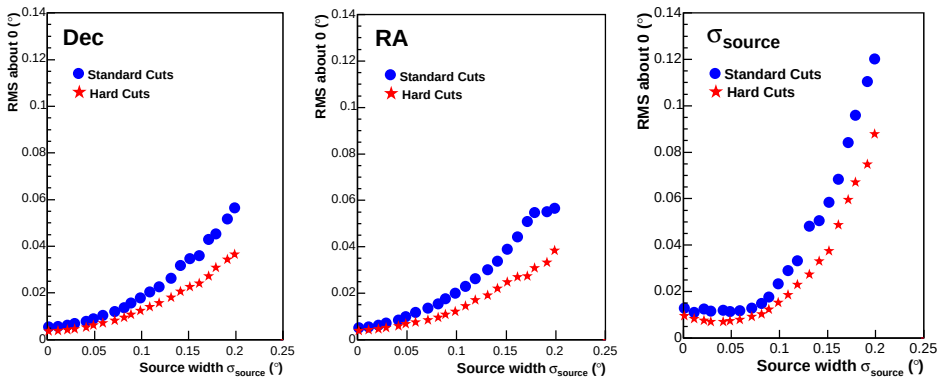


**Figure 4.19:** rms about zero deviation $\delta$ for the three different reconstructed parameters as a function of true source width $\sigma_{\text{source}}$. The expected deterioration in resolution with increased source width is apparent.

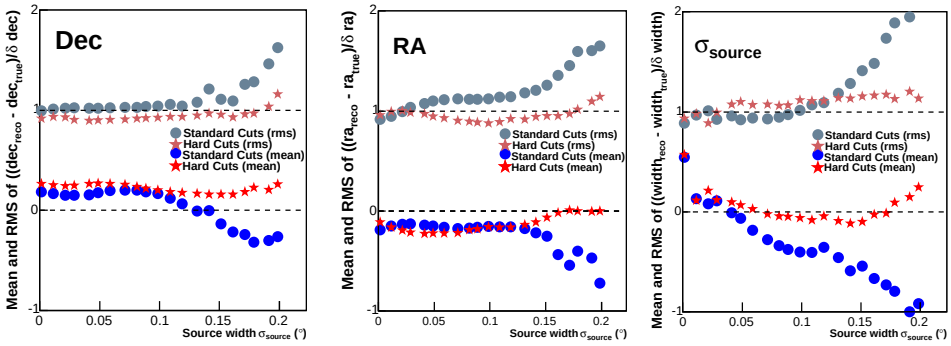


**Figure 4.20:** Mean and rms of Pull distribution as defined in the text for the relevant parameters of the position fit for standard and hard cuts.

value can be plotted. The mean and rms of the so-called *pull*-distribution are shown in Figure 4.20. The pull-distribution is given by $(X_{\text{reco}} - X_{\text{true}})/\Delta X_{\text{reco}}$ where $X$ can be either Right Ascencion or Declination or the reconstructed width and $\Delta X_{\text{reco}}$ gives the error on the reconstructed value. In the case of correctly assigned errors, the pull distribution should be a Gaussian with mean 0 and rms 1. It can be seen from Figure 4.20, that for hard cuts, the errors behave close to expectations for all widths and all reconstructed parameters, for standard cuts systematic problems start to appear above source size of 0.15°. A reason for this degradation could be that the extension of the source starts to be comparable to the scale at which the background is no more flat, which could introduce a systematic underestimation of the error. This effect would be less severe for hard cuts since in this case the background is strongly suppressed.

To summarise the systematic checks of the position fitting, the approach of fitting a Gaussian with a realistic background to the raw on-map yields reasonable results and behaves as expected. Generally, the hard cuts should be used for the position fitting, mainly because of the better background suppression and the improved angular resolution.

## 4.4 Spectrum Determination

The energy spectrum of VHE $\gamma$-ray sources provides valuable information on the acceleration mechanisms at work in these astrophysical objects. The differential energy spectrum (or differential flux $F(E)$) of a source is defined as the number of photons detected from the source $N_\gamma$ per unit area and time. It can be expressed as:

$$F(E) = \frac{dN_\gamma}{dE} = \frac{1}{t_{\text{live}} A_{\text{eff}}(E)} \frac{dN_\gamma}{dE} \tag{4.16}$$

where $A_{\text{eff}}(E)$ is the effective collection area of the instrument as will be described below and $t_{\text{live}}$ is the live time of the observation. The effective collection area $A_{\text{eff}}(E)$ describes the area within which the H.E.S.S. instrument could detect a flux of $\gamma$-rays assuming a detection efficiency of 100%.

### 4.4.1 Effective collection area for $\gamma$-rays

The effective collection area describes the detector efficiency of the H.E.S.S. instrument for the detection of $\gamma$-rays and must be determined from Monte-Carlo simulations. $A_{\text{eff}}$ depends on several parameters and can be expressed as:

$$A_{\text{eff}}(E, \Phi, \psi, \Theta) = 2\pi \int_0^\infty P(E, \Phi, \psi, \Theta, R) R dR \tag{4.17}$$

with $R$ being the distance of the shower core to the centre of the array and $P$ the probability of a $\gamma$-ray shower to be detected and pass all event selection cuts. The important quantity in this formula is the probability $P$, that describes the efficiency of the array and the analysis to select a $\gamma$-ray event. The effective area depends on:

- The energy $E$ of the shower.
- The zenith angle $\Phi$ of the shower, primarily via the change in distance between the shower maximum in the atmosphere and the detector.
- The azimuth angle $\Theta$ of the telescope pointing, since it reflects the orientation of the shower with respect to the Earth's magnetic field.
- The position in the field of view $\psi$, since the *gamma*-ray efficiency of the system drops with distance from the centre as described in section 4.2.2.

For a sample of simulated $\gamma$-rays the probability $P$ can be simply evaluated by calculating in energy bands of width $\Delta E$ the ratio of the number of $\gamma$-rays detected and passing all event selection cuts $n$ to the total number of simulated $\gamma$-rays $N$. At large distances $R = R_{\text{max}}$, the detection probability becomes insignificantly small and thus only showers with core locations within a circle of radius $R_{\text{max}}$ must be considered. Thus equation 4.17 simplifies to:

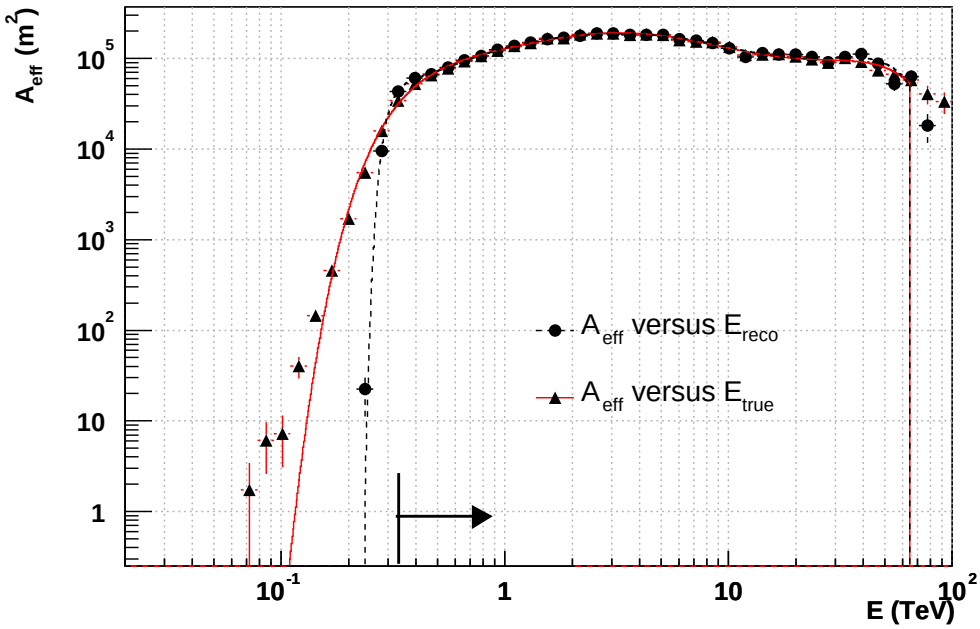


**Figure 4.21:** Effective Area $A_{\text{eff}}$ for $\gamma$-rays as a function of energy for a zenith angle of $\Phi = 20°$ a camera offset of $\psi = 0.5°$ and an azimuth angle of $\Theta = 180°$. The triangles show the effective area as a function of the true energy, along with the fit as a red line, the circles show the effective area as a function of the reconstructed energy along with a fit as a dashed black line. The arrow shows the safe threshold (as determined from the right side panel) above which energies are used for the calculation of source energy spectra.

$$A_{\text{eff}}(\Delta E, \Phi, \psi, \Theta) = 2\pi(\pi R^2_{\text{max}})\frac{n(\Delta E, \Phi, \psi, \Theta)}{N(\Delta E, \Phi, \psi, \Theta)} \tag{4.18}$$

Figure 4.21 shows the effective area determined using equation 4.18 after application of all selection cuts as a function of the true and the reconstructed shower energy for a typical zenith angle of observation $\Phi$ of 20°, an offset of the Monte-Carlo point source from the camera centre of 0.5° and a photon index for the simulated $\gamma$-rays of 2.0. At low energies the effective area exhibits a sharp rise towards a turnover, which roughly corresponds to the energy threshold of the instrument for this zenith angle and offset. At these low energies $A_{\text{eff}}$ is limited by the amount of Cherenkov light reaching the detector and by the cut on the total number of photoelectrons in a camera image (size cut). For energies larger than this threshold, the effective area $A_{\text{eff}}$ rises slowly until it reaches a maximum around 3 TeV. After this the $A_{\text{eff}}$ decreases gradually towards larger energies due to decreasing cut efficiencies at larger energies. Since the energy can only be reconstructed with limited precision, there is a difference in the effective area plotted as a function of the true energy and plotted as a function of the reconstructed energy. This effect can be described by the energy dependent bias as already described and defined in section 4.1.4 and equation 4.1

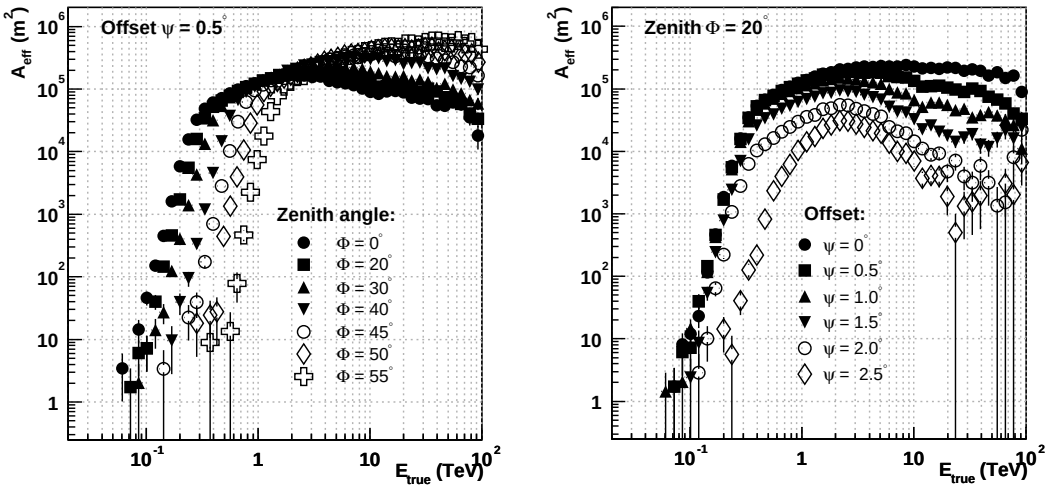


**Figure 4.22: Left:** Effective area $A_{\text{eff}}$ as a function of the true energy for $\gamma$-rays for different zenith angles $\Phi$, a camera offset of $\psi = 0.5°$ and an azimuth angle of $\Theta = 180°$. **Right:** Effective area $A_{\text{eff}}$ as a function of the true energy for $\gamma$-rays for different camera offsets $\psi$, a zenith angle $\Phi = 20°$ and an azimuth angle of $\Theta = 180°$.

and as shown in Figure 4.4 (right).
The energy bias depends on the zenith angle $\Phi$ and the camera offset $\psi$. To account for this reconstruction bias, the effective area as a function of the reconstructed energy is used for the determination of the energy spectrum of a $\gamma$-ray source. This correction is valid for a source with the same photon index as the Monte-Carlo simulated $\gamma$-rays ie. $\Gamma = 2$. The energy spectrum is only determined above the *safe* threshold $E_{\text{safe}}$, given by the energy, above which the energy bias drops below 20%.
The zenith angle and camera offset dependency of $A_{\text{eff}}$ is illustrated in Figure 4.22 for zenith angles $\Phi = 20°, 30°, 40°, 45°, 50°, 55°$ and camera offsets $\psi = 0.5°, 1.0°, 1.5°, 2.0°, 2.5°$. These histograms are fitted with an analytical function in order to reduce statistical fluctuations. For the calculation of the energy spectrum, an effective area is assigned to each event after reconstruction of energy, zenith angle $\Phi$ and camera offset $\psi$ by evaluating the function and interpolating linearly in $\cos\Phi$ and $\psi$. To account for the weak azimuth dependence of the effective areas, one set of effective areas for northernly and one for southernly observations is generally generated. For the target under consideration the corresponding northernly or southernly effective areas are used (targets with a declination $< -23°$ being denoted as southernly).

### 4.4.2 Calculation of Energy Spectra

After the generation of the effective area curves from Monte-Carlo simulations, the energy spectrum of a $\gamma$-ray source can be derived from equation 4.16. Since for a single event in the on-region it is not known whether it is a true $\gamma$-ray or a background event, a spectrum for all events in the on-region and a spectrum for all events in the off-region

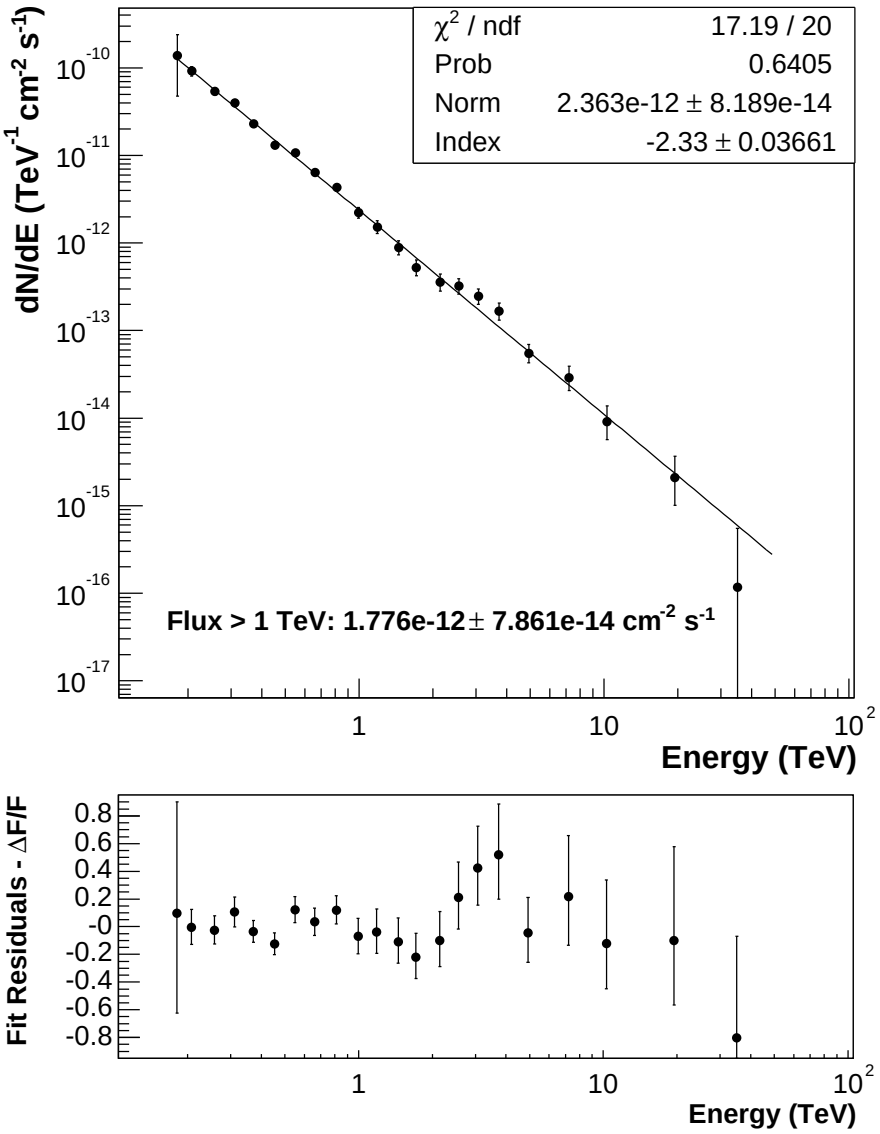


**Figure 4.23: Top** Differential energy spectrum of HESS J1745-290, the source at the Galactic Centre using 2004 data. The solid line shows the power-law fit to the data. **Bottom** Residuals of the power-law fit.

(defined by the background method that is used as described above) is created. The difference between these two spectra (taking into account the normalisation factor $\alpha$) yields the energy spectrum of the excess events and therefore of the source signal.
For the creation of the energy spectrum, the energy range is divided into fine energy bins of equal width $\Delta \log(E)$. For a given run only events with an energy above $E_{\mathrm{safe}}$ are considered. The reciprocal of the effective area for each event is filled into the histogram. The flux per energy bin of width $\Delta E$ is then finally given by:

$$F(\Delta E) = \frac{1}{t_{\mathrm{live}} \Delta E} \left\{ \sum_{i=1\ldots N_{\mathrm{on}}}^{E_i \in \Delta E} \frac{1}{A_i} - \alpha(\Delta E) \sum_{j=1\ldots N_{\mathrm{off}}}^{E_j \in \Delta E} \frac{1}{A_j} \right\} \tag{4.19}$$

where the normalisation $\alpha$ and the live time $t_{\mathrm{live}}$ are determined seperately for each energy bin and the effective area $A_{i/j} = A_{\mathrm{eff}}(E, \Phi, \psi)$ denotes the effective area for each particular event.
To ensure a minimum significance of each energy bin the finely binned on- and off-flux histograms are rebinned according to the source strength. For each energy bin the resulting flux value $F(E)$ was assigned to the energy $E$ given by the mean value of the energies in the bin weighted by $1/A_{\mathrm{eff}}$. All points in the final spectrum are required to have a flux above zero and a relative flux error $\Delta F/F < 1$. Finally the resulting differential energy spectrum is fit by a power law with Flux normalisation $F_0$ and photon index $\Gamma$:

$$F(E) = dN/dE = F_0 \left( \frac{E}{1\mathrm{TeV}} \right)^{-\Gamma} \tag{4.20}$$

The bias arising from using effective areas weighted with an energy spectrum of $E^{-2}$ instead of the measured photon index for a given source is of the order of 10% close to the threshold and decreases to less than 5% at higher energies for a wide range of photon indices (see e.g. Aharonian et al. (2005h), which shows the energy-resolved ratio of reconstructed flux to true flux for photon indices between 1.1 and 3.2). Figure 4.23 shows the differential energy spectrum for the source at the Galactic Centre, HESS J1745-290 derived using the reflected background technique.

## 4.5 Basic performance properties of the H.E.S.S. telescope system

Two of the basic parameters of the H.E.S.S. instruments are the angular resolution and the sensitivity of the system. These will be summarised in the following.

### 4.5.1 Angular Resolution

The angular resolution of the H.E.S.S. system can be derived from point-source $\gamma$-ray Monte-Carlo simulations. For this purpose a distribution of squared angular distance $\theta^2$ between the true and the reconstructed direction of the Monte-Carlo $\gamma$-rays is generated and as a canonical value, the 68%-containment radius of this distribution determined.

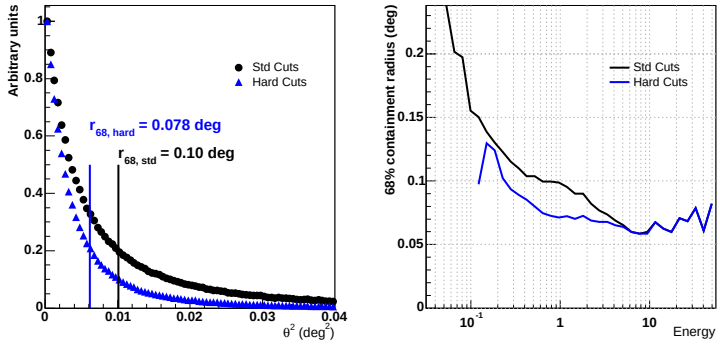


**Figure 4.24:** Angular resolution of the H.E.S.S. instrument. **Left:** Distribution of squared angular distance $\theta^2$ of reconstructed direction from the source direction for a Monte-Carlo $\gamma$-ray source for standard and hard cuts. Different camera offset and zenith angle Monte-Carlo simulations have been averaged to match the distribution of zenith angles as for one of the new source found in the survey (HESS J1813-148). This histogram defines the PSF of the H.E.S.S. instrument for this dataset. The straight lines denotes the 68% containment radius ($r_{68}$) of the PSF, which is used as a figure of merit to describe the angular resolution of the instrument. **Right:** $r_{68}$ as a function of the $\gamma$-ray energy for standard and hard cuts. The wiggles above 10 TeV arise from a lack of statistics for these high energies in the Monte-Carlo $\gamma$-rays.

Figure 4.24 (left) shows the $\theta^2$ distribution of Monte-Carlo $\gamma$-rays (point spread function). Different camera offsets and zenith angle Monte-Carlo simulations have been averaged to match the distribution for these parameters for the dataset of one of the new H.E.S.S. sources detected in the Galactic Plane survey (HESS J1813-148). The figure of merit, used to describe the angular resolution of the H.E.S.S. instrument for this dataset is the 68% containment radius of this histogram, which is commonly referred to as the Point Spread function of the instrument. Figure 4.24 (right) shows for the same zenith angle and offset the 68% containment radius as a function of the reconstructed energy for the standard and hard cuts. It can be seen, that the hard cuts provide a better angular resolution up to energies close to 10 TeV. The oscillations above 10 TeV are due to bad statistics in the Monte-Carlo $\gamma$-ray simulations above these energies.

Of great importance for the conduction of surveys making use of the large field of view of H.E.S.S. is the off-axis performance of the telescope system. Figure 4.25 (left) shows in triangles and circles the 68% containment radius of the PSF as a function of the offset from the pointing direction of the system for two different zenith angles. It can be seen, that the angular resolution is reasonably constant out to 1.5° (even to 2° for 20° zenith angle). Also shown in this figure is the efficiency for $\gamma$-ray showers relative to on-axis $\gamma$-rays. The efficiency curve is reasonably flat for the inner 1° and then falls off mostly due to the cut on the nominal distance (at 2° for this dataset). Figure 4.25 (right) shows the angular resolution as a function of the zenith angle of the observation for an offset of 0.5°. As apparent also in Figure 4.25 (left), the angular resolution is better for smaller

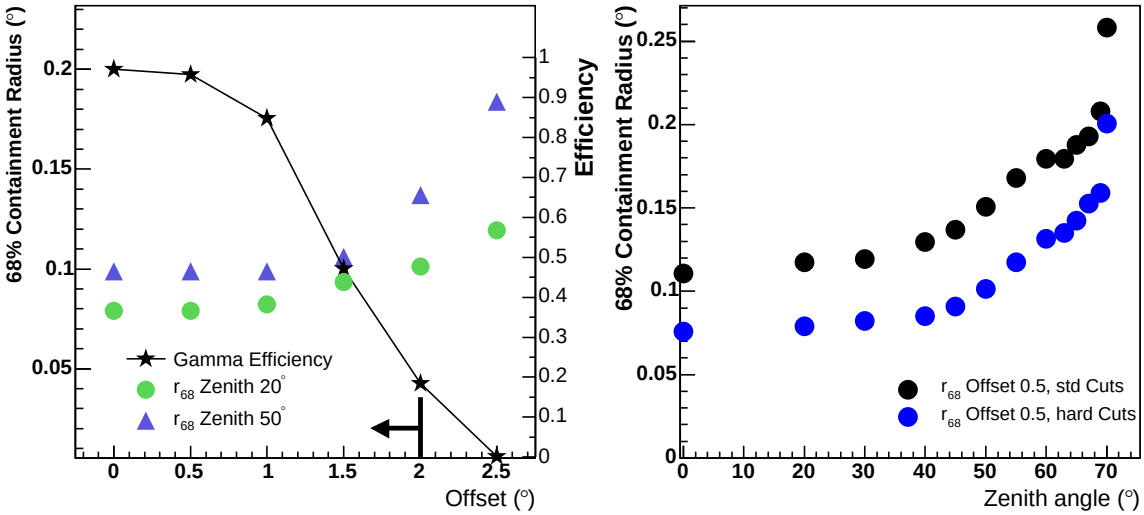


**Figure 4.25: Left:** The off-axis performance of the H.E.S.S. instrument. The black curve shows the simulated $\gamma$-ray collection efficiency relative to that for an on-axis source, assuming a source spectrum of the form $dN/dE \propto E^{-2}$ at 20° zenith angle. The green circles and blue triangles show the simulated angular resolution (68% containment radius) for hard cuts, plotted as a function of the offset for observations at zenith angles of 20° and 50° respectively. The arrow denotes the offset $\psi = 2°$ up to which events are used in the standard analysis. **Right:** Angular resolution plotted as a function of the zenith angle of the observation for hard and standard cuts and a source with an energy spectrum as in the left panel at an offset of 0.5° from the pointing direction.

zenith angles and is reasonably flat to a zenith angle of 40°. For larger zenith angles the average core distance of the shower increases rapidly, leading to a smaller average stereo angle between camera images leading to a worse reconstruction of the direction. These figures show that the angular resolution of the system in the inner part of the camera and for moderate zenith angles is well behaved.

### 4.5.2 Sensitivity

The sensitivity of an instrument indicates the minimum detectable flux of an object. The sensitivity of the H.E.S.S. instrument is an order of magnitude better than previous instruments in the range between 100 GeV and 10 TeV. Figure 4.26 (left) shows the minimum detectable flux above the energy $E$ for a 5 $\sigma$ detection in 50 hours of observation as a function of the reconstructed energy for the standard H.E.S.S. analysis using the reflected region background method as described in section 4.2.4. Each points denote an integrated sensitivity in the sense that it contains the minimum detectable flux above the energy given on the x-axis. The sensitivity value is derived for the detection above that energy of a source with the corresponding flux and a Crab-like spectrum (photon index 2.6) at the $5\sigma$ level in a 50 hour observation. As off-data for these curves, runs taken

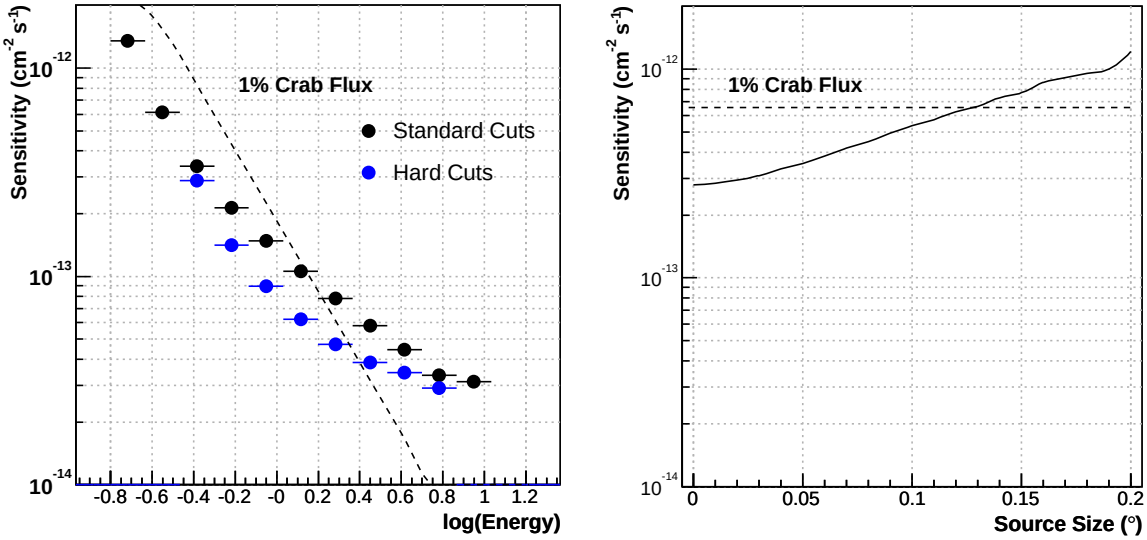


**Figure 4.26: Left:** Sensitivity curve for the H.E.S.S. telescope system for two different sets of cuts plotted against reconstructed energy. This sensitivity is derived for an observation of 50 hours at 20° zenith angle and a camera offset of 0.5° , for a source with a power-law spectrum with photon index 2.6 (as for the Crab Nebula). The sensitivity curve uses only events with energies above the spectral *safe threshold*). **Right:** For hard cuts, sensitivity plotted against angular size of the source, for the same parameters. The wiggles in the curve arise from the fact that different number of background regions are used, depending on the $\theta^2$ cut (which is adapted for the source size).

at an offset of 0.5° and in the zenith angle range between 20° and 30° on targets from which no $\gamma$-ray-emission was detected, were used. On-data were taken from Monte-Carlo $\gamma$-rays averaged over the zenith angle range. It should be noted that the sensitivities shown here apply only for events above the safe spectral threshold different for the two sets of cuts (as described in section 4.4 this is the minimum energy for which the energy bias is below 10%). This threshold is slightly higher than the *trigger threshold* (described in section 3.3), given as the peak of the differential trigger rate). The black points show the sensitivity for standard cuts, for which the spectral threshold is 200 GeV for the given zenith angle range. The blue points show the sensitivity for hard cuts with a higher threshold of 420 GeV. Also shown is the curve corresponding to 1% of the Crab flux above that energy. The curves demonstrate the increased sensitivity of the hard cuts at the expense of a higher energy threshold.
Of particular interest for the analysis of galactic sources is the dependence of the H.E.S.S. sensitivity on the source size $\sigma_{\text{source}}$. Figure 4.26 (right) shows the sensitivity for hard cuts as a function of the source size. To generate this curve, an optimum cut $\theta^2_{\text{opt}}$ was derived for a given source size by:

$$\theta^2_{\text{opt}} = \theta^2_{\text{point}}(\sigma^2_{\text{source}} + \sigma^2_{\text{PSF}})/\sigma^2_{\text{PSF}} \tag{4.21}$$

approximating the H.E.S.S. PSF as a 2-D Gaussian with $\sigma_{\rm PSF} = 0.08^\circ$ and $\theta_{\rm point} = 0.1^\circ$ (standard $\theta$ cut for hard cuts). Such a cut provides optimum significance for a weak Gaussian shaped source on a uniform background. Using the one-dimensional region background technique, the number of off-regions $n_{\rm off}$ that can be fit on the ring around the observation position depends on the $\theta^2$ cut (assuming that the camera offset is fixed to $0.5^\circ$). The background level $B_{{\rm tot},\sigma}$ in the $n_{\rm off}(\sigma)$ off-regions used for a given $\theta^2$ cut can be estimated from the total number of background events for a point-source analysis $B_{\rm point}$ by

$$B_\sigma = \frac{N_\sigma \theta^2_{\rm opt}}{N_{\rm point}\theta^2_{\rm point}} B_{\rm point} \tag{4.22}$$

This is a valid approach as long as the background regions are small in comparison to the camera field of view, so that the decrease in acceptance within the off-regions is small. As can be seen, for a source of RMS source size $0.2^\circ$ the sensitivity decreases a factor of $\sim 4$ with respect to the point-source sensitivity.

## 4.6 Some aspects of Data Quality

Due to the large number of subsystems of the H.E.S.S. array a wealth of information about the status of the system is available. In the following, some key parameters concerning the performance of the system are summarised.

### 4.6.1 Telescope Efficiency

To achieve optimal energy resolution for a Cherenkov telescope system, the relative response of the telescopes, i.e. the relation between the light yield and the digital counts provided by the ADC system must be known with very good precision. While single telescopes are flat-fielded using the pulsed light emitting laser in the centre of the dish, the telescope-to-telescope calibration is more complicated. In the following, a simple technique for telescope intercalibration according to Hofmann (2003) is presented.
After the flat-fielding of the individual telescopes, one calibration factor per telescope is required to relate the image size to the photon yield. Two telescopes can be compared by selecting showers with cores equidistance from the two telescopes, and comparing the image sizes of both telescopes. However, in systems with more than two telescopes, one needs to be careful not to introduce a bias due to other telescopes involved in the triggering or the event reconstruction. Several steps should be taken in order to ensure an unbiased comparison:

1. To compare two telescopes, events were selected where both telescopes had triggered (and possible others in addition). Only information from the two telescopes was used in the shower reconstruction. The images from other telescopes were ignored.

2. To reduce the influence of trigger thresholds, a cut above the threshold was applied; the sum of the image sizes of the two telescopes had to be above 200 photoelectrons.

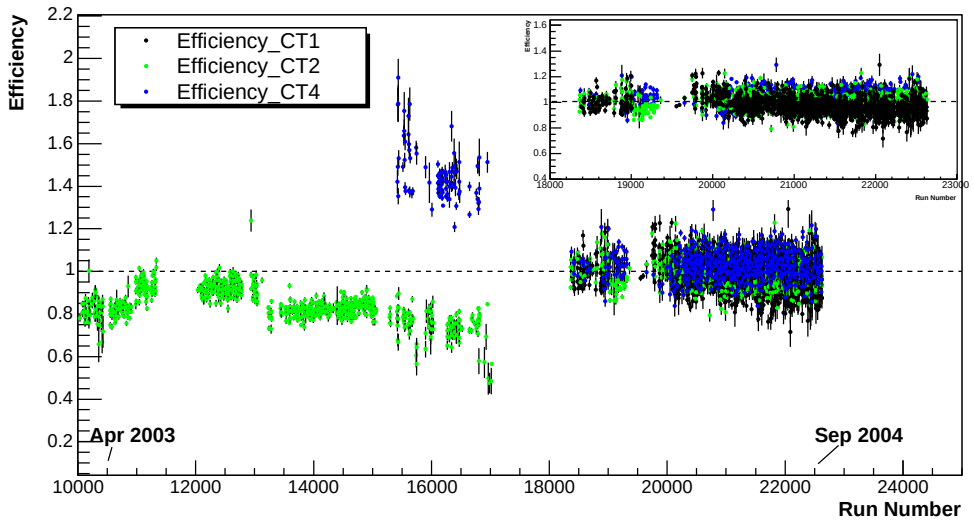


**Figure 4.27:** Telescope efficiencies relative to CT3 according to Equation 4.23, derived from the image size asymmetry for images with a shower core equidistant to the two telescopes under consideration. The time range for the runs shown here corresponds to April 2003 (run 10000) to September 2004 (run 22500).

3. Additional "quality cuts" were applied to improve image quality and reconstruction. These included a cut on the nominal distance of 1.75°, a cut on the (stereo) angle between the two image axis of a least 30° and finally a cut on the reconstructed shower direction to be within 0.7° from the telescope axis.

The relative response of two telescopes $i$ and $j$ can then be derived from plotting the size asymmetry $a_s$ as a function of the impact distance asymmetry $a_r$. These asymmetries are given by $a_{s(i,j)} = \frac{s_i - s_j}{s_i + s_j}$ and $a_{r(i,j)} = \frac{r_i - r_j}{r_i + r_j}$, with $s_i$ being the image size and $r_i$ the impact distance for telescope $i$. For the determination of the relative telescope response for the telescopes $i$ and $j$, the average $a_s$ for $a_r = 0$ has to be determined. This is achieved by cutting on $a_r < 0.05$ and fitting a Gaussian to the resulting distribution of $a_s$. By defining the efficiency of telescope $i$ relative to telescope $j$ as

$$\mathrm{Eff(i,j)} = \frac{1 + < a_{s(i,j)} >}{1 - < a_{s(i,j)} >}, \tag{4.23}$$

where $< a_{s(i,j)} >$ is the mean of the fitted Gaussian, one can derive relative telescope responses. Figure 4.27 shows the efficiencies of CT1, CT2 and CT4 relative to CT3 (Eff(i, 3)).
As can be seen from Figure 4.27, after run 18000, which was the time, when the fourth telescope (CT1) was added to the system and all PMTs exchanged between the cameras in order to achieve a maximum agreement in the response of the cameras, the system behaves well balanced and the efficiencies are within 20% of the efficiency of CT3. Note that the Galactic Plane survey data that will be presented in the following chapter corresponds to runs numbers above 20000.

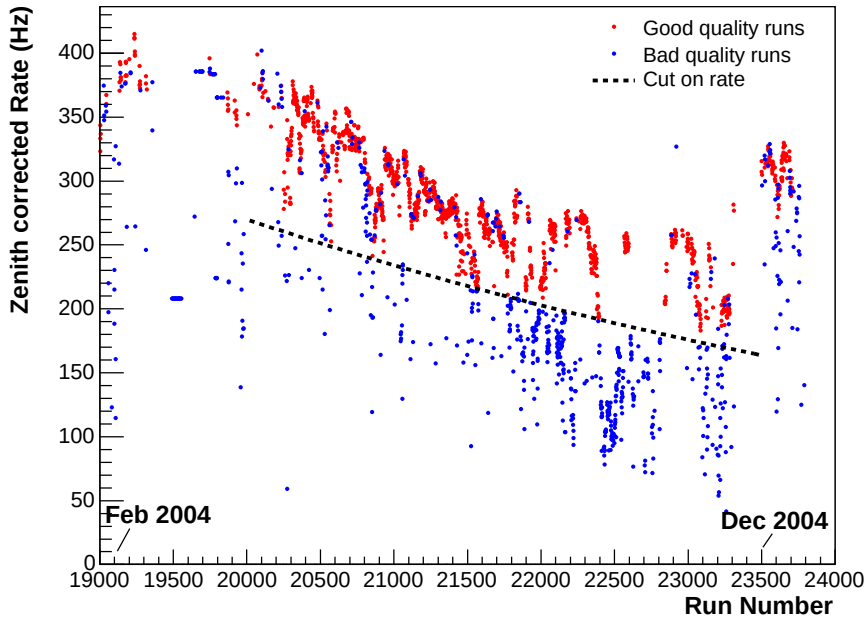


**Figure 4.28:** Time evolution of the system trigger rate for observation runs with 4 participating telescopes. Shown in red are the runs passing all run selection cuts on hardware and zenith corrected trigger rate, in blue all runs that don't pass the run selection cuts are shown. The dashed line shows the cut on the zenith corrected rate. An overall degradation is apparent as discussed in the text. Also seen is the effect of the adjustment of the high voltage of the PMTs that was performed close to run 23500. The time range for this histogram is from February 2004 (run 19000) to December 2004 (run 23500).

### 4.6.2 Evolution of the System Trigger Rate

Another important parameter of H.E.S.S. is the system trigger rate. It is used for example in the selection of good quality runs and should be stable over time. The system trigger rate evolution is correlated to the efficiency evolution of the system if all threshold parameters of the camera and the central trigger system are kept constant.
An overall reduction of the system trigger rate is apparent from Figure 4.28. Unknown quantities that change with time and play a role in the overall efficiency of the system and hence affect the system trigger rate are: mirror efficiency, quantum efficiency of the PM tubes, reflectivity of the Winston cones, etc. The envelope of this curve shows an overall degradation of the system rate up to run $\sim$ 23500. At this time the high voltage of the PMTs were readjusted to provide a nominal gain of 80 ADC counts/pe. This can by seen in the system trigger rate as a step after that run number. It seems clear from this, that at least some of the degradation of the system rate was due to the loss of gain of the PM tubes that could be partially corrected by an increase of the high voltage.
As a conclusion from the system rate evolution it seems that there is some degradation of the system, but it can be partially recovered by increase of the high voltage.

# Chapter 5

# The H.E.S.S. Galactic Plane survey

## 5.1 Basic properties of the H.E.S.S. Galactic Plane survey

The H.E.S.S. survey of the central region of our Galaxy took place between May and July 2004 at an average flux sensitivity around 3% of the Crab flux. The survey was conducted in the Galactic longitude band $\pm 30^\circ$ around $l = 0^\circ$. Runs of 28 minutes duration were taken at pointing positions with a spacing of $0.7^\circ$ in longitude in three strips in Galactic latitude: $b = -1^\circ, b = 0 \circ$ and $b = +1^\circ$. Runs were selected based on weather and hardware conditions. 95 hours of quality-selected data were taken in this survey mode. The observation schedule was optimised so that individual pointings were conducted near culmination, resulting in the smallest zenith angles accessible. Figure 5.1 (left) shows the resulting not very strong correlation of Galactic longitude and zenith angle, showing that the Galactic Plane can be observed under good observation conditions. The large zenith angle observations present in Figure 5.1 (left) were taken in reobservation of promising source candidates July and October 2004. These reobservations yielded a further 30 good-quality hours of data. For the analysis described in the following, additional pointed observations of SNR RX J1713.7–3946 and of the Galactic Centre region (also partially at large zenith angles) are included. The total data set presented here amounts to 230 hours after quality selection, the mean zenith angle of all observations is $26^\circ$. Figure 5.2 shows a map of exposure for this data set, expressed in terms of an equivalent number of hours observing a source at the centre of the field of view.

As can be seen from Figure 5.2, the exposure is rather irregular with peak exposures in the regions around RX J1713.7–3946 and the Galactic Centre. This irregular exposure results in an uneven sensitivity for the detection of new sources. The sensitivity of the survey in Galactic latitude (averaged over the whole longitude range in black and for a region in longitude in which no re-observations took place in blue) is shown in Figure 5.1 (right). For $-1.5^\circ < b < 1.5^\circ$ the sensitivity is rather flat at a level of 2.5% of the flux from the Crab Nebula, and deteriorates rapidly at $> 2^\circ$ from the Galactic Plane.

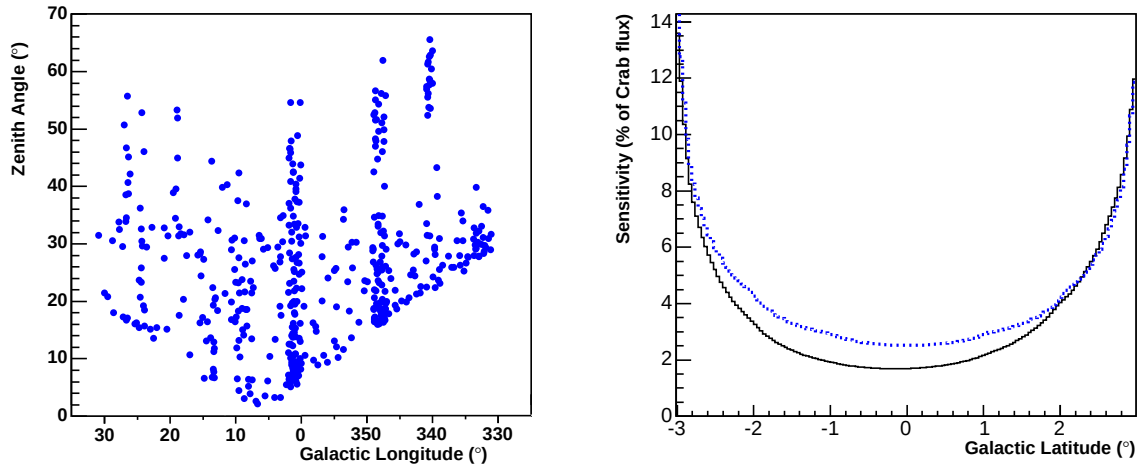


**Figure 5.1: Left:** Correlation between Galactic longitude and zenith angle of observation of the individual runs, analysed in this work. Each point corresponds to one run of 28 generally 28 minutes of observation. The large zenith angle observations were taken in pointed reobservations on source candidates and in pointed observations on the previously known source RX J1713.7-3946 and at the Galactic Centre that are included in the dataset used here. **Right:** Sensitivity in Galactic latitude of the H.E.S.S. Galactic Plane scan in units of the flux from the Crab Nebula ($\sim 3 \times 10^{-10}$ cm$^{-2}$ s$^{-1}$, $E > 200$ GeV) and assuming a power-law spectrum with photon index 2.6. The sensitivity used here is defined as the minimum flux of a source that would be detectable in this survey by H.E.S.S. at the 5 $\sigma$ level. The solid curve shows the sensitivity averaged over the whole longitude range of the survey. The blue dashed curve shows the sensitivity in the range of longitude $350^\circ < l < 357^\circ$, a region where no re-observations were conducted. This sensitivity is calculated before accounting for the number of trials.

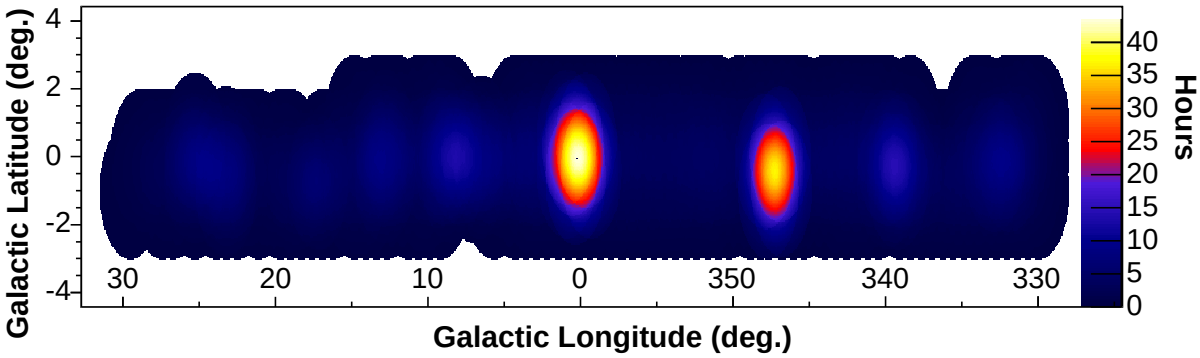


**Figure 5.2:** The effective exposure of the H.E.S.S. Galactic Plane survey, expressed as equivalent number of hours spent observing a source at the centre of the field of view. The deeper observations of the RX J1713.7–3946 and the Galactic Centre are apparent.

## 5.2 Analysis of the survey data

The H.E.S.S. Galactic Plane survey yielded a large amount of data. In 230 hours 522635 $\gamma$-ray like events were collected and are available for the analysis. For this purpose an analysis chain was developed that yielded fast results as will be described in the following. The analysis chain was prepared by separately looping over individual runs and filling two histograms:

- a raw sky map centred on the observation position of the run, containing all events that pass the event selection cuts (apart from the $\Theta^2$ cut) out to a distance of $\psi = 4°$ from the observation position. This map contains all $\gamma$-ray like events to be used in the following analysis.

- an acceptance map centred on the observation position of the run. The acceptance map is generated either by a rotation of the run-wise acceptance curve or the acceptance curve model taking into account the zenith angle distribution of the events in the run.

These two maps are generated once for each run as a pre-analysis step. After this the event-by-event information is lost, since the analysis of the survey data acted only on these histograms. Therefore in a separate step a detailed analysis of the $\gamma$-ray source candidates found in the survey analysis has to be performed in order to generate e.g. an energy spectrum as will be described in section 5.3.2.
In the analysis of the scan data, all runs within the scan region are analysed by adding up the individual run-wise histograms (the raw sky map and the acceptance map) into a big histogram encompassing the whole range of the survey in Galactic longitude and latitude. In the summation of the histograms, a cut on $\psi$ (the distance of the event from the pointing position of the system) of typically 2° is used to avoid systematic effects of the acceptance curve at large distances from the camera centre due to small statistics. This cut reduced the number of available $\gamma$-ray events to 421100. The summation of the histograms resulted in one large raw sky map and one large acceptance map, containing all individual run-wise histograms. By using these histograms, the survey region was divided (a priori) into a grid of trial source positions with grid points of width 0.04°, a value well below the angular resolution of the instrument.
The background for each grid point was estimated using two different techniques as described in section 4.2. For the ring background estimation a ring around each grid point with a mean radius of 0.7° and an area 7 times that of the on-region was used to estimate the background level. The standard ring radius of 0.5° was increased to 0.7° (again a priori) to improve sensitivity to extended sources. The template method uses the standard H.E.S.S. parameters and estimates the background level from events with a MSCW value between 2.0 and 7.0. Figure 5.3 shows the correlation of the background level estimated for each grid point from the ring background and the template background method. The slope of the major axis of the distribution is 1.01 and the dispersion in the distribution is consistent with it being dominated by statistical fluctuations in the number of counts for the two statistically independent background estimates. This shows that the background estimates are consistent within 1%.

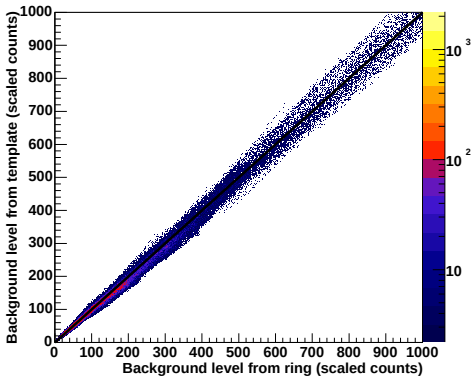


**Figure 5.3:** Background level estimated for each grid point (given by $\alpha \times N_{\mathrm{off}}$), calculated using a ring background technique, plotted as a function of the background level estimated from a template method (Rowell, 2003). The dashed line shows the expected one-to-one correlation. The width of distribution is consistent with expectations for statistical fluctuations in the independent background estimates.

For each grid point in the scan region, the on-source signal was calculated by summation of all events within a circle of radius $\theta = 0.22°$, (or $\theta^2 = 0.05(°)^2$), a cut appropriate for slightly extended sources with respect to the angular resolution of the instrument. This cut was chosen a-priori and is optimal for the detection of $\gamma$-ray sources with the average size of Galactic SNRs (Green, 2004).
From the on-counts and the background level for each grid point in the map a statistical significance can be determined, testing the existence of a $\gamma$-ray source at the position of that grid point, resulting in a significance map.

### 5.2.1 Trial factor

Since the significance map contains a large number of test positions ($\sim$ 250000), this significance has to be corrected by a "trial factor" $N_{\mathrm{trial}}$. The trial factor accounts for the increased probability of finding a fake signal with an increased number of test positions for which a significance is calculated. If the grid points were uncorrelated, the trial factor would be exactly equal to the number of grid points. Since the significances are correlated by the on-region (through the summation within the $\theta^2$ circle) as well as by the background determination (through the summation within the ring) as shown in Figure 5.4 (left), it is not possible to analytically derive the correct trial factor. However it is evident, that the trial factor must be between the most optimistic estimate in which it is calculated how many times the $\theta^2$ circle fits into the survey region (2400) and the most conservative estimation, the numbers of trial positions (250000). A Monte-Carlo simulation of the technique applied to the survey data has been performed to estimate the trial factor. No sources of $\gamma$-rays were simulated in this Monte-Carlo approach, but instead the raw sky map was replaced by one sampled from the acceptance curve with the same number of events as the original map. The acceptance map was used from the

data and the individual raw sky and acceptance maps were added up as described in the previous section. Then a significance map was generated similar to the approach in real data. This procedure was repeated 3000 times and the resulting significance distributions of the individual Monte-Carlo simulations were added up. This trial factor can then be determined from the number of sources above a certain significance in comparison to the number one would expect for 3000 Monte-Carlo simulation each with a trial factor $N_{\mathrm{trial}}$. The trial factor was found to be a factor of $\sim 2$ lower than the number of points for which a significance is calculated, i.e. the number of grid points in the map. For the calculation of post-trials significances it was conservatively assumed that the number of trials is equal to the number of bins. Figure 5.4 (right) shows the distribution of significances for all grid points in the map (solid black). This distribution is consistent with a normalised Gaussian, demonstrating that the analysis technique behaves as expected.

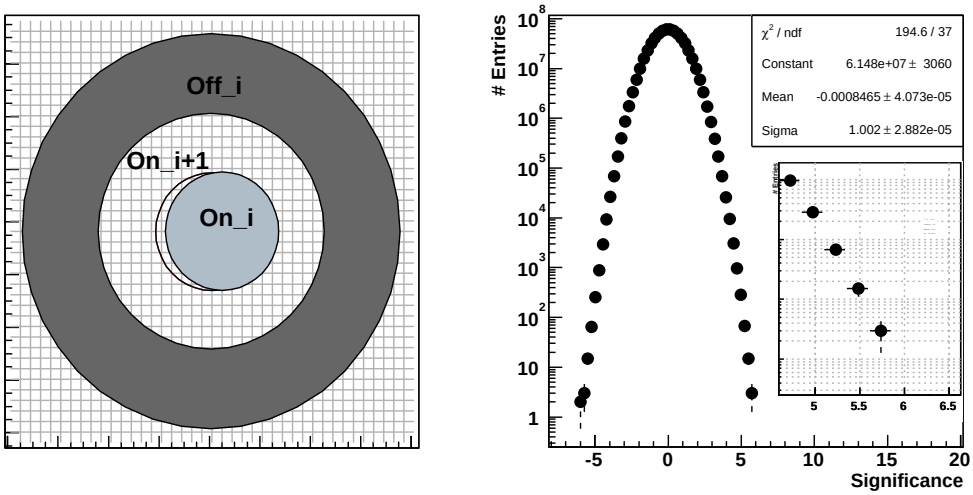


**Figure 5.4: Left:** Schematic description of the correlation between adjacent grid points. The grey boxes show the grid positions, the two circles show two adjacent on-regions and the big ring shows the background region for one of the on-regions. It becomes clear, that the significances calculated for neighbouring grid positions are highly correlated. **Right:** Distribution of significances for the 3000 Monte-Carlo simulation of the survey without $\gamma$-ray sources, along with a Gaussian fit. The inset shows the same distribution, zoomed in the range of 4.8 to 6.5 standard deviations.

### 5.2.2 Significance Map

The resulting significance map with the background estimated from the ring technique is shown in Figure 5.5. It should be noted that the values $S_1$ in this map are significances before accounting for the trial factor and will have to be corrected in the following. The strong $\gamma$-ray sources RX J1713.7–3946, HESS J1745–290 clearly stand out, partly because of the high exposure in this regions. Also visible at a much fainter level is the recently published new $\gamma$-ray source G 0.9+0.1 (Aharonian et al., 2005d), which was serendipitously

detected in the H.E.S.S. observations of the Galactic Centre region. The significance map has been searched for further candidate sources of $\gamma$-rays by requiring a minimum significance of 6.2 $\sigma$, corresponding to $4\sigma$ after accounting for all trials. In addition to the three known objects, fourteen new sources of VHE $\gamma$-rays are detected above the required level, the eight most significant of which have been discussed in Aharonian et al. (2005b). The new sources are marked in Figure 5.5 with arrows and have the post-trial significance given next to their position. A search for very extended sources with respect to the angular resolution using a larger $\theta^2$ cut yields similar results. With one exception, a similar search for point-like sources with a $\theta^2 = 0.01(^\circ)^2$ cut revealed only a subset of the sources presented here. The exception is the H.E.S.S. source HESS J1826–146 coincident with the microquasar LS5039. The significance map for the point-like and for the extended $\theta^2$ cut are given in Appendix A.
A post-trial significance $S_2$ (the effective *detection significance*) was calculated from the pre-trials significance $S_1$ by converting $S_1$ into a probability, recalculating the probability of the occurrence of one or more such events given the number of trials and converting this probability back into a significance. Grid Points for which the post-trial significance is above $4.0\sigma$ (corresponding to $6.2\sigma$ before trials) are considered as likely sources of VHE $\gamma$-rays. The probability of a single fake signal at this level is $3 \times 10^{-5}$ in the whole survey. Table 5.1 shows the pre-trials significance for the peak positions in the map for the new sources in column $S_1$ and the significance after accounting for the number of trials in column $S_2$. Column $S_3$ shows the post-trial significance applying a cut appropriate for point source ($\theta_{\rm point} = 0.1^\circ$) instead of the extended source cut $\theta = 0.22^\circ$.

## 5.3 Characteristics of the new sources

A detailed spectral and positional analysis has been performed on the 14 sources listed in Table 5.1.

### 5.3.1 Position and Morphology

For the position and approximate size determination of each source, the spatial distribution of excess events was fit to a model of a 2-D Gaussian $\gamma$-ray brightness profile of the form $\rho \propto \exp(-\theta^2/2\sigma^2_{\rm source})$, convolved with the PSF of the instrument as described in section 4.3. To test for possible elongation of each emission region, an elongated Gaussian with independent $\sigma_{\rm source}$ and $\sigma'_{\rm source}$ in each dimension and a free orientation $\omega$ was also fit. As criterion for significant elongation, the error range of the minor axis $\sigma'_{\rm source}$ being outside that of the major axis $\sigma_{\rm source}$ was requested. Using the best fit position and a reduced bin size to allow for a more accurate sampling of the peak, the significance of the candidate source has was re-determined, using the ring background method. Column $S_4$ of Table 5.1 shows the post-trial significance for the best fit position for the detailed analysis using a $\theta = 0.22^\circ$ cut. Table 5.2 shows the best fit position and best fit Gaussian equivalent size $\sigma_{\rm source}$ (and $\sigma'_{\rm source}$ and orientation $\omega$ in case of elongation) of the seventeen

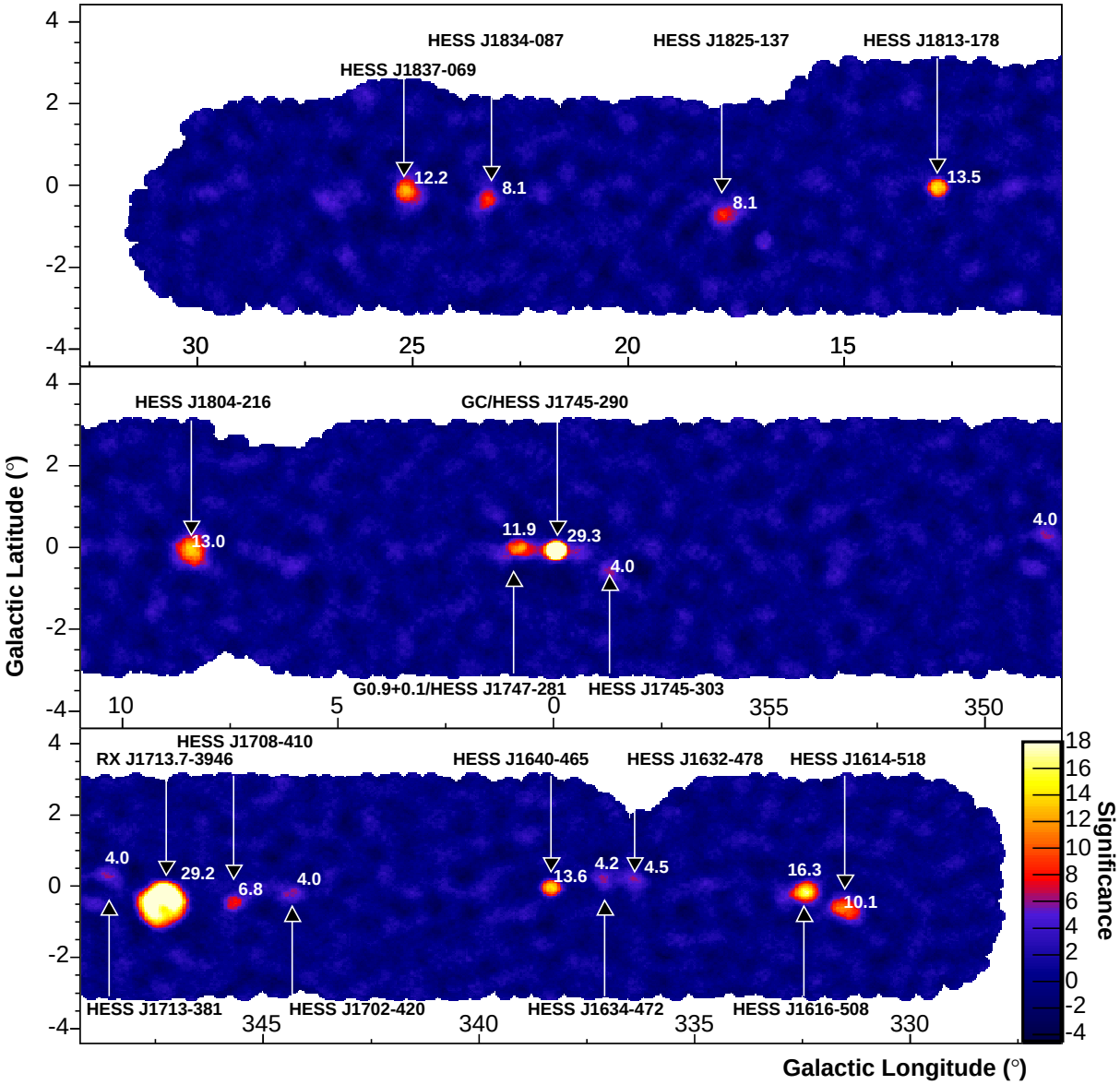


**Figure 5.5:** Significance map of the H.E.S.S. Galactic Plane survey in 2004, including re-observations of source candidates detected in the original scan and observations of the known $\gamma$-ray emitter RX J1713.7–3946 and the Galactic Centre region. The energy threshold for this map is 250 GeV. The on-source counts for each grid point are integrated in a circle of radius $\theta = 0.22°$. The background for each grid point has been derived using a ring of mean radius 0.7° and an area 7 times that of the on-source circle. The labels indicate the $\gamma$-ray sources described in this work, along with the known $\gamma$-ray sources RX J1713.7–3946, G 0.9+0.1 and the Galactic Centre. The numbers in the map give the post-trials significances of the $\gamma$-ray sources. The significance scale is truncated at $18\sigma$, the signals from the Galactic Centre and RX J1713,7–3946 exceed this level.

**Table 5.1:** Table of significances for the new sources of VHE $\gamma$-rays detected in the survey of the Galactic Plane. $S_1$ stands for the pre-trials significance (using a $\theta^2$ cut of $0.05^\circ$) for the peak positions in the map. $S_2$ shows the post-trial significance for this position. Column $S_3$ shows the post-trial significance for this position for a point-source cut ($\theta_{\rm point} = 0.1^\circ$). $S_4$ shows the post-trial significance similarly to $S_2$ for a $\theta^2$ cut of $0.05^\circ$ for the the best fit position of the finely binned detailed analysis. The sources that are marked with a † have been reported in (Aharonian et al., 2005b). Galactic longitude $l$ and latitude $b$ as well as RA/Dec coordinates are given in degrees, the live time is given in hours. HESS J1826–146 is detected significantly only in the point-like search (see Appendix A) and is included here and in the following for completeness.

| Name | Position | | | | Significance | | | | Live time |
|---|---|---|---|---|---|---|---|---|---|
| | $l$ | $b$ | RA | Dec | $S_1$ | $S_2$ | $S_3$ | $S_4$ | |
| J1614–518† | 331.52 | –0.58 | 243.58 | –51.82 | 11.6 | 10.5 | 7.5 | 11.1 | 9.8 |
| J1616–508† | 332.39 | –0.14 | 244.10 | –50.90 | 17.4 | 16.7 | 9.7 | 16.6 | 10.2 |
| J1632–478 | 336.38 | 0.19 | 248.04 | –47.82 | 6.6 | 4.5 | - | 5.6 | 4.5 |
| J1634–472 | 337.11 | 0.22 | 248.74 | –47.27 | 6.4 | 4.2 | 1.8 | 4.2 | 6.6 |
| J1640–465† | 338.32 | –0.02 | 250.18 | –46.53 | 14.5 | 13.6 | 14.5 | 12.0 | 14.3 |
| J1702–420 | 344.26 | –0.22 | 255.69 | –42.07 | 6.3 | 4.0 | 4.1 | 3.6 | 5.7 |
| J1708–410 | 345.67 | –0.44 | 257.06 | –41.08 | 8.4 | 6.8 | 6.9 | 7.3 | 37.4 |
| J1713–381 | 348.65 | 0.38 | 258.49 | –38.20 | 6.3 | 4.0 | 1.4 | 2.9 | 37.3 |
| J1745–303 | 358.71 | –0.64 | 266.26 | –30.37 | 6.3 | 4.0 | 1.8 | 3.1 | 35.3 |
| J1745–290 | 359.95 | –0.05 | 266.42 | –29.00 | 29.8 | 29.3 | 33.9 | 34.6 | 49.3 |
| J1747–281 | 0.87 | 0.08 | 266.85 | –28.15 | 12.9 | 11.9 | 11.2 | 8.3 | 49.3 |
| J1804–216† | 8.40 | –0.03 | 271.13 | –21.70 | 13.9 | 13.0 | 7.7 | 15.9 | 15.7 |
| J1813–178† | 12.81 | –0.03 | 273.40 | –17.84 | 14.4 | 13.5 | 15.3 | 13.2 | 9.7 |
| J1825–137† | 17.82 | –0.74 | 276.51 | –13.76 | 9.5 | 8.1 | 3.7 | 8.7 | 8.4 |
| J1826–146 | 16.89 | –1.31 | 276.58 | –14.85 | 3.84 | - | 7.04 | - | |
| J1834–087† | 23.24 | –0.32 | 278.69 | –8.76 | 9.5 | 8.1 | 5.7 | 7.0 | 7.3 |
| J1837–069† | 25.18 | –0.11 | 279.41 | –6.95 | 13.2 | 12.2 | 9.9 | 13.9 | 7.6 |

**Table 5.2:** Position and sizes of the new sources of VHE $\gamma$-rays detected in the survey of the Galactic Plane. Galactic longitude $l$ and latitude $b$, the RMS source size $\sigma_{\text{source}}$ and $\sigma'_{\text{source}}$ and the orientation angle $\omega$ counter-clockwise with respect to the Galactic latitude axis are given in degrees.

| Name | Source Position | | $\sigma_{\text{source}}$ | $\sigma'_{\text{source}}$ | $\omega$ |
|---|---|---|---|---|---|
| | l | b | | | |
| J1614–518 | 331.52 ± 0.03 | –0.58 ± 0.02 | 0.23 ± 0.02 | 0.15 ± 0.02 | 49 ± 10 |
| J1616–508 | 332.391 ± 0.014 | –0.138 ± 0.013 | 0.136 ±0.008 | - | - |
| J1632–478 | 336.38 ± 0.04 | 0.19 ± 0.03 | 0.21 ± 0.05 | 0.06 ± 0.04 | 21 ± 13 |
| J1634–472 | 337.11 ± 0.05 | 0.22 ± 0.04 | 0.11 ± 0.03 | - | - |
| J1640–465 | 338.316 ± 0.007 | –0.021 ± 0.007 | 0.045 ±0.009 | - | - |
| J1702–420 | 344.26 ± 0.04 | –0.22 ± 0.03 | 0.08 ± 0.04 | - | - |
| J1708–410 | 345.672 ± 0.013 | –0.438 ± 0.010 | 0.054 ±0.012 | - | - |
| J1713–381 | 348.65 ± 0.03 | 0.38 ± 0.03 | 0.06 ± 0.04 | - | - |
| J1745–303 | 358.71 ± 0.04 | –0.64 ± 0.05 | 0.21 ± 0.06 | 0.09 ± 0.04 | 54 ± 7 |
| J1745–290 | 359.949 ± 0.002 | –0.046 ± 0.002 | 0.0297 ± 0.006 | - | - |
| J1747–281 | 0.872 ± 0.005 | 0.076 ± 0.005 | 0.0 ± 0.01 | - | - |
| J1804–216 | 8.401 ± 0.016 | –0.033 ± 0.018 | 0.200 ±0.010 | - | - |
| J1813–178 | 12.813 ± 0.005 | –0.0342 ± 0.005 | 0.036 ±0.006 | - | - |
| J1825–137 | 17.82 ± 0.03 | –0.74 ± 0.03 | 0.16 ± 0.02 | - | - |
| J1826–146 | 16.89 ± 0.01 | –1.31 ± 0.01 | 0.02 ± 0.03 | - | - |
| J1834–087 | 23.24 ± 0.02 | –0.32 ± 0.02 | 0.09 ± 0.02 | - | - |
| J1837–069 | 25.185 ± 0.012 | –0.106 ± 0.016 | 0.12 ± 0.02 | 0.05 ± 0.02 | 149 ± 10 |

sources.

Figure 5.6 shows the distribution of sizes for the new sources. For the elongated sources, the arithmetic mean of $\sigma_{\text{source}}$ and $\sigma'_{\text{source}}$ was used. All but four of the sources appear significantly extended. Four out of seventeen appear significantly elongated, whereas the remaining thirteen new sources are compatible with a radially symmetric Gaussian shape. The radial excess distributions of all sources are given individually in section 5.4.

### 5.3.2 Spectra

Using the best fit position a spectral analysis was performed, again assuming a Gaussian emission region and using an optimal $\theta^2$ cut as described in equation 4.21. For the elongated sources, the arithmetic mean of $\sigma_{\text{source}}$ and $\sigma'_{\text{source}}$ was used. The energy dependent efficiency of the $\theta$ cut is estimated by convolving the H.E.S.S. PSF with a Gaussian of size $\sigma_{\text{source}}$. This introduces an additional systematic error in the absolute flux determination since it implicitly assumes that the tails of the source follow a Gaussian distribution and that the morphology of the source does not show any energy dependency. The resulting typical overall systematic error in the determination of the flux level is estimated to be

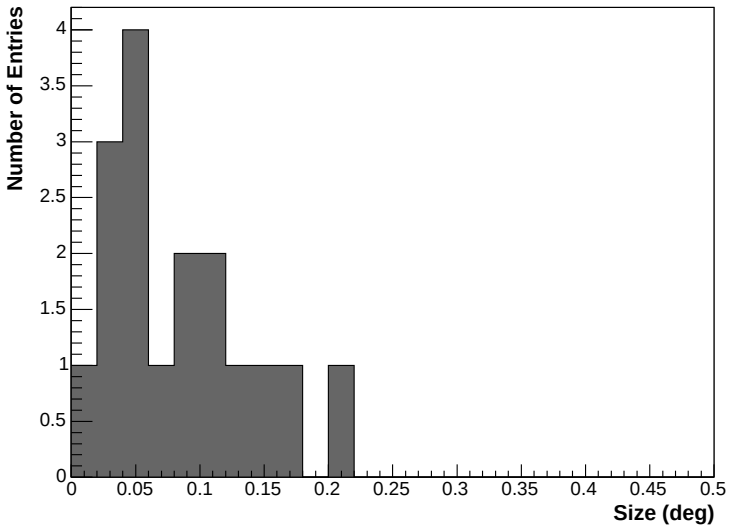


**Figure 5.6:** Distribution of the RMS angular size $\sigma_{\rm source}$ of the seventeen VHE $\gamma$-ray sources. For the elongated sources, the arithmetic mean of $\sigma_{\rm source}$ and $\sigma'_{\rm source}$ is used. The mean of this distribution is 0.08 with an RMS of 0.05.

$\sim$ 30%. The standard H.E.S.S. spectral analysis technique is described in (Aharonian et al., 2005e).
To keep as many low-energy $\gamma$-rays as possible, a looser size cut of 80 photo-electrons is used for the spectral analysis. This cut allows to reach a lower energy threshold ($\sim$ 200 GeV) at the expense of reduced sensitivity for hard spectrum sources and 30% poorer angular resolution. The consistency of the spectra derived for the size cut of 80 p.e. and the size cut of 200 p.e. has been confirmed for all sources given here. Table 5.3 lists the resulting photon index ($\Gamma$) and flux above 200 GeV for a power law fit $dN/dE = F_0 E^{-\Gamma}$. The typical systematic error on these photon indices is estimated to be $\sim$ 0.2.
Figure 5.7 shows the distribution of photon indices for the 14 new sources. The distribution exhibits a mean of 2.33, broadly consistent with predictions by models of shock wave acceleration in SNRs (Drury, Aharonian, & Völk, 1994) and expected for the spectrum of sources of Galactic cosmic rays. The distribution has an RMS of 0.19, comparable with the statistical errors on the measurements.

## 5.4 Individual $\gamma$-ray sources

This section describes the 14 VHE $\gamma$-ray sources detected in the Galactic Plane survey individually along with a brief description of possible counterparts at other wavelengths. Excess maps are shown that have been smoothed with a two-dimensional Gaussian to reduce the effect of statistical fluctuations. The resulting count map is in units of integrated excess counts within the smoothing radius. The RMS of the Gaussian used for the smoothing is adapted for each source according to the available photon statistics. This

**Table 5.3:** Results of a power-law fit $dN/dE = F_0 E^{-\Gamma}$ for the seventeen sources of VHE $\gamma$-rays. The $\theta$ cut used for the spectral analysis is given in degrees. The errors given on the spectral index and flux are statistical only. The typical systematic errors are $\sim 0.2$ in the spectral index and $\sim 30\%$ in the absolute flux.

| Name | $\Gamma$ | Flux $> 200$ GeV ($10^{-12}$ cm$^{-2}$ s$^{-1}$) | $\theta$ cut | $\chi^2$/NDF |
|---|---|---|---|---|
| HESS J1614–518 | 2.46±0.20 | 57.8±7.7 | 0.40 | 0.6/3 |
| HESS J1616–508 | 2.35±0.06 | 43.3±2.0 | 0.26 | 5.5/5 |
| HESS J1632–478 | 2.49±0.19 | 50.2±6.5 | 0.36 | 5.2/3 |
| HESS J1634–472 | 2.30±0.16 | 19.3±2.4 | 0.23 | 4.12/3 |
| HESS J1640–465 | 2.42±0.15 | 20.9±2.2 | 0.16 | 3.7/4 |
| HESS J1702–420 | 2.31±0.15 | 15.9±1.8 | 0.19 | 7,8/6 |
| HESS J1708–410 | 2.34±0.11 | 8.8±0.7 | 0.17 | 6.3/3 |
| HESS J1713–381 | 2.27±0.48 | 4.2±1.5 | 0.14 | 1.8/2 |
| HESS J1745–290 | 2.33±0.04 | 15.1±0.4 | 0.01 | 17.2/2 |
| HESS J1747–281 | 2.46±0.13 | 4.4±0.4 | 0.01 | 8.0/6 |
| HESS J1745–303 | 1.82±0.29 | 11.2±4.0 | 0.36 | 4.4/3 |
| HESS J1804–216 | 2.72±0.06 | 53.2±2.0 | 0.36 | 6.9/11 |
| HESS J1813–178 | 2.09±0.08 | 14.2±1.1 | 0.15 | 5.5/11 |
| HESS J1825–137 | 2.46±0.08 | 39.4±2.2 | 0.30 | 6.2/8 |
| HESS J1826–146 | 2.12±0.15 | 6.0±0.9 | 0.01 | 8.7/4 |
| HESS J1834–087 | 2.45±0.16 | 18.7±2.0 | 0.20 | 3.5/4 |
| HESS J1837–069 | 2.27±0.06 | 30.4±1.6 | 0.23 | 12.55/10 |

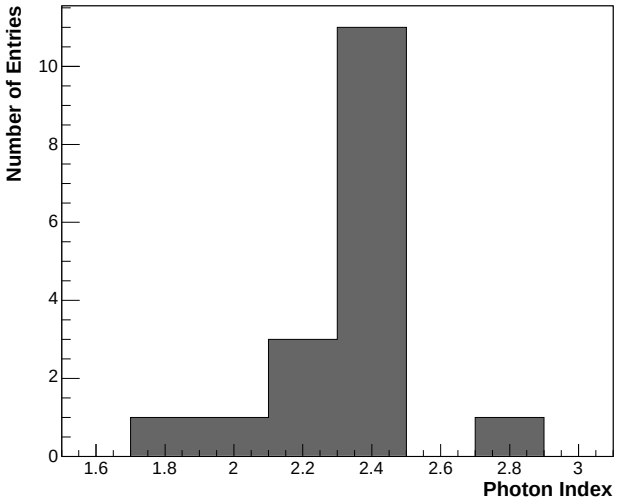


**Figure 5.7:** Distributions of the photon index of the new sources. The mean photon index is 2.33 with an RMS of 0.19.

RMS is shown as a black dotted line in the inset in the lower right part of each excess map along with the PSF of the instrument, smoothed in the same way as the excess map. Please note that the maps might have different zoom levels, therefore the white line in the upper right corner indicates a line of length 0.2°. Further it should be noted that the z-axis (that is the colour scale) has different scales for different maps. Also shown are possible counterparts to the VHE $\gamma$-ray emission: SNR from Green (2004) (with white circles illustrating their nominal radii), pulsars from the ATNF pulsar catalogue (Manchester et al., 2005) (as white triangles), hard X-ray sources detected by the International Gamma-Ray Laboratory (INTEGRAL) satellite (as white stars), and unidentified EGRET sources from the third EGRET catalogue (Hartman et al., 1999) (showing the 95% error contour for the position of the source in dashed white). In some maps contours of radio and/or X-ray emission are also shown and discussed individually. The best fit source position is shown with error bars in black, the best fit source morphology is shown as a black dashed circle or ellipse. The radial distribution of $\gamma$-ray excess with respect to the best-fit source position is shown for each source; in each plot the number of reconstructed events in bins of the squared angular distance ($\theta^2$) is shown along with the best-fit radially symmetric model (solid black line) and the PSF of the instrument (dashed red line), derived from Monte-Carlo simulations. For all sources the reconstructed differential energy spectra are shown together with the best-fit power-law (solid line).

### 5.4.1 HESS J1614–518

This source (see Figure 5.8) is located in a region relatively devoid of counterpart candidates. The source exhibits elliptical emission with a semi major axis of $14 \pm 1$ arc minutes and a semi minor axis of $9 \pm 1$ arc minutes. HESS J1614–518 is one of the two brightest new sources detected with a flux corresponding to 25% of that from the Crab Nebula above 200 GeV. The spectrum is well fit by a power-law of photon index $2.46 \pm 0.20$ (see Figure 5.8 (top right). A nearby *Chandra* observation (Kastner et al., 2003) covers an area 10 arc minutes and more away from the best fit position of HESS J1614–518 and showed no evidence for X-ray emission. The poor quality of the fit to the radial distribution of HESS J1614–518 as is shown in Figure 5.8 (bottom right) indicates that the source is not radially symmetric.

### 5.4.2 HESS J1616–508

HESS J1616–508 (see Figure 5.9) with a flux of 14% of the Crab Nebula above 200 GeV is also one of the brighter new sources of VHE $\gamma$-rays. Its spectrum can be fitted by a power-law of photon index $2.27 \pm 0.08$ as shown in Figure 5.9 (top right). The emission region is extended to 16 arc minutes and is not positionally coincident with any known counterpart at other wavelengths. It is located in a region close to the known SNRs G332.4–0.4 (RCW 103) and G332.4+0.1 (Kes 32). The region has been intensively studied with X-ray satellites like *Chandra* (Vink, 2004) and *XMM*, with the position of HESS J1616–508 mostly outside or at the edge of the field of view where the sensitivity is strongly decreased. No extended X-ray source that lines up with the VHE $\gamma$-ray emission has been found. Another interesting object in this region is the young and energetic pulsar

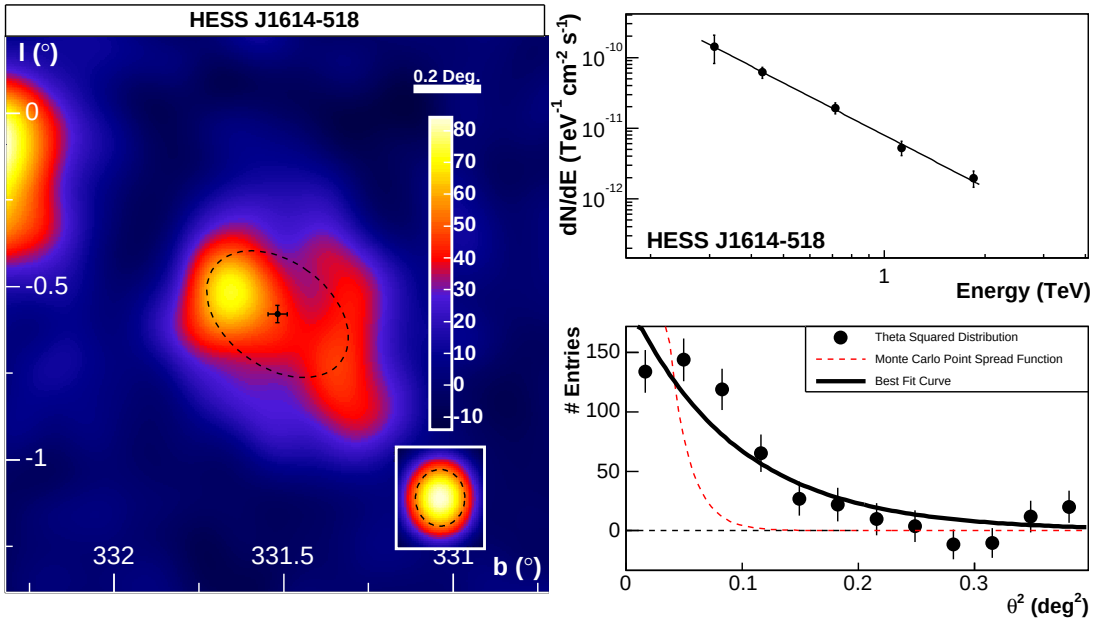


**Figure 5.8:** Smoothed excess map (left) of the region of HESS J1614–518 (smoothing radius 0.09°). The figures on the right hand side show the energy spectrum (top) and $\theta^2$ plot (bottom).

PSR J1617–5055 (Torii et al., 1998), a hard X-ray pulsar, that was proposed to emit TeV $\gamma$-rays (Hirotani, 2001). Less than 1% of its spin-down luminosity would suffice to power the observed VHE $\gamma$-ray emission. Since HESS J1616-508 does not line up with this object, an asymmetric (yet undetected) PWN nebula powered by the pulsar would be required to explain the TeV emission as observed e.g. for MSH–15–5*2* (Aharonian et al., 2005f).

### 5.4.3 HESS J1632–478

The centroid position of this object (right hand source in Figure 5.10 (top)) and of the close-by HESS J1634–472 are spatially separated by less than 45 arc minutes. HESS J1632–478 has an elongated shape with a semi-major axis of 12 ± 3 arc minutes and a semi-minor axis of 3.6 ± 2.4 arc minutes. Its flux in VHE $\gamma$-rays above 200 GeV corresponds to 22% of the flux from the Crab Nebula and the spectrum can be fitted by a power-law of photon index 2.49±0.19 (see Figure 5.10 (bottom left)). Again for HESS J1632–478, the bad quality of the fit to the radial distribution gives some indication that the source might not be radially symmetric but rather elliptically shaped. A positional coincidence of HESS J1632–478 exists with the hard X-ray source IGR J16320–4751 discovered by the INTEGRAL satellite (Tomsick et al. , 2003) in the energy range above 15 keV. In softer X-rays between 2 and 10 keV, this object was also strongly detected in an *XMM-Newton* observation (Rodriguez et al., 2003) and found to be coincident with the ASCA source AX J1631.9-4752, detected in the ASCA Galactic Plane survey (Sugizaki et al., 2001). This source is believed to belong to a new class of heavily absorbed high mass X-ray

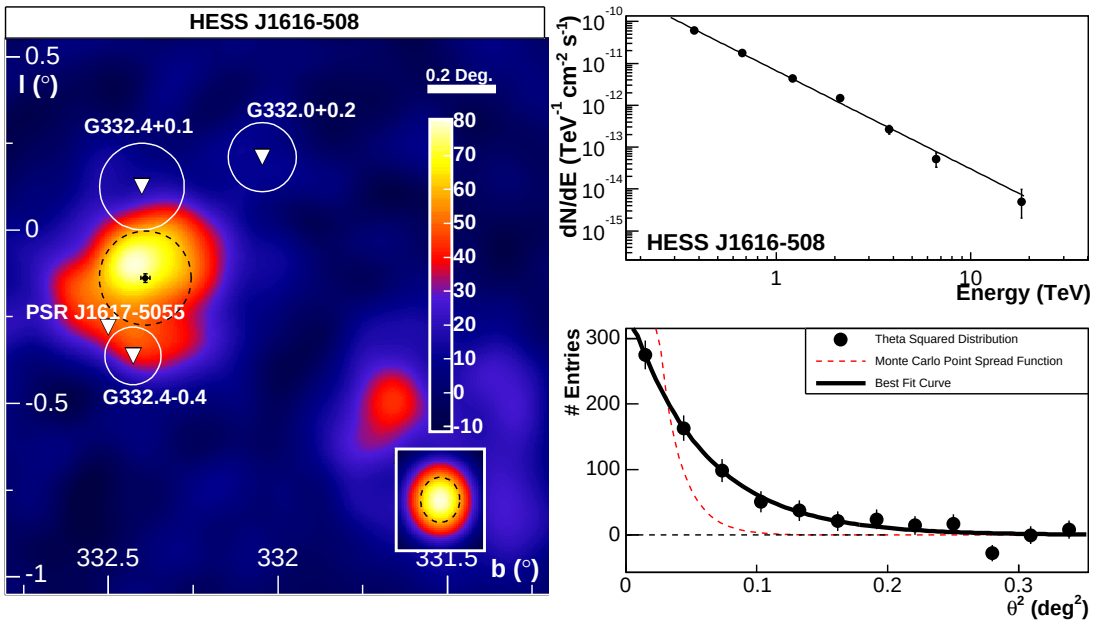


**Figure 5.9:** Smoothed excess map (left) of the region surrounding HESS J1616–508 (left hand source). HESS J1614–518 is also visible in this map (right hand source), along with nearby pulsars and SNRs which were considered as counterparts (smoothing radius 0.06°). The figures on the right hand side show spectrum (top) and $\theta^2$ (bottom) plot of HESS J1616–508.

binary systems, with an equivalent absorption column density of $(9.2 \pm 1.1) \times 10^{22}$ cm$^{-2}$ in this case.

### 5.4.4 HESS J1634–472

The size of the HESS J1634–472 (left hand source in Figure 5.10 (top)) emission region is 6.6 ± 1.8 arc minutes and its flux above 200 GeV is again close to 7% of the Crab flux with a photon index for the energy spectrum of 2.30 ± 0.16 (see Figure 5.10 (middle left)). HESS J1634–472 has no direct positional counterpart, although it is interesting to note that yet another INTEGRAL source IGR J16358-4726 is located close-by (Revnitsev et al., 2003). This source presumably belongs to the class of highly absorbed X-ray binary system like IGR J16320-4751 (which is in positional coincidence with HESS J1632–478). The source was detected in the 2-10 keV X-ray band with the *Chandra* satellite (Patel et al., 2004). The column density determined for this object is $N_H = 3.3 \times 10^{23}$ cm$^{-2}$ and the luminosity of this object in the 2–10 keV band is $10^{36}$ ergs/s.

### 5.4.5 HESS J1640–465

As can be seen from the radial distribution of this source (see Figure 5.11 (bottom right)) HESS J1640–465 is marginally extended with respect to the PSF of the instrument. It is one of the few examples of a perfect spatial correlation between the VHE $\gamma$-ray emission and an SNR (G338.3–0.0), known from radio observations (Green, 2004) (shown in black

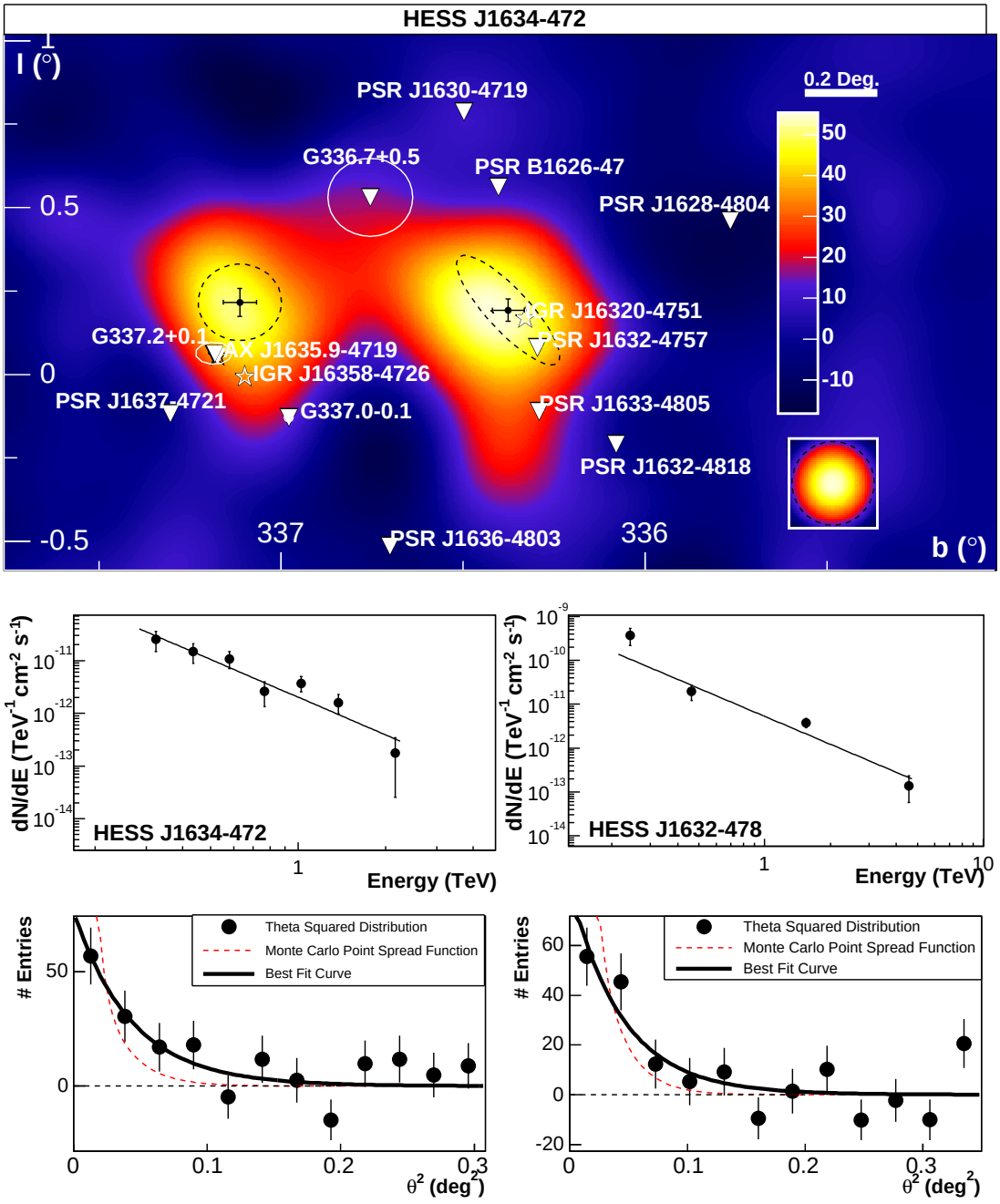


**Figure 5.10:** Smoothed excess map (top) of the region of the two close-by H.E.S.S. sources HESS J1634–472 (left hand source) and HESS J1632–478 (right hand source), along with nearby pulsars and SNRs which were considered as counterparts (smoothing radius 0.12°). The figures in the middle row show the spectra (left: HESS J1634–472, right HESS J1632–478), the figures in the bottow row the corresponding $\theta^2$ plots.

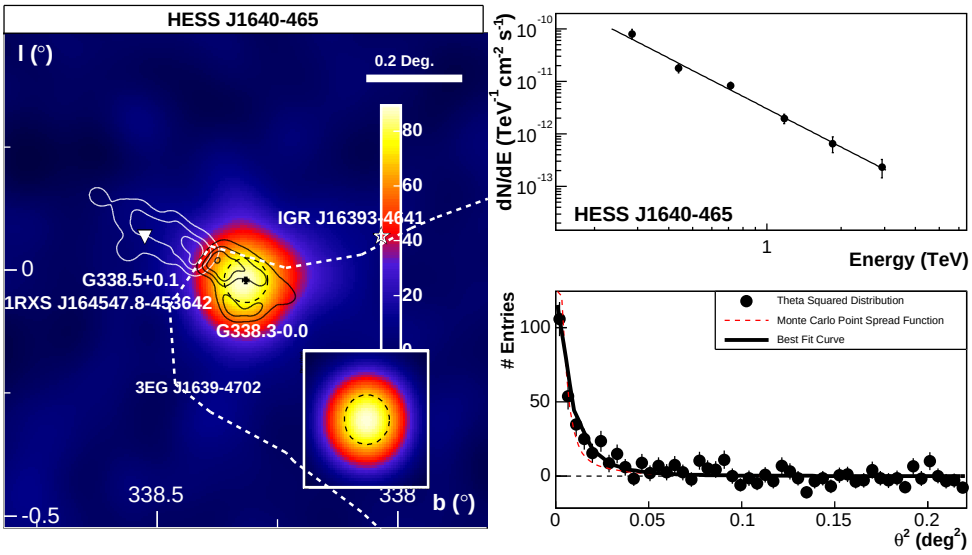


**Figure 5.11:** Smoothed excess map (left) of the region surrounding HESS J1640–465 along with nearby pulsars and SNRs which were considered as counterparts as discussed in the text (smoothing radius 0.05°). The black and the white contours indicate the radio emission detected from the region surrounding G338.3–0.0 in the Molonglo Galactic Plane survey at 843 MHz (Whiteoak & Green, 1996). The dashed white contours show the 95% positional error of the unidentified EGRET source 3EG J1639-4702. The differential energy spectrum (upper right) and the radial (lower right) distribution ($\theta^2$) plot are shown on the right hand side.

and white contours in Figure 5.11 (left)). G338.3–0.0 was observed in the Molonglo Galactic Plane survey at 843 MHz and has been reported to be a broken shell SNR lying on the edge a bright HII region (Whiteoak & Green, 1996). The ASCA source AX J164042-4632, detected during the ASCA Galactic Plane survey (Sugizaki et al., 2001) has been identified with G338.3–0.0. It should be noted, that the position of HESS J1640–465 is compatible with the VHE $\gamma$-ray emission region is the unidentified EGRET source 3EG J1639–4702 (Hartman et al., 1999). The 95% positional contour level is shown in Figure 5.11 (left). The distance of HESS J1640–465 to this EGRET source is 34 arc minutes. The differential energy spectrum of HESS J1640–465 can be well fit by a power-law with photon index 2.42±0.10 at a flux close to 7% of that from the Crab Nebula above 200 GeV (see Figure 5.11 (top right)). A simple power-law extrapolation of the VHE $\gamma$-ray spectrum to 1 GeV matches the EGRET flux above that energy.

### 5.4.6 HESS J1702–420

For HESS J1702–420 (Figure 5.12) no significant evidence for extension of the emission region can be derived. Its emission region is extended at the $2\sigma$-level with a size of 0.08° ± 0.04°. The flux above 200 GeV of this source corresponds to 7% of the Crab flux and the energy spectrum can be fitted by a power law of photon index 2.31±0.15 (see

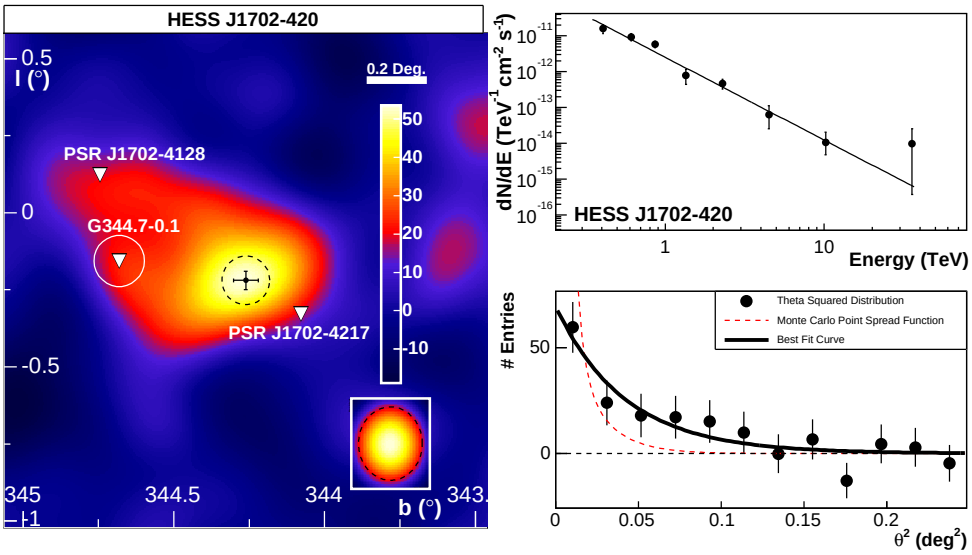


**Figure 5.12:** Smoothed excess map (left) of the region surrounding HESS 1702–420 along with nearby pulsars and SNRs which were considered as counterparts as discussed in the text (smoothing radius 0.10°). The differential energy spectrum (upper right) and the radial (lower right) distribution ($\theta^2$) plot are shown on the right hand side.

Figure 5.12 (top right)). The two close-by pulsars PSR J1702–4128 and PSR J1702–4217 are not energetic enough to account for the observed VHE $\gamma$-ray emission. Therefore this source has so far no plausible counterpart in any other wave-band.

### 5.4.7 HESS J1708–410

This VHE $\gamma$-ray source (Figure 5.13) of size $3.2 \pm 0.7$ arc minutes is located very close to SNR RX J1713.7–3946 and therefore its observation live time within 2° of the pointing position of the instrument amounts to 37.2 hours well beyond typical exposures in the H.E.S.S. survey. The source exhibits an energy spectrum with a power-law index of $2.34 \pm 0.11$, the flux above 200 GeV is less than 4% of the flux from the Crab Nebula (see Figure 5.13 (top right)). As can be seen from Figure 5.13 (left), there is no close-by plausible counterpart. A nearby *XMM* observation of the SNR G345.7–0.2 has revealed no X-ray counterpart to the VHE $\gamma$-ray source, but it should be noted that the offset of HESS J1708–410 from the centre of the *XMM* field of view was 15 arc minutes, positioning it close to the edge of the field of view. As can be seen from the radial distribution, shown in Figure 5.13 (bottom right), the source is only marginally extended with respect to the PSF of the instrument.

### 5.4.8 HESS J1713–381

This source (Figure 5.14) is the second of the fourteen VHE sources that shows no significant evidence for an extension of the emission region. The energy spectrum of

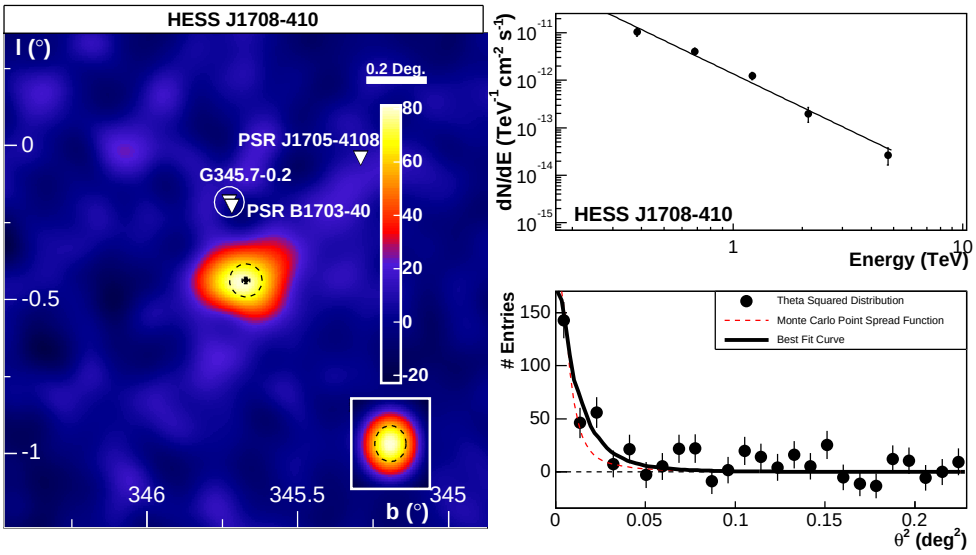


**Figure 5.13:** Smoothed excess map (left) of the region surrounding HESS J1708–410 along with nearby pulsars and SNRs which were considered as counterparts as discussed in the text (smoothing radius 0.05°). The differential energy spectrum (upper right) and the radial (lower right) distribution ($\theta^2$) plot are shown on the right hand side.

HESS J1713–381 is consistent with a power-law with photon index 2.2±0.5. Its flux of 1.8% of the flux from the Crab Nebula above 200 GeV puts this object among the weakest of the new sources. Its location is very close to the strong VHE $\gamma$-ray source Supernova remnant RX J1713.7–3946 and it was therefore in the field of view of most pointed observations by H.E.S.S. on this object. The correspondingly deep exposure of 37 hours at offsets of less than 2° from the centre of the field of view made it possible to detect this object. As can be seen from Figure 5.14 (left), it coincides with part of the unusual Supernova remnant complex CTB 37. The radio contours of the CTB 37 complex as taken from the Molonglo Plane survey at 843 MHz are shown in white (Whiteoak & Green, 1996). There is clear positional match between the source HESS J1713–381 and the SNR G 348.7+0.3 (CTB 37 B). Also visible in Figure 5.14 (right) is a weaker marginal source consistent with the position of the CTB 37 A. The marginal detection of emission from this source is however not significant after accounting for all trials for the analysis of extended sources in this survey as described above. Kassim, Baum, & Weiler (1991) describe CTB 37 A as two SNRs overlapping in projection: with the partial shell of G348.7+0.1 in the west and the SNR G 348.5–0.0 to the east. Both SNRs in CTB 37A appear to be interacting with a system of molecular clouds with densities of 100-1000 cm$^{-3}$ (Reynoso & Mangum, 2000). The SNR CTB 37 B is less well studied but appears to share the dense environment of CTB 37 A.

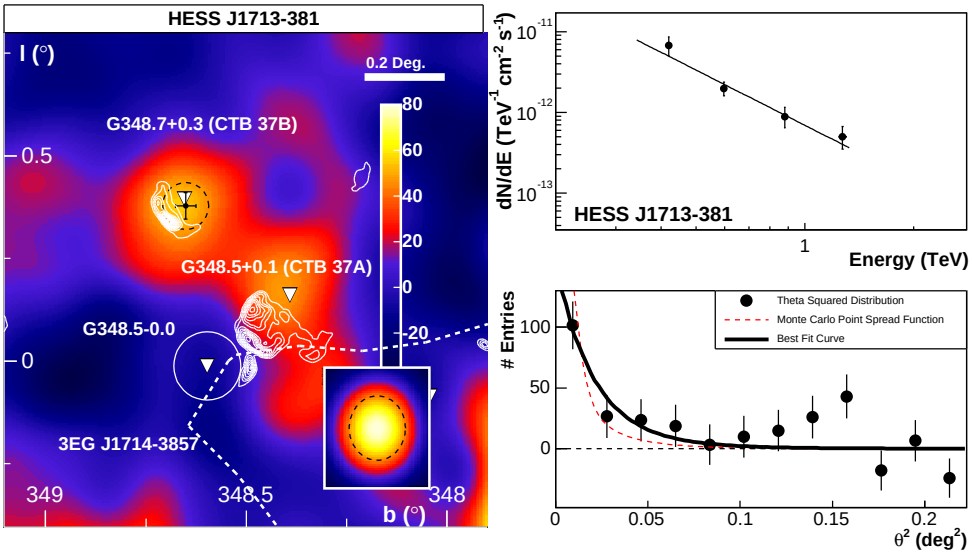


**Figure 5.14:** Smoothed excess map (left) of the region surrounding HESS J1713–381 along with nearby pulsars and SNRs which were considered as counterparts as discussed in the text (smoothing radius 0.07°). In the bottom right corner of this excess map, the strong VHE emission from SNR RX J1713.7–3946 is apparent. The white contours show the radio emission as seen in the Molonglo Plane survey at 843 MHz (Whiteoak & Green, 1996). The marginal excess in positional agreement with CTB 37 A is not significant after accounting for all trials for the analysis presented here. The differential energy spectrum (upper right) and the radial (lower right) distribution ($\theta^2$) plot are shown on the right hand side. Also in the radial distribution, some indication for an excess $\approx 0.4\,^\circ$ away from HESS J1713–381 can be seen, due to the marginal excess at the position of CTB 37 A.

### 5.4.9 HESS J1745–290

This source in the direct vicinity of the centre of our Galaxy has been previously published (Aharonian et al., 2004b). HESS J1745–290 exhibits a power-law energy spectrum with a spectral index of 2.33 ±0.04, with a flux at the level of 9% of the Crab flux above 1 TeV. The emission region is slightly extended as can be seen from Figure 5.15 (lower right). The Galactic Centre region (Melia & Falcke, 2001) harbours a variety of potential sources of high-energy radiation including the super-massive black hole Sgr A* of $2.6 \times 10^6$ $M_\odot$ (see e.g. Schoedel Schoedel et al. (2002)), which has been identified as a faint source of X-rays (Baganoff et al., 2003) and infrared radiation (Genzel et al., 2003). Emission from Sgr A* is presumably powered by the energy released in the accretion of stellar winds onto the black hole (Melia, 1992; Yusef-Zadeh, Melia, & Wardle, 2000; Yuan, Quataert, & Narayan, 2003)). The $\gamma$-radiation could result from acceleration of electrons or protons in shocks in these winds, in the accretion flow or in nearby SNRs, followed by interactions of accelerated particles with ambient matter or radiation. Another source of VHE $\gamma$-rays is the diffuse emission from the entire central region. $\gamma$-rays may result from interactions of accelerated protons and nuclei (Fatuzzo, & Melia, 2003) with the ambient matter with a density as large as $n = 10^3\,\mathrm{cm}^{-3}$ (Maeda et al., 2002). Only modest overall energy, $W_\mathrm{p} \simeq 5 \times 10^{47}(10^3\,\mathrm{cm}^{-3}/\mathrm{n})$ erg, in TeV protons is needed to explain the observed $\gamma$-ray flux from this region. An obvious candidate for the proton accelerator could be the young ($10^4$ yr) and unusually powerful (total explosion energy $\simeq 4\times10^{52}$ erg) supernova remnant Sgr A East (Maeda et al., 2002). Given the location of the black hole Sgr A* within the projection of Sgr A East on the sky (seen in Figure 5.15 (left) and the estimated systematic positional error of at least 20 arc seconds of the position of HESS J1745–290, no firm conclusion can yet be drawn which of these two potential associations is responsible for the VHE $\gamma$-ray emission. The position of Sgr A* is at a distance of 18 arc seconds from the best fit position of HESS J1745–290 and therefore well compatible with the source of the emission. An unambiguous proof of this association would require the observation of correlated variability in VHE $\gamma$-rays and other wavebands or an improvement of the pointing accuracy which is under investigation at this moment.

### 5.4.10 HESS J1745–303

This object (Figure 5.16) has a direct positional coincidence with an unidentified EGRET source (3EG J1744–3011) (Hartman et al., 1999). Since it is within the field of view of the Galactic Centre, HESS J1745–303 has a large observation live time of 35.3 hours. Its flux level corresponds to 5% of the flux from the Crab Nebula above 200 GeV and the photon index of the spectral power-law fit has a hard value of 1.8±0.3. Its emission region has an elliptical shape with a semi-major axis of 13 ± 4 arc minutes and a semi-minor axis of 5.4 ± 2.4 arc minutes as is shown in Figure 5.16 (left). The distance of HESS J1745–303 to the EGRET source 3EG J1744–3011 is 10 arc minutes and is well within the 95% uncertainty level of the EGRET position. A simple power law extrapolation of the VHE $\gamma$-ray spectrum to energies above 1 GeV is an order of magnitude below the EGRET flux above that energy. A correlation between HESS J1745–303 is therefore only possible if the energy spectrum gets softer in the 10 to 250 GeV range or if one assumes an emission

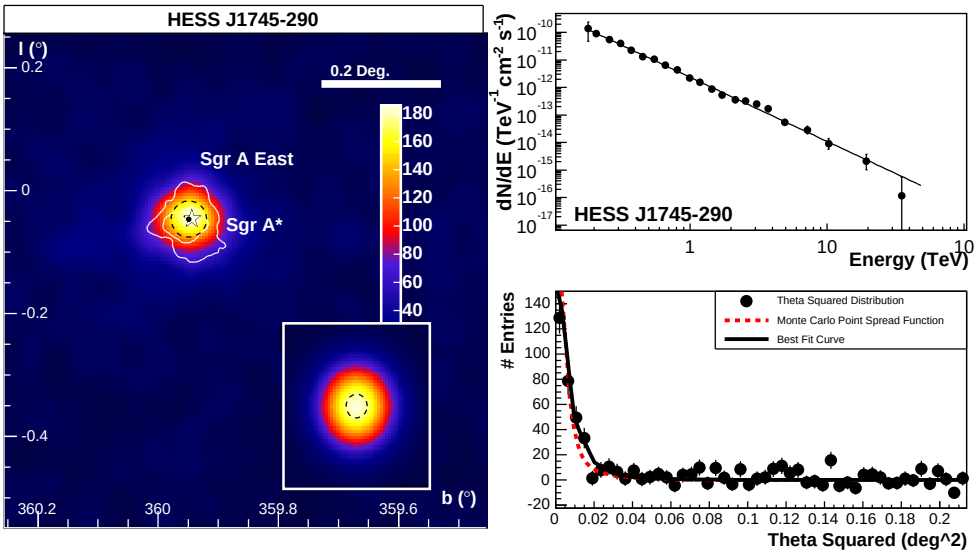


**Figure 5.15:** Smoothed excess map (left) of the region surrounding HESS J1745–290 (smoothing radius 0.02°) along with a 90 cm radio map of the central region of our Galaxy, containing emission from Sgr A East and Sgr A*. The differential energy spectrum (upper right) and the radial (lower right) distribution ($\theta^2$) plot are shown on the right hand side.

mechanism that does not follow a simple power law. To solve this problem, detection of the source in the interesting energy range above 10 GeV is necessary as can be provided by the GLAST satellite or future low-threshold Cherenkov telescopes like HESS-II.

### 5.4.11 HESS J1747–281

HESS J1747–281 has been serendipitously discovered during observations on the Galactic Centre region and has been previously published (Aharonian et al., 2005d). The source is point-like as can be seen from Figure 5.17 (lower right) and exhibits a power-law spectrum with spectral index 2.46 ± 0.13. Its flux of 2% of the Crab flux above 1 TeV makes it a rather weak source. HESS J1747–281 is positional coincident with the SNR G 0.9+0.1 as is evident from Figure 5.17 (left). G 0.9+0.1 is a well known composite SNR, recognised as such from its radio morphology (Helfand, & Becker, 1987). The 20 mm radio contours are shown as white contours in Figure 5.17 (left). G 0.9+0.1 exhibits a bright compact radio core (∼2′ across) surrounded by an 8′ diameter shell. X-ray observations of the nebula with BeppoSAX (Mereghetti, Sidoli, & Israel, 1998), Chandra (Gaensler, Pivovaroff, & Garmire, 2001)) and XMM-Newton (Porquet, Decourchelle, & Warwick, 2003) have unambiguously identified the core region as a pulsar wind nebula (PWN), however no pulsed emission has been detected. Observations with XMM have revealed a softening of the X-ray spectrum with increasing distance from the centre of the PWN, a signature of energy loss of electrons within the nebula. The location of G 0.9+0.1 in the Galactic Centre (GC) region suggests a distance of ∼8.5 kpc (Mezger, Duschl, & Zylka, 1996). At this distance the size of the shell implies an age of a few thousand years for the SNR.

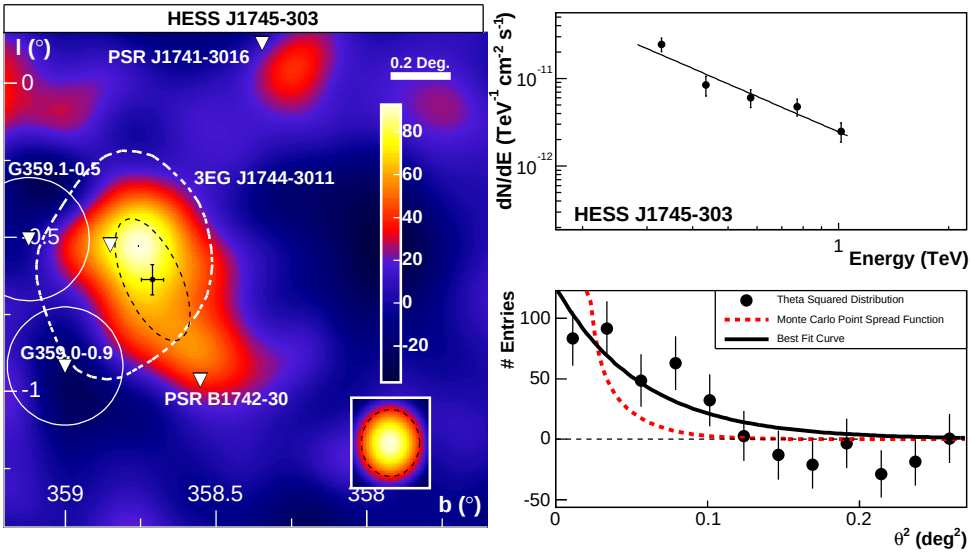


**Figure 5.16:** Smoothed excess map (left) of the region surrounding HESS J1745–303 along with nearby pulsars and SNRs which were considered as counterparts as discussed in the text (smoothing radius 0.10°). The differential energy spectrum (upper right) and the radial (lower right) distribution ($\theta^2$) plot are shown on the right hand side.

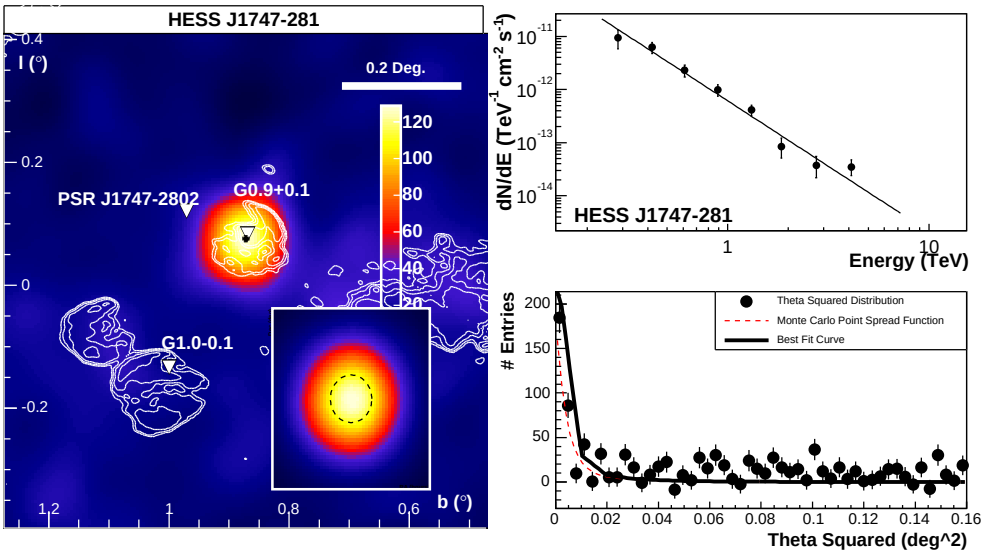


**Figure 5.17:** Smoothed excess map (left) of the region surrounding HESS J1747–281 along with nearby pulsars and SNRs which were considered as counterparts as discussed in the text (smoothing radius 0.09°). The white contours show the radio emission of the region at 90 cm. The positional coincidence with the SNR G0.9+0.1 is apparent. The differential energy spectrum (upper right) and the radial (lower right) distribution ($\theta^2$) plot are shown on the right hand side.

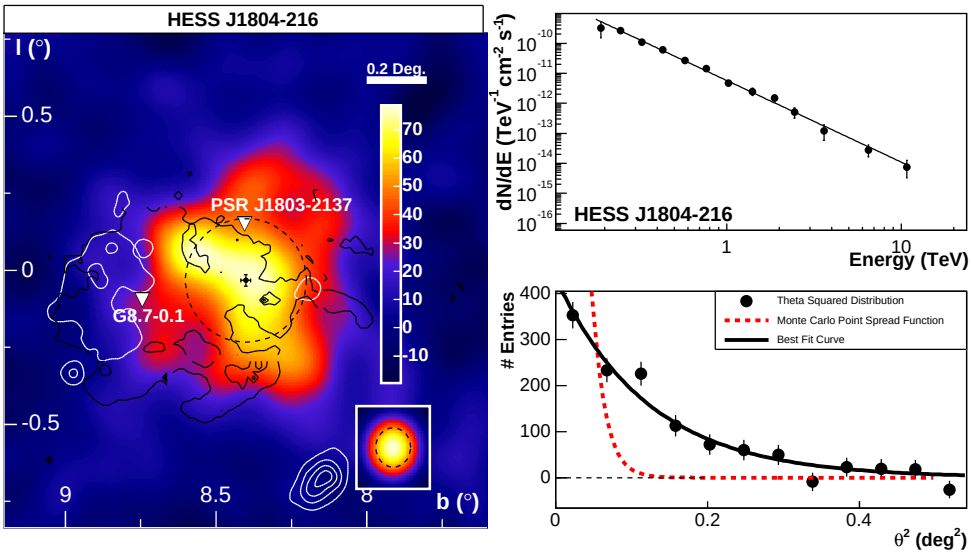


**Figure 5.18:** Smoothed excess map (left) of the region surrounding HESS J1804–216 along with nearby pulsars and SNRs which were considered as counterparts as discussed in the text (smoothing radius 0.06°). The white contours show the X-ray emission from G8.7–0.1 as detected by the ROSAT satellite, the black contours show the 20cm radio emission detected by the VLA. The differential energy spectrum (upper right) and the radial (lower right) distribution ($\theta^2$) plot are shown on the right hand side.

### 5.4.12 HESS J1804–216

This source (Figure 5.18) with a size of approximately 22 arc minutes is the biggest of the new emission regions of VHE $\gamma$-rays. With a flux of nearly 24% of the flux from the Crab Nebula above 200 GeV, it is also the brightest of the new H.E.S.S. sources. The photon index of 2.72±0.06 makes it one of the softest sources (see Figure 5.18 (top right)). As can be seen from Figure 5.18 (left) , the emission region does not perfectly line up with any known object, although it could be associated with the south-western part of the shell of the Supernova remnant G8.7–0.1 of radius 26 arc minutes. From CO observations, the surrounding region is known to be associated with molecular gas where massive star formation takes place (Ojeda-May et al., 2002). The white contours in Figure 5.18 (left) show X-ray emission as detected by the ROSAT satellite (Finley & Ögelman, 1994), the black contours show the 20cm radio emission as recorded by the VLA. Another plausible association of HESS J1804–216 is the young Vela-like pulsar PSR J1803–2137 with a spin-down age of 16000 years (Kassim & Weiler, 1990). The required efficiency of this pulsar's energy to power the observed emission in $\gamma$-rays is only 1% and could therefore easily account for the new source.

### 5.4.13 HESS J1813–178

With a moderate flux of approximately 6% of the Crab Nebula above 200 GeV, this source (see Figure 5.19) is among the more compact of the new sources ($\sigma_{\text{source}} = 0.02°$).

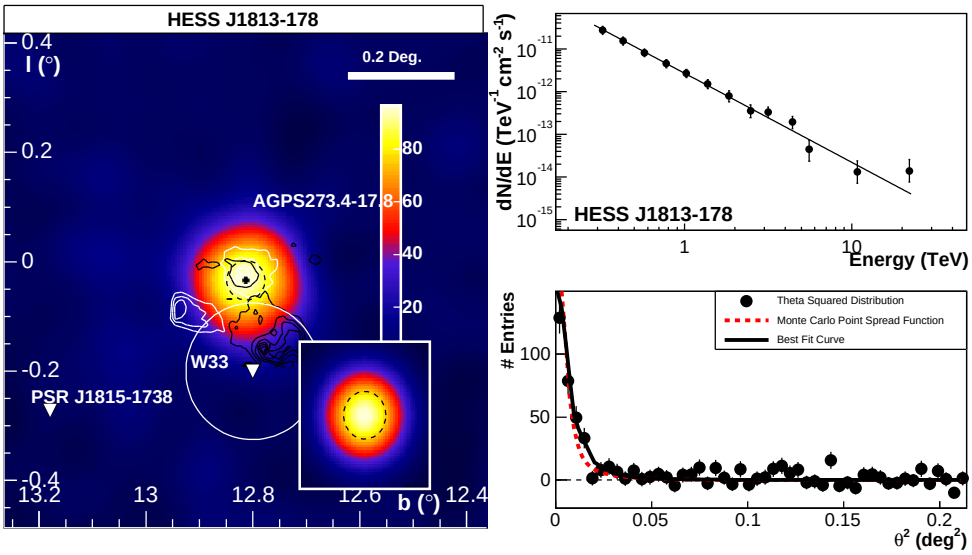


**Figure 5.19:** Smoothed excess map (left) of the region surrounding HESS J1813–178 along with nearby pulsars and SNRs which were considered as counterparts as discussed in the text (smoothing radius 0.04°). The black contours show the X-ray emission from AGPS273.4-17.8 as detected by the ASCA satellite, the black contours show 20 cm radio emission as observed by the VLA. The radial (lower right) distribution ($\theta^2$) plot shows that the source is marginally extended with respect to the PSF of the H.E.S.S. system.

When using a large $\theta^2$ cut of $(0.4°)^2$, the normalisation of the power-law fit is 25% higher, suggesting a slight deviation from the radial symmetry. The source exhibits a rather hard photon index of 2.09±0.08 (see Figure 5.19 (top right)). As is clear from Figure 5.19 (left), there is a compelling positional coincidence between this source and the X-ray source AGPS273.4 17.8 (Sakano, 2002) (black contours in figure 5.19). This unidentified ASCA source is one of the brightest sources detected in the ASCA Galactic Plane survey and has a very hard energy spectrum. This region was also observed with the VLA and 20 cm radio contours are shown in black in Figure 5.19. There is some faint radio emission visible at the position of HESS J1813–178. Additionally HESS J1813–178 lies 10 arc minutes from the centre of the radio source W 33. W 33 extends over 15 arc minutes and has a compact radio core (G 12.8–0.2) which is 1 arc minutes across (Haschick & Ho, 1983), located $\sim$ 15 arc minutes away from HESS J1813–178. The W33 region shows signature of an ultra-compact HII region (Churchwell, 1990) and contains methanol, hydroxyl and water masers and other tracers of recent star formation, that could act as target material for the generation of VHE $\gamma$-rays.

### 5.4.14 HESS J1825–137

This source has an energy spectrum with a photon index of 2.46 ± 0.08 and a flux of VHE $\gamma$-rays of approximately 17% of the flux from the Crab Nebula above 200 GeV

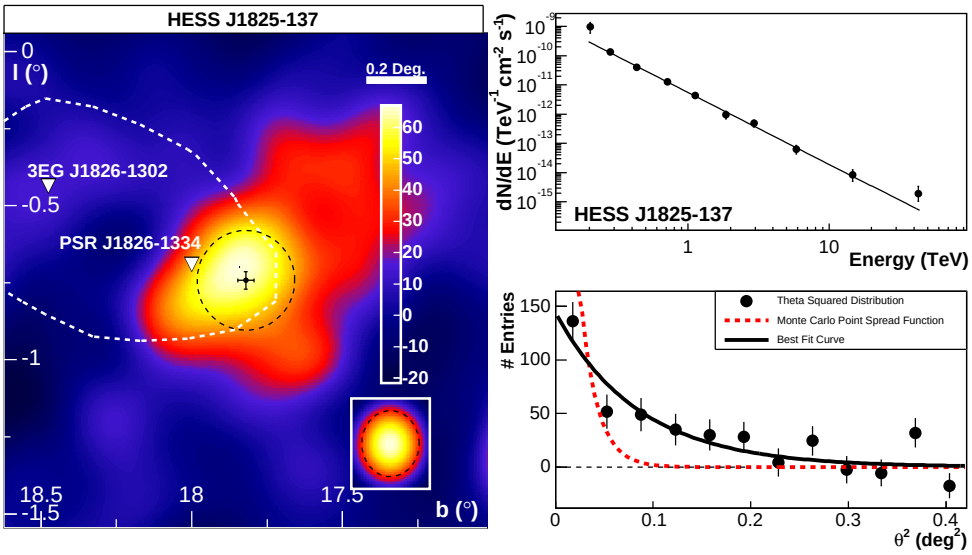


**Figure 5.20:** Smoothed excess map (left) of the region surrounding HESS J1825–137 along with nearby pulsars and SNRs which were considered as counterparts as discussed in the text (smoothing radius 0.09°). The differential energy spectrum (upper right) and the radial (lower right) distribution ($\theta^2$) plot are shown on the right hand side.

(see Figure 5.20 (top right)). It is radially symmetric and the emission region can be best described by a Gaussian of width $\sigma_{\text{source}} = 0.16°$. The position of HESS J1825–137 is approximately 11 arc minutes to negative Galactic longitudes of the young pulsar PSR B1823–13 (PSR J1826–1334), which makes an association of the VHE $\gamma$-ray source with the pulsar plausible. The pulsar PSR B1823–13 is a 101 ms evolved Vela-like pulsar at a distance of 3.9 ± 0.4 kpc. The region surrounding the pulsar has been previously observed at large zenith angles by the Whipple collaboration (Hall et al., 2003), who observed a $3.1\sigma$ excess also to negative Galactic longitudes with respect to the pulsar position. X-ray observations with the *XMM-Newton* satellite show a 5 arc minutes diameter diffuse emission region extending also asymmetrically to negative Galactic longitudes from the pulsar (Gaensler et al., 2003). If the VHE $\gamma$-ray source is indeed associated with this pulsar wind nebula, the VHE emission region would extend much further to the south than in X-rays. This possible association can be explained by past history of pulsar injection into the wind nebula and the effect of synchrotron cooling on the injected electrons and wind confinement due to swept up gas from an unseen SNR. PSR B1823–13 was also proposed to power the close-by unidentified Egret source 3EG J1826–1302 (Nolan et al., 2003). The distance of this EGRET source to HESS J1825–137 is 43 arc minutes. As illustrated in Figure 5.20 (left) the new VHE $\gamma$-ray source is well compatible with the EGRET source within the 95% positional error of EGRET and a simple power-law extrapolation of the H.E.S.S. energy spectrum to energies above 1 GeV gives a similar flux as derived from the EGRET spectrum above this energy. An in-depth study of HESS J1825–137 and dicussion about the corresponding PWN model will be given in a seperate paper.

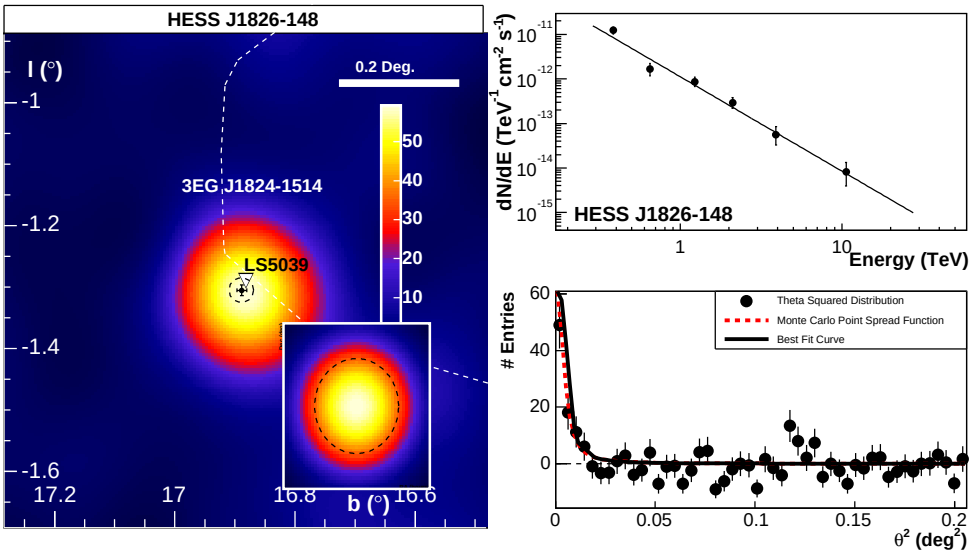


**Figure 5.21:** Smoothed excess map (left) of the region surrounding HESS J1826–146 along with nearby pulsars and SNRs which were considered as counterparts as discussed in the text (smoothing radius 0.07°). The differential energy spectrum (upper right) and the radial (lower right) distribution ($\theta^2$) plot are shown on the right hand side.

### 5.4.15 HESS J1826–146

This source is only significantly detected using the point-source $\theta^2 = 0.01$ cut, in fact this is the only additional source that is found when using this cut instead of the extended $\theta^2 = 0.05$ cut. The emission region is point-like an the plot of the squared angular distance with respect to the best fit position lines up with the PSF of the instrument as shown in Figure 5.21 (right bottom). The energy spectrum of this object can be fitted with a power-law of photon index 2.12±0.15 and the flux of this object above 1 TeV corresponds to 5% of the Crab flux (Figure 5.21 right top). HESS J1826-146 is located $\sim 1°$to negative Galactic latitudes with respect to HESS J1825-137. It is located in the close vincinity of the X-ray binary system LS5039 as can be seen in Figure 5.21 (left). This X-ray binary system was first detected in the ROSAT all sky survey (Motch et al., 1997), has a low variability and was estimated to be at a distance of 3.1 kpc. LS5039 has been proposed to be associated with the unidentified EGRET source 3EG J1824–1514 (Paredes et al., 2000) but this association is uncertain at this stage. It has resolved radio structures detected by the Very Large Baseline Array (VLBA) (Paredes et al., 2000) and can hence be seen as a microquasar candidate. The distance of HESS J1826–146 to the radio position of LS5039 is 63 arc seconds, whereas the statistic error on the position is 30 arc seconds in each coordinate. Therefore although an association is very likely, given a typical systematic error in the pointing of at least 20 arc seconds, a firm association can not yet been established and needs a deeper investigation.

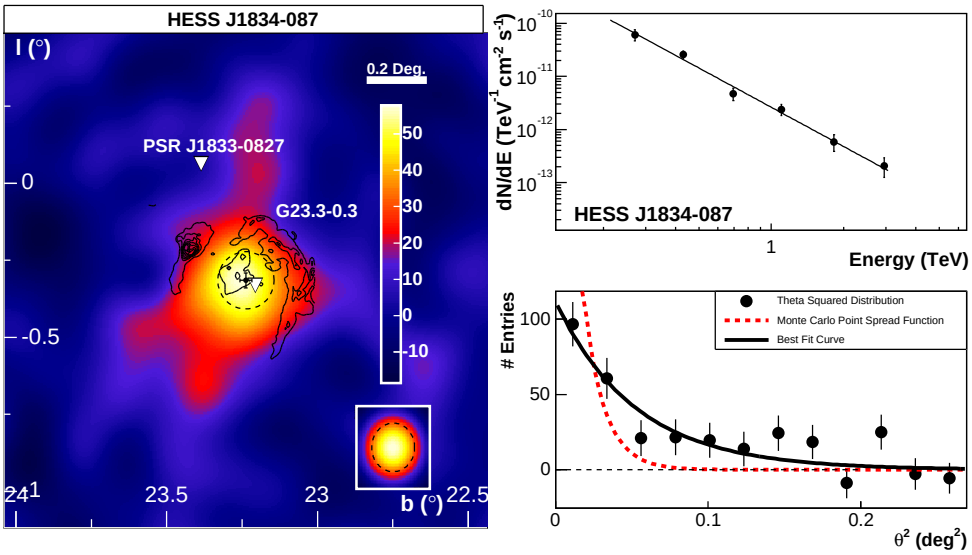


**Figure 5.22:** Smoothed excess map (left) of the region surrounding HESS J1834–087 along with nearby pulsars and SNRs which were considered as counterparts as discussed in the text (smoothing radius 0.08°). The positional coincidence with SNR G23.3–0.3 (W41) is clearly seen, the black contours show 20 cm radio emission recorded by the VLA. The differential energy spectrum (upper right) and the radial (lower right) distribution ($\theta^2$) plot are shown on the right hand side.

### 5.4.16 HESS J1834–087

HESS J1834–087 (Figure 5.22) has a size of 12 arc minutes and a $\gamma$-ray flux of 9% of the flux from the Crab Nebula above 200 GeV. Its energy spectrum exhibits a photon index of 2.45±0.16 (see Figure 5.22 (top right)). When using a large $\theta^2$ cut of $(0.4°)^2$, the normalisation of the power-law fit increases by 30%, suggesting a deviation of the morphology from the radial Gaussian symmetry. The location of HESS J1834–087 makes it another source with a compelling positional agreement with an SNR (see Figure 5.22 (left)). The positionally coincident shell-type SNR G23.3–0.3 (W 41) with a diameter of 27 arc minutes was mapped in radio at 330 MHz (Kassim, 1992) and also at 20 cm with the VLA (White, Becker, & Helfand, 2005). It is possibly connected to the old pulsar PSR J1833–0827 (Gaensler & Johnston, 1995). This pulsar is energetic enough to power HESS J1834–087, but its distance of 24 arc minutes renders a correlation unlikely.

### 5.4.17 HESS J1837–069

This source (Figure 5.23) has an elongated shape and a flux of 13.4% of the Crab flux above 200 GeV. The energy spectrum can be well fitted by a power law of photon index 2.27±0.06 (see Figure 5.23 (top right)). When using a large $\theta^2$ cut of $(0.4°)^2$, the normalisation of the power-law fit increases by 30%, suggesting that the assumption of radial symmetry does not hold for this source. HESS J1837–069 coincides with the southern part of the diffuse hard X-ray complex G25.5+0.0. This source, which is 12 arc minutes across, was detected

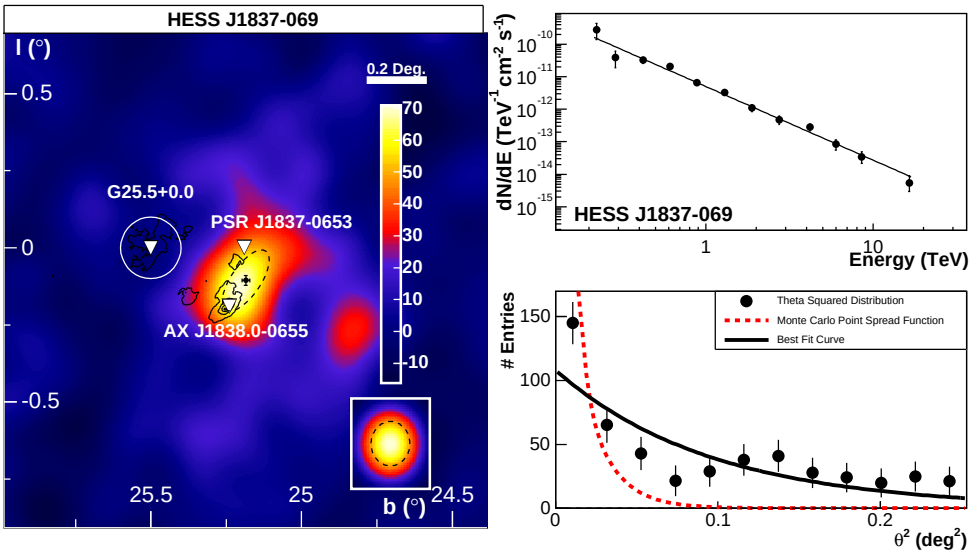


**Figure 5.23:** Smoothed excess map (left) of the region surrounding HESS J1837–069 along with nearby pulsars and SNRs which were considered as counterparts as discussed in the text (smoothing radius 0.05°). Shown in black contours is the X-ray emission as detected by the ASCA satellite from this region. The positional coincidence with the ASCA source AX J1838.0–0655 is clearly seen. The differential energy spectrum (upper right) and the radial (lower right) distribution ($\theta^2$) plot are shown on the right hand side.

in the ASCA Galactic Plane survey (Bamba et al., 2003). The nature of this bright X-ray source is unclear but it may be an X-ray synchrotron emission dominated SNR such as SN 1006 or a PWN. The brightest feature in the ASCA map (AX J1838.0–0655), located south of G25.5+0.0, coincides with the centre of gravity of the VHE emission and is therefore the most promising counterpart candidate. This still unidentified source was also serendipitously detected by BeppoSAX and also in the hard X-ray (20-100 keV) band in the Galactic Plane survey of INTEGRAL (Malizia et al., 2004).

# Chapter 6

# Discussion of the results

While the previous chapter described possible multi-wavelength association of the seventeen sources of VHE $\gamma$-rays individually, this chapter will summarise these associations in the light of populations of sources.

## 6.1 Counterparts in other wavebands

Possible multi-wavelength associations of the seventeen new VHE as discussed in the last chapter are summarised in Table 6.1. A further qualification from tentative associations to unambiguous counterpart identifications requires spatial or morphological coincidence, a viable $\gamma$-ray emission mechanism for the object, and consistent multi-wavelength behaviour according to the properties of the suggested identification. All the possible associations given above can be considered as plausible $\gamma$-ray emitters, but only in five cases does a satisfactory positional coincidence exist. Three of the new sources apparently line up with SNRs. Only in the case of HESS J1640–465 there is a clear association with an SNR known in both radio and X-rays. For HESS J1834–087 and HESS J1713–381 positional coincidences exist with radio-detected SNRs but no X-ray emission has yet been reported. Two sources (HESS J1813–178 and HESS J1837–069) may be related to ASCA detected X-ray emission of unknown origin. For three of the new sources, namely HESS J1616–509, HESS J1804–216 and HESS J1825–137, a sufficiently energetic nearby pulsar could account for the VHE $\gamma$-ray emission but the offset of the sources from the pulsar positions makes these associations less firm. Four of the new VHE $\gamma$-ray sources are consistent with the 95% positional error of unidentified EGRET sources: HESS J1640–465, HESS J1745–303, HESS J1826–148, and HESS J1825–137. HESS J1826–148 is also directly coincident with the microquasar LS5039. Two of the new sources are coincident or located very close to a new class of highly absorbed hard X-ray sources detected recently by INTEGRAL (HESS J1632–478 and HESS J1634–472) with column-densities $N_H \gtrsim 10^{23}$ cm$^{-2}$. The three remaining sources (HESS J1614–518, HESS J1702–420 and HESS J1708–410) have no plausible SNR, pulsar or EGRET counterpart and may belong to a new source class. Significant fluxes of VHE $\gamma$-rays without accompanying X-ray and radio emission would suggest the absence of relativistic electrons and the presence of energetic baryons. That such a population exists is already being suggested by the

**Table 6.1:** Summary of possible counterparts to the H.E.S.S. VHE $\gamma$-ray sources in the inner Galaxy. The Offset denotes the offset of the VHE $\gamma$-ray source from the possible counterpart, the last column gives the implied luminosity between 0.2 and 10 TeV. The sources in this table are grouped by possible counterparts. The H.E.S.S. source coincident with the SNR RX J1713.7-3946 (HESS J1713–397) has been added for completeness to this table.

| Name | Possible Counterpart | Class | Offset (arcmin) | Distance (kpc) | Luminosity ($10^{34}$ erg s$^{-1}$) |
|---|---|---|---|---|---|
| J1640–465 | G 338.3–0.0 | SNR | 0 | - | - |
| | 3EG J1639–4702 | UID | 34 | - | - |
| J1713–381 | G 348.7+0.3 | SNR | 0 | 10.2 | 2.0 |
| J1713–397 | RX J1713.7–3946 | SNR | 0 | 1 | 0.3 |
| J1745–290 | Sgr A East | SNR | 0 | 8.5 | 5 |
| | Sgr A$^\star$ | BH | 0 | 8.5 | 5 |
| J1804–216 | G 8.7–0.1 | SNR | 21 | 6 | 6.5 |
| | PSR J1803–2137 | PWN | 10.8 | 3.9 | 2.7 |
| J1834–087 | G 23.3–0.3 | SNR | 0 | 4.8 | 1.7 |
| J1616–508 | PSR J1617–5055 | PWN | 10.4 | 6.5 | 7.9 |
| J1747–281 | G0.9+0.1 | PWN | 0 | 8.5 | 2. |
| J1825–137 | PSR J1826–1334 | PWN | 11 | 3.9 | 2.4 |
| | 3EG J1826–1302 | UID | 43 | - | - |
| J1826–146 | LS5039 | MQ | 1 | 3.1 | 0.3 |
| | 3EG 1824-1514 | UID | 32 | - | - |
| J1745–303 | 3EG J1744–3011 | UID | 10 | - | - |
| J1813–178 | AGPS 273.4–17.8 | UID | 0 | - | - |
| J1837–069 | AX J1838.0–0655 | UID | 6 | - | - |
| J1632–478 | IGR J16320–4751 | UID | 3 | - | - |
| J1634–472 | IGR J16358–4726 | UID | 13 | - | - |
| J1614–518 | - | - | - | - | - |
| J1702–420 | - | - | - | - | - |
| J1708–410 | - | - | - | - | - |

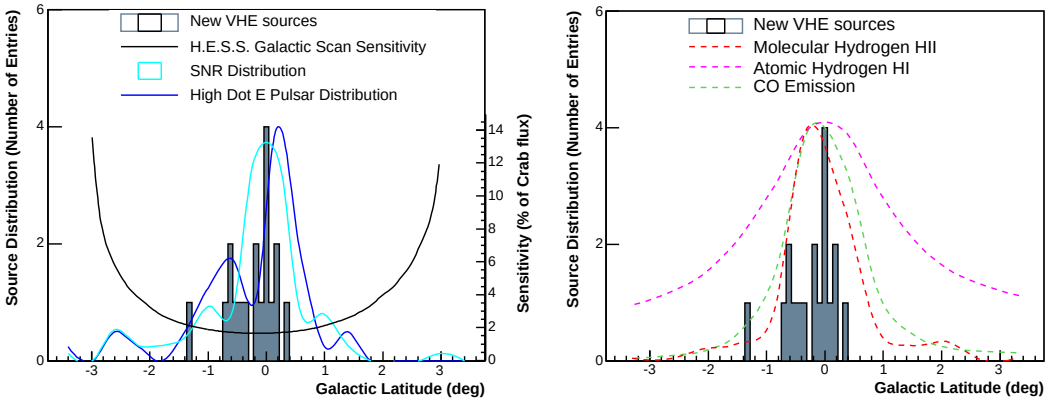


**Figure 6.1:** Distribution of galactic latitude of the seventeen VHE $\gamma$-ray sources as given in Table 6.1 (the fourteen new plus the three previously known). The mean of the distribution is –0.23 with an RMS of 0.38. On the left, the distribution is shown along with the distribution in galactic latitude of possible counterpart populations to the VHE $\gamma$-ray sources. SNRs from Green (2004) are shown in turquoise, high spin-down luminosity pulsars ($\dot{E} > 10^{34}$ erg s$^{-1}$) taken from the ATNF catalogue (Manchester et al., 2005) are shown as a blue curve. On the right the distribution of VHE $\gamma$-ray sources as on the left is shown along with the latitude distributions of matter in our Galaxy. The distribution of molecular hydrogen (HII) (Paladini et al., 2003) is shown in dashed red, the distribution of atomic hydrogen (HI) (Dickey & Lockman, 1990) is shown in dashed purple and the distribution of CO (Dame, Hartman & Thaddeus, 2001) is shown as dashed green line.

detection of apparently "dark" accelerators by the HEGRA (Aharonian et al., 2002a) and H.E.S.S. (Aharonian et al., 2005a) collaborations. However, the possibility remains that these new sources are associated with SNRs or PWN as yet undiscovered at other wavelengths. Further multi-wavelength investigations are needed to clarify this picture.
The nearest lower energy band relative to the H.E.S.S. energy range was covered by observations with the EGRET telescope aboard the Compton Gamma-Ray Observatory. Its energy coverage was primarily between 30 MeV and 10 GeV and $\gamma$-ray source detections above 100 MeV resulted in the third EGRET (3EG) catalogue (Hartman et al., 1999). The only sources detected above 10 GeV are pulsars that have been found due to their characteristic periodicity. The bulge of photons above 10 GeV have to be attributed to galactic (and extra-galactic) diffuse emission.
When comparing the MeV to GeV sources with the H.E.S.S. Galactic Plane survey result, it should be noted that even if an EGRET source spectrum is covered up to 10 GeV, a few decades in energy are left uncovered before the H.E.S.S. energy threshold. Indeed, only a minor fraction of the H.E.S.S. sources coincide within the considerably larger location uncertainty contours of EGRET sources. These sources are HESS J1640–465, HESS J1745–303, HESS J1826-148, and HESS J1825–137, which are consistent with the 95% ($\theta_{95}$) location uncertainty of the unidentified EGRET sources 3EG J1639–4702,

3EG J1744–3011, 3EG J1824–1514, and 3EG J1826–1302. In total 17 EGRET sources are catalogued within the H.E.S.S. survey region. Taking into account the 95% positional error contours ($\theta_{95}$), they cover an area of 9.76 deg$^2$, resulting in a chance positional coincidence with an EGRET source of 7%. In case of the spatial association between 3EG J1824–1514 and HESS J1825–137, plausibly identified with the microquasar LS5039 in both EGRET (Paredes et al., 2000) and H.E.S.S. such a connection is presumably an indication that other objects than members of the known population of galactic EGRET sources may be able to bridge the energetic gap between EGRET and H.E.S.S..

EGRET observations are generally affected by significantly reduced sensitivity (Reimer, 2000) in the inner Galactic Plane for various reasons. The dominant $\gamma$-ray emission originating from cosmic ray interactions, peaks in the $|b| < 0.5^\circ$ range. Thus, the instruments ability to detect point sources is decisively hampered by the apparent galactic diffuse emission. A typical sensitivity in a $|b| < 2^\circ$ range (considering the size of EGRETs PSF) is at the level of $10^{-7}$ cm$^{-2}$ s$^{-1}$. The diffuse $\gamma$-ray emission in the inner Galaxy introduces a bias for source detections according to their spectra: Whereas hard sources can be more easily discriminated against the diffuse emission as a function of energy (where the EGRET PSF narrows, but the number of photons becomes very marginal), soft spectrum emitters are increasingly hard to detect, explaining the noticeable deficit of soft $\gamma$-ray sources in the Galactic Plane from EGRET observations.

Also physical arguments suggest that the EGRET source population and the set of new H.E.S.S. sources might be of different kinds. While the brightest $\gamma$-ray pulsars can be directly traced up to $\sim$ 20 GeV, EGRET data indicates the existence of GeV-cutoffs already in the 2-10 GeV range (Reimer & Bertsch, 2001). The brightest pulsars, and several unidentified EGRET sources with pulsar-like characteristics deviate from single power-law spectral representations (Bertsch et al., 2000), and are significantly better fitted when introducing high-energy spectral cutoffs. GeV-cutoffs are indeed predicted from multi-frequency modelling of the $\gamma$-ray emission of pulsars (Cheng, 2004; Baring, 2004). Therefore, the emission of these unidentified EGRET sources may not extend up to the H.E.S.S. energy range. From Crab measurements by CELESTE (de Naurois et al., 2002), consecutively continuing the EGRET GeV-data, a characteristic change in the emission properties of the pulsar became apparent: pulsed emission is diminished or entirely fading away, leaving only a steady emission component, in case of Crab attributed to the PWN. If the majority of EGRET sources in the Galactic Plane may be identifiable with $\gamma$-ray pulsars, this population will overlap with the H.E.S.S. energies only if a plerionic emission components exist.

For PWN there are theoretical grounds to expect in some cases a displacement of the $\gamma$-ray emission from the pulsar powering the nebula (Aharonian, Atoyan, & Kifune, 1997; Aharonian et al., 2005g). In such cases the association becomes more difficult. Considering only pulsars with sufficient spin-down luminosity to explain the measured VHE $\gamma$-ray flux, five of the new sources have possible associations with pulsar wind nebula. However, only in the case of HESS J1825–137 is there so far a convincing multi-wavelength argument for the offset (both direction and magnitude) from the pulsar position.

The sensitivity of the survey shown in Figure 5.1 is that for point-like ($< 0.1^\circ$) sources. The sensitivity of H.E.S.S. above the trigger threshold decreases with increasing source

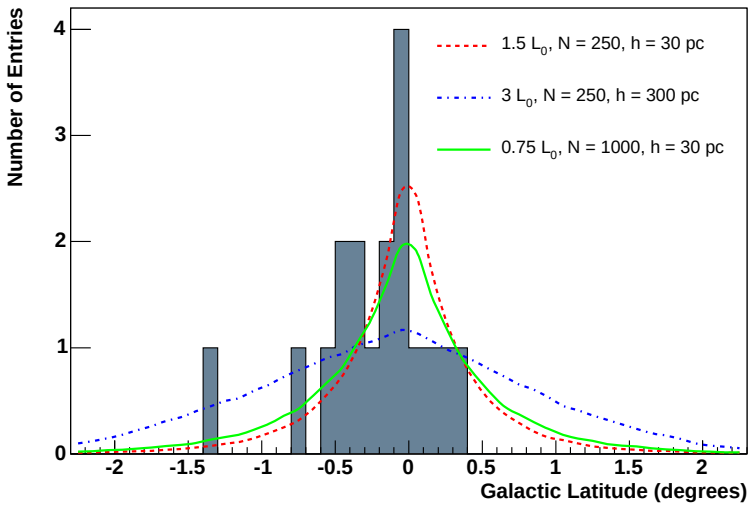


**Figure 6.2:** Comparison of the galactic latitude distribution of the VHE $\gamma$-ray sources in the survey region with the prediction of a simple source population model assuming scale heights in the galactic disc of 30 pc (red and green curves) and 300 pc (blue curve). The sources are assumed to be mono-luminous. The curves are not normalised and give the predicted number of detected sources in each latitude bin. The legend gives the physical parameters in each case with $L_0 = 1.3 \times 10^{34}$ erg s$^{-1}$ (in the energy range 0.2 TeV to 10 TeV) as previously defined.

size as shown in Figure 4.26 (right) and was here assumed to follow:

$$F_{\rm min} \approx F_{\rm point-source} \sqrt{\sigma^2_{\rm source} + \sigma^2_{\rm PSF}}/\sigma_{\rm PSF} \tag{6.1}$$

with $\sigma_{\rm PSF} \approx 0.08^\circ$ for the analysis described here. As a consequence there is a bias in this survey against very extended sources, indeed for sources larger than the size of the ring used for background estimation ($0.7^\circ$ radius) the flux threshold increases dramatically. This effect produces a bias against close-by sources, potentially resulting in a latitude distribution narrower than that of the parent population. An additional consequence of the ring background technique is that this survey is insensitive to weak diffuse emission. A search for diffuse emission in this dataset is beyond the scope of this work.
It is apparent from Table 6.1 that the most likely associations of the $\gamma$-ray sources lie at rather large distances (i.e. 4-10 kpc) within our Galaxy, and exhibit luminosities in the range 1-7 $\times 10^{34}$ erg s$^{-1}$. The candidate SNR have implied $\gamma$-ray luminosities comparable to the well studied shell-type remnant RX J1713.7–3946 ($0.3 \times 10^{34}$ erg s$^{-1}$). The candidate PWN have somewhat higher implied luminosities, comparable to that of the likely PWN G 0.9+0.1.
As is also clear from Table 6.1 it is difficult to explain the new VHE sources as belonging to a single source population. It is therefore not straight-forward to interpret the global properties of the sources. However, conventional galactic particle accelerators such as young pulsars and SNRs have similar spatial distribution within the Galaxy. Molecular

material and hence regions of star formation, cluster rather close to the Galactic Plane, with a scale height of <100 pc (Dame & Thaddeus, 1994). $\gamma$-ray sources associated with stellar death (and birth) (SNRs, young pulsars, OB associations) should therefore follow similar distributions (see Figure 6.1). To compare such candidate populations with the measured galactic latitude distribution of the survey sources assumptions must be made about the luminosity distribution, the radial distribution in the Galaxy and the intrinsic size of the sources. A simple Monte-Carlo simulation shows that the measured $b$ distribution of sources is rather insensitive to the assumed luminosity distribution.
Taking the example case of SNRs as being a single class of counterparts to the new sources it is possible to derive the expected properties of the detected $\gamma$-ray sources. For this exercise the prescription of Drury, Aharonian, & Völk (1994) is followed for the $\gamma$-ray emission of SNRs assuming supernova explosions with fixed energy $10^{51}$ erg s$^{-1}$ occurring at a rate of 1/40 year$^{-1}$ and with a $\gamma$-ray emitting lifetime of $10^4$ years. In this case 250 $\gamma$-ray sources are expected within the galactic disc. Assuming the radial distribution of SNRs suggested by Case & Bhattacharya (1996), the measured number of the VHE $\gamma$-ray sources is consistent with expectations for plausible values of conversion efficiency $\Theta = 0.2$ and ISM density $n = 1$ cm$^{-3}$. As the sensitivity of the survey is reduced for extended sources some assumption of the intrinsic size distribution of sources must be made. Here the Sedov solution is assumed to determine the size of the $\gamma$-ray emission region for SNR, of randomly sampled age, expanding into an ISM of density $n$. Reasonable agreement with the number and angular size of the detected sources are found for $1 < n < 10$ cm$^{-3}$. Figure 6.2 (right) shows the expected distributions from this simple model for a scale height in the galactic disk of 30 pc (red curve) and 300 pc (blue curve). The green curve is as the red curve but with 4 times as many sources, each with half the luminosity, illustrating the relative insensitivity of the shape of the distribution on the assumed source luminosity distribution. The difference between the blue and the red curve illustrates that the H.E.S.S. survey has a broad enough sensitive coverage in $b$ to distinguish these two scenarios. For the 300 pc curve (blue), a intrinsic luminosity twice that of the 30 pc case has been assumed to give reasonable agreement with the number of detected sources. As can be seen from Figure 6.2 the experimental data favour a scale height for the parent population of $< 100$ pc in line with expectations for young SNR and PWN.

## 6.2 Conclusion and Outlook

Comparing the knowledge of the Milky Way in VHE $\gamma$-rays before the completion of H.E.S.S. as shown in Figure 1.8, to the results of the H.E.S.S. Galactic Plane survey as described in this work, it becomes apparent, that the survey was successful towards a better understanding of our Galaxy. The number of known galactic sources of VHE $\gamma$-radiation has more than doubled from $\sim$ 10 to 25. The $\gamma$-ray sky at present knowledge is shown in Figure 6.3.
The search for counterparts in other wavebands as described in the last section reveals no clear single population of sources but rather demonstrates that most probably more than one class of VHE $\gamma$-ray-sources exists within our Galaxy. With the microquasar LS5039 an entirely new class of objects was found to emit $\gamma$-rays. The increasing number

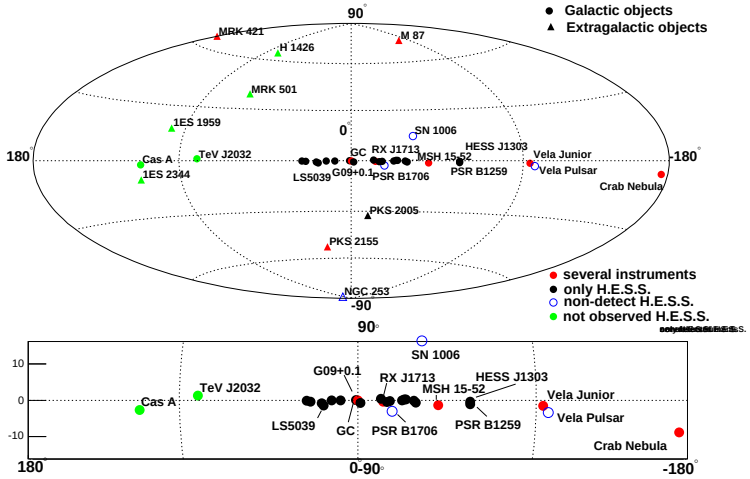


**Figure 6.3:** Known sources of VHE $\gamma$-radiation including the new H.E.S.S. sources. In the upper panel, circles denote galactic objects whereas triangles denote extra-galactic objects. The lower panel shows only Galactic sources. Objects that have not been observed by H.E.S.S. due to their location in the northern hemisphere are marked in green. Sources that have been reported by other experiments with contradicting flux upper limits from H.E.S.S. are marked in blue, sources that have been detected by several instruments are marked in red, whilst sources that are detected only by H.E.S.S. are marked in black.

of known $\gamma$-ray-emitters allows us to start to look for similarities in the properties of the different source classes. One interesting similarity of all galactic sources found in the H.E.S.S. survey is the rather hard energy spectrum in comparison to the Crab Nebula which seems to be different to the rather soft spectra found in sources of extra-galactic origin like e.g. active galactic nuclei (see here PKS 2155-304 (Aharonian et al., 2005e)) as expected due to extragalactic background light absorption. The mean of the photon index distribution of the 17 sources described here is 2.3, a value that is still comparable with expectations from models of shock wave acceleration in SNRs. Another important property of the new sources is their rather narrow latitude distribution which leads to the conclusion that they are not local objects but kiloparsecs away – presumably in the inner Galaxy. A simple Monte-Carlo simulation has shown that the latitude distribution of the detected sources appears to be consistent with a scale height in the galactic disk for the parent population of $< 100$ pc, consistent with expectations for supernova remnants and/or pulsar wind nebulae.

Although some of the new sources seem to have clear counterparts in the radio and/or X-ray waveband, it is evident that our broadband knowledge of the new sources is rather limited. More multiwavelength data is needed to draw firm conclusions about these new objects and the possible acceleration mechanisms at work. Reobservations with X-ray satellites such as *XMM-Newton* and *Chandra* are planned or proposed and will (with their high sensitivity and superior angular resolution) help to resolve any possible X-ray emission associated with the new sources. The H.E.S.S. survey has however opened a

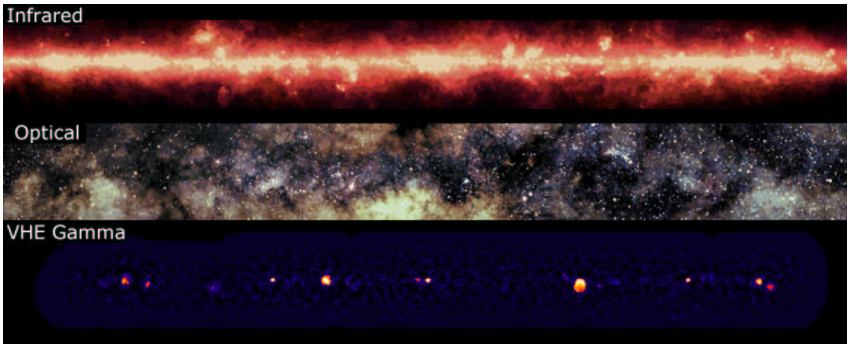


**Figure 6.4:** The central part of the Galactic Plane as seen in different wavebands between Galactic longitude +35° to -35° and Galactic latitude +4° to -4°.

new window on our Milky Way. The inner Galaxy was mapped for the first time with high sensitivity in VHE $\gamma$-rays. Figure 6.4 shows a picture of our Galaxy in the optical, the infrared and in VHE $\gamma$-rays. The top panel shows the picture of the Milky Way in the infrared as recorded by the IRAS satellite. The Galactic Plane is clearly seen as broad strip running through the middle of the picture. This infrared emission is mostly due to interstellar dust warmed by absorbed starlight. In the middle panel the optical image of the central part of our Galaxy is shown. Most of the central part of the Galaxy is hidden by the above mentioned interstellar dust. Most of this starlight is emitted by stars that are close to the solar system on the scale of the Milky way. The bottom panel shows the new picture of the Milky way as seen by H.E.S.S. in very high energy gamma-rays as presented in this work. It can be clearly seen, that most of the new sources of very high energy gamma-rays cluster along the Galactic Plane.
Follow-up observations of the new sources with H.E.S.S. are underway to gain more in-depth information on morphology and extend the energy spectra to higher energies. Also an extension of the survey to the longitude range between 300° and 330° is currently underway in 2005.

# Appendix A

# Additional Significance Maps

This section shows the two additional significance maps, generated from the Galactic survey data. Figure A.1 shows the significance map using a cut of $\theta^2 = 0.01(^\circ)^2$, optimised for point-like objects, while Figure A.2 shows the significance map using a cut of $\theta^2 = 0.1(^\circ)^2$, which is sensitive to very extended sources with respect to the PSF of the instrument. For the point-source cut an additional significant excess is apparent at the position of the microquasar LS5039 (denoted HESS J1826–148). The extended $\theta^2$ cut reveals several additional significant emission regions but the discussion of these is beyond the scope of this work.

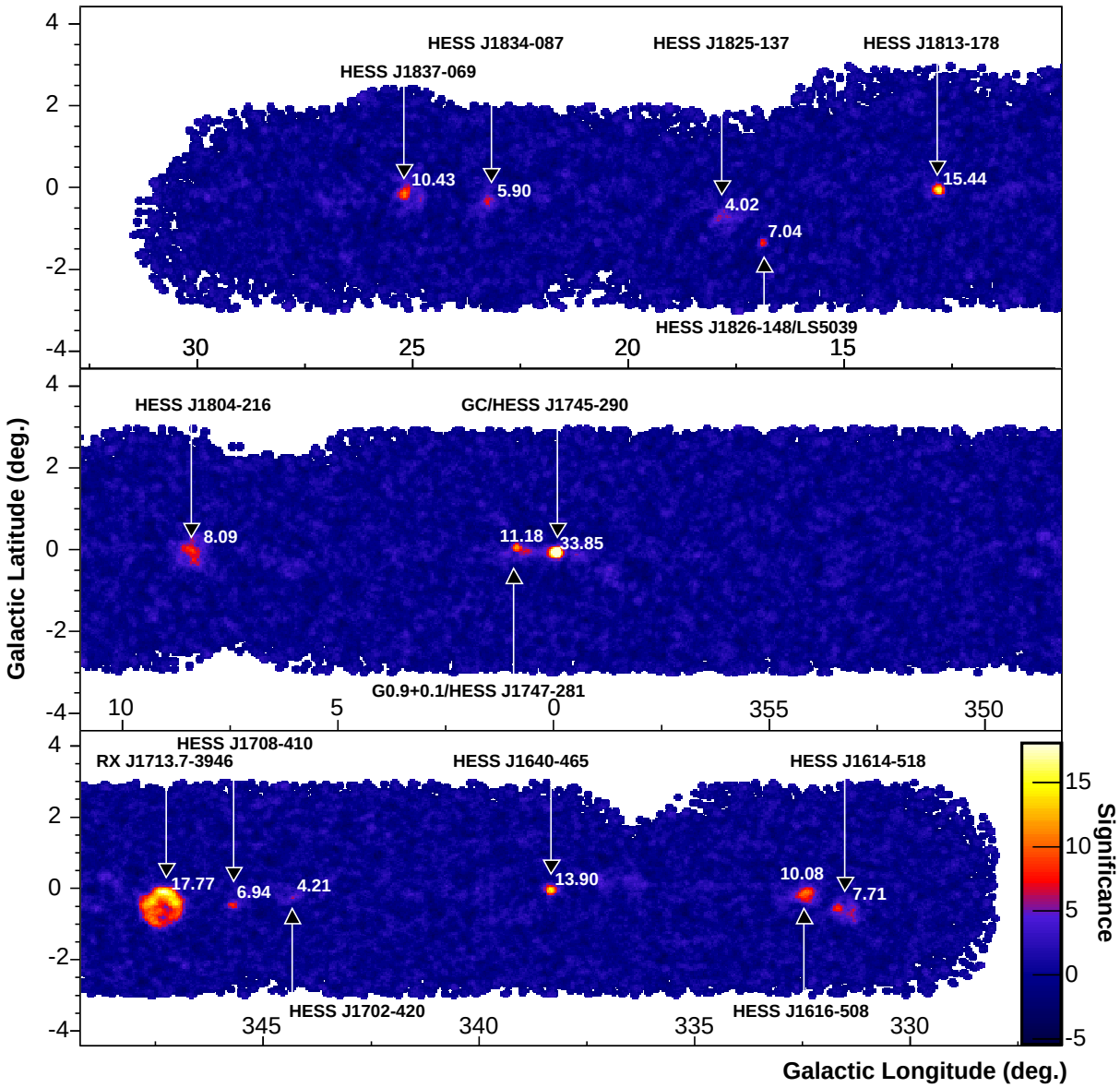


**Figure A.1:** Significance map of the H.E.S.S. Galactic Plane survey in 2004 similar to Figure 5.5, derived with a cut of $\theta^2 = 0.01(^\circ)^2$, an optimal cut for point-like sources. The labels indicate the $\gamma$-ray sources described in this work, plus the additionally detected source HESS J1826–147, which is coincident with the microquasar LS5039. Also here the significance scale is truncated at $18\sigma$, the signals from the Galactic Centre and RX J1713,7–3946 exceed this level.

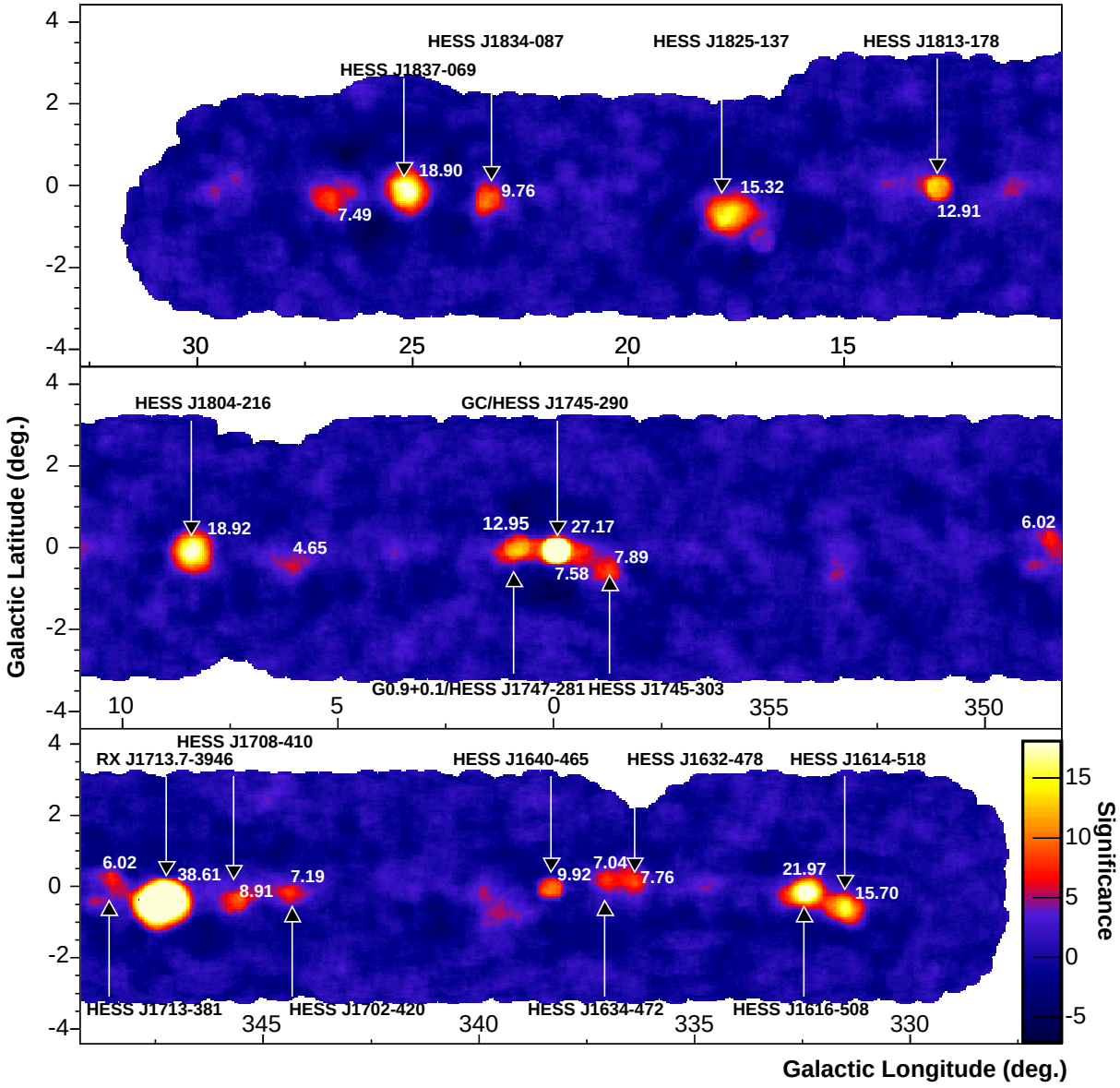


**Figure A.2:** Significance map of the H.E.S.S. Galactic Plane survey in 2004 similar to Figure 5.5, and Figure A.1 derived with a cut of $\theta^2 = 0.1(^\circ)^2$, a cut sensitive to very extended sources with respect to the PSF. The labels indicate the $\gamma$-ray sources described in this work. Also here the significance scale is truncated at $18\sigma$, the signals from the Galactic Centre and RX J1713,7–3946 exceed this level. Some additional sources are found, but a detailed discussion of this approach and the systematic problems involved is beyond the scope of this work.

# Bibliography


Aharonian, F. A., Atoyan, A. M., & Kifune, T. 1997, MNRAS, 291, 162

Aharonian, F. A., et al. 1999, A&A, 349, 11.

Aharonian, F. A., et al. 2000, ApJ, 539, 317

Aharonian, F. A., et al. 2002a, A&A, 393, L37

Aharonian, F. A., et al. 2002b, A&A, 395, 803

Aharonian, F. A. 2004, "Very high energy cosmic gamma radiation : a crucial window on the extreme Universe", River Edge, NJ: World Scientific Publishing

Aharonian, F. A., et al. (*H.E.S.S. Collaboration*) 2004a, Nature, 432, 75

Aharonian, F. A., et al. (*H.E.S.S. Collaboration*) 2004b, A&A, 425, L13

Aharonian, F. A., et al. (*H.E.S.S. Collaboration*) 2004c, APh, 22, 109

Aharonian, F. A., et al. (*H.E.S.S. Collaboration*) 2005a, A&A, submitted

Aharonian, F. A., et al. (*H.E.S.S. Collaboration*) 2005b, Science 307, 1938

Aharonian, F. A., et al. (*H.E.S.S. Collaboration*) 2005c, A&A submitted

Aharonian, F. A., et al. (*H.E.S.S. Collaboration*) 2005d, A&A 432, 29

Aharonian, F. A., et al. (*H.E.S.S. Collaboration*) 2005e, A&A 430, 865

Aharonian, F. A., et al. (*H.E.S.S. Collaboration*) 2005f, A&A, 435, L17

Aharonian, F. A., et al. (*H.E.S.S. Collaboration*) 2005g, A&A, in preparation

Aharonian, F. A., et al. (*H.E.S.S. Collaboration*) 2005h, A&A, in preparation

Amenomori, M., et al. 2002, ApJ, 580, 887

Atkins, R., et al. 2004, ApJ, 608, 680

Baganoff, F. K., et al. 2003, ApJ, 591, 891

Bamba, A., Ueno, M., Koyama, K., Yamauchi, S. 2003, ApJ, 589, 253

Baring, M. G. 2004, AdSpR, 335, 552

Bell, A. R. 1978, MNRAS, 182, 147

Berezhko, E. G., & Völk, H. J. 1997, APh, 7, 183

Berezhko, E. G., & Völk, H. J. 2000, A&A, 357, 283

Bernlöhr, K. 2000, APh, 12, 255.

Bernlöhr, K. 2001, MC images of air showers, `http://www.mpi-hd.mpg.de/hfm/~bernlohr/HESS/`

Bernlöhr, K., et al. 2003, APh, 20, 111

Bernlöhr, K. 2005, In

Bertsch, D. L., et al. 1999, in Proc. 5th Compton Symposium, Portsmouth, ed. M. L. McConnell, & J. M. Ryan,(Melville: AIP 510), 504

Blandford, R. D., & Eichler, D. 1987, PhR, 154, 1

Bolz, O., PhD thesis, 2004, Universität Heidelberg

Case, G., & Bhattacharya, D. 1996, A&AS, 120, 437

CGPS (Canadian galactic plane survey), *http://www.ras.ucalgary.ca/CGPS/where/plan/*

Cheng, K. S. 2004, AdSpR, 33, 561

Churchwell, E. 1990, A&ARv, 2, 79

Cornils, R., et al. 2003, APh, 20, 129

Dame, T. M., & Thaddeus, P. 1994, ApJ, 436, L173

Dame, T. M., Hartman, D., & Thaddeus, P. 2001, ApJ, 547, 792

Daum, A., et al. 1997, APh, 8, 1.

Davies, J. M., & Cotton, E. S. 1957, J. Solar Energy Sci. and Eng., 1, 16

Dickey, J. M., & Lockman, F. J. 1990, ARA&A, 28, 215

Drury, L. O., Aharonian, F. A., & Völk, H. J. 1994, A&A, 287, 959

Enomoto, R., et al. 2002, Nature, 416, 823

Fatuzzo, M., & Melia, F. 2003, ApJ, 596, 1035

Feinstein, F. (*ANTARES Collaboration*), NIM A, 504, 258.

Fesefeldt, H. 1985, Physikalisches Institut der Technischen Hochschule Aachen, PITHA-Report 85/02

Finley, J. P., & Ögelman, H. 1994, ApJ, 434, L25

Fleysher, R. et al. 2005, International Symposium on High-Energy Gamma-Ray Astronomy, ed. F.A. Aharonian, H.J. Völk, D. Horns, AIP Conference Proceedings 269

Franzen, A., et al. 2003, Proc. 28th ICRC (Tsukuba), Univ. Academy Press, Tokyo. p. 2987.

Funk, S., et al. 2004, APh, 22, 285

Gaensler, B. M., & Johnston, S. 1995, MNRAS, 275, L73

Gaensler, B. M., Pivovaroff, M. J., Garmire, G. P. 2001, ApJ, 556, L107

Gaensler, B. M., Schulz, N. S., Kaspi, V. M., Pivovaroff, M. J., & Becker, W. E. 2003, ApJ, 588, 441

Genzel, R., et al. 2003, Nature, 425, 934

Ginzburg, V. L., & Syrovatskii, S. I. 1963, "Origin of Cosmic Rays", Macmillan

Green, D. A. 2004, BASI, 32, 335

Harding, A.K. 1996, SSRv, 75, 257

Hall, T. A., et al. 2003, in Proc. 28th ICRC, Tsukuba, ed. T. Kajita et al., (Universal Academy Press, Tokyo, 2003), 2497

Halley, E. 1686, Philos. Trans. R. Soc. London, 16, 104

Hartman, R. C., et al., 1999, ApJS, 123, 79

Haschick, A., Ho, P. T. P. 1983, ApJ, 267, 638

Heck, D., et al. 1998, Forschungszentrum Karlsruhe Report **FZKA 6019**

Heitler, W, 1954, *Quantum Theory of Radiation*, Dover Press, 3rd edition

Helfand, D. J., & Becker, R. H. 1987, ApJ, 314, 203

Hess, V., 1912, Physik. Zeitschrift, 13

Hillas, A., 1985, Proc. 19th ICRC, La Jolla, 445

Hinton, J. A. 2004, NewAR, 48, 331

Hirotani, K. 2001, ApJ, 549, 495

Hofmann, W. 2003, APh, 20, 1

Kassim, N. E., & Weiler, K. W. 1990, Nature, 343, 146

Kassim, N. E., Baum, S. A., & Weiler, K. W. 1991, ApJ 374, 212

Kassim, N. E. 1992, AJ, 103, 943

Kastner, J. H., Balick, B., Blackman, E. G., Frank, A., Soker, N., Vrtilek, S. D., & Li, J. 2003, ApJ, 591, L37

Katagiri, H., et al. 2005, ApJ, 619, L163

Koyama, K., et al. 1995, Nature, 378, 225

Kubo, H., et al. 2004, NewAR, 48, 323

Lampeitl, H., et al. 1999, AIP Proc. GeV-TeV Gamma Ray Astrophysics Workshop (Snowbird), 515, 328 (astro-ph/9910461)

Li, T., & Ma, Y. 1983, ApJ, 272, 317

Longair, M. S., "High energy astrophysics", Vol. 2, 1994, Cambridge university press.

Lorenz, E., et al. (*MAGIC Collaboration*) 2004, NewAR, 48, 339

Maeda, Y., et al. 2002, ApJ, 570, 671

Malizia, A., et al. 2004, "From BeppoSAX to INTEGRAL: PDS observations of hard X-ray sources detected in the IBIS survey", (available at http://xxx.lanl.gov/abs/astro-ph/0404596).

Malkov, M. A., & Drury, L. O'C. 2001, Rep. Prop. Phys, 64, 429

Manchester, R. N., Hobbs, G. B., Teoh, A., & Hobbs, M. 2005, AJ, 129, 1993

Melia, F., 1992, ApJ, 387, L25

Melia, F., & Falcke, H. 2001, ARA&A, 39, 309

Mereghetti, S., Sidoli, L., & Israel, G. L. 1998, A&A, 331, L77

Mezger, P. G., Duschl, W. J., & Zylka, R. 1996, A&ARv., 7, 289

Motch, C., Haberl, Fl, Dennerl, K., Pakull, M., & Janot-Pacheco, E. 1997, A&A, 323, 853

de Naurois, M., et al. 2002, ApJ, 566, 343

Nolan, P. L., Tompkins, W. F., Grenier, I. A., & Michelson, P. F. 2003, ApJ, 597, 615

Ojeda-May, P., Kurtz, S. E., Rodriguez, L. F., Arthur, S. J., Velazquez, P. 2002, RMxAA, 38, 111

Paladini, R., Burigana, C., Davies, R. D., Maino, D., Bersanelli, M., Cappellini, B., Platania, P., & Smoot, G. 2003, A&A, 397, 213

Patel, S. K., Kouveliotou, C., Tennant, A, et al. 2004, ApJ, 602, L45

Paredes, J. M., Marti, J., Ribo, M., & Massi, M. 2000, Science 288, 2340

Preuss, S., et al. 2002, NIM A, 481, 229.

Porquet, D., Decourchelle, A., & Warwick, R. S. 2003, A&A, 401, 197

O. Reimer, in Proc. of The Nature of Unidentified Galactic High-Energy Gamma-Ray Sources, Tonantzintla 2000, Astrophysics and Space Science Library 267, 17

Reimer, O., & Bertsch, D. L., in Proc. of 27th Int. Cosmic Ray Conf., Hamburg, 2001, 2546

Revnitsev, J., Tuerler, M., DelSanto, M., Westergaard, N. J., Gehrels, N., & Winkler, C. 2003, IAUC 8097

Reynoso, E. M., & Mangum, J. G. 2000, ApJ, 545, 874

Rodriguez, J., Tomsick, J. A., Foschini, L., Walter, R., Goldwurm, A., Corbel, S., & Kaaret, P. 2003, A&A, 407, L41

Rowell, G. P., 2003, A&A, 410, 389

Sakano, M., http://heasarc.gsfc.nasa.gov/docs/asca/ao5/abs/51072.html

Schödel, R., et al. 2002, Nature, 419, 694

Sugizaki, M., Mitsuda, K., Kaneda, H., Matsuzaki, K., Yamauchi, S., & Koyama, K. 2001, ApJS, 134, 77

Smith, A. J., et al., 2005, International Symposium on High-Energy Gamma-Ray Astronomy, eds F.A. Aharonian, H.J. Völk, D. Horns, AIP Conference Proceedings 657

Tomsick, J. A., Lingelfelter, R., Walter, R., et al. 2003, IAUC, 8076

Torii, K. et al. 1998, ApJ, 494, L207

Vincent, P., et al. 2003, in Proceedings of the 28th International Cosmic Ray Conference, T. Kajita et al., Eds. (Universal Academy Press, Tokyo, 2003), 2887

Vink, J. 2004, ApJ, 604, 693

Weisskopf, M. C., O'Dell, S. L., Paerels, F., Elsner, R. F., Becker, W., Tennant, A. F., & Swartz, D. A. 2004, ApJ, 601, 1050

Weekes, T. C., et al. 1989, ApJ, 342, 379

Weekes, T. C. 2001, in Proceedings of High Energy Gamma-Ray Astronomy, International Symposium 2000, Heidelberg, Germany, F. A. Aharonian & H. J. Voelk Eds, (AIP Proceedings, 558), 15

Weekes, T. C., et al. 2002, APh, 17, 221.

Werner, K. 1993, Phys. Rep, 232, 87

Wiedner, C. A. 1998, *Site aspects of the HESS project: astronomical and visibility conditions*, unpublished, H.E.S.S. internal note

White, R. L., Becker, R. H., & Helfand, D. J. 2005, AJ, submitted (astro-ph/0501607)

Whiteoak, J. B. Z., Green, A. J. 1996, A&AS, 118, 329

Yuan, F., Quataert, E., & Narayan, R. 2003, ApJ, 598, 301

Yusef-Zadeh, F., Melia, F., & Wardle, M. 2000, Science, 287

# Acknowledgements / Danksagung

An dieser Stelle möchte ich noch den zahlreichen Helfern danken, die mich beim Entstehen dieser Arbeit auf unterschiedlichste Weise unterstützt haben. Einige, die einen besonders grossen Teil zum Gelingen beigetragen haben, möchte ich im Folgenden namentlich erwähnen.

- Professor Werner Hofmann möchte ich für die Freiräume danken, die er mir gewährt hat, für die Annahme als Doktorand bei H.E.S.S., für das interessante Thema meiner Arbeit, für die Begeisterung für die $\gamma$-Astronomie, die er in mir geweckt hat, sowie für die hilfreichen Ideen in Bezug auf meine Analysen.

- Jim Hinton möchte ich danken für die gute Zusammenarbeit in Heidelberg und Namibia (sogar beim Kochen), für die entspannten Gespräche beim Runterlaufen, für die Hilfe beim Scan Paper mit Latte Macchiato im Star Coffee und für die Unterstützung während meiner Promotion.

- bedanken möchte ich mich auch bei der H.E.S.S.-Gruppe am Max-Planck Institut für Kernphysik in Heidelberg. German Hermann war jederzeit bereit mich zu unterstützen (Pulse-Width encoding war doch eine gute Idee) und war ein guter Mini-Chef der Trigger Crew. Die Diskussionen mit Felix Aharonian waren immer sehr anregend und interessant. Für die gute Zusammenarbeit in Heidelberg möchte ich mich ausserdem bei Conor Masterson, Wystan Benbow, Bruno Khelifi, Oliver Bolz, Gavin Rowell und allen anderen Mitgliedern der H.E.S.S. Gruppe bedanken.

- auch die intensive Zusammenarbeit innerhalb der H.E.S.S. Collaboration war sehr fruchtbar. Insbesondere der Berliner Gruppe um Thomas Lohse, Christian Stegmann und Stefan Schlenker möchte ich hier danken, die mir während der Einbindung des zentralen Triggers in die H.E.S.S.-Daq hilfeich zur Seite standen.

- David Berge möchte ich für seine Freundschaft danken und für die vielen interessanten und schönen Stunden, die wir während der Promotion miteinander verbracht haben. Ebenso danke ich allen meinen Freunden, die mir die Zeit neben der Arbeit angenehm gemacht haben, meinem Bruder Sebastian, Torsten und Michi, Tariq, meiner Fussball-Crew, Magali und Gero und allen anderen.

- meinen Eltern Margot und Werner danke ich dafuer, dass sie mich seit ich denken kann immer in allem unterstützt haben, was mir wichtig war, dass sie mir bei Problemen zur Seite standen und dass ich bei ihnen immer ein offenes Ohr fand.

- und natürlich gilt mein besonderer Dank Jimena, die mir mein Leben vergoldet. Ich danke ihr für ihre wertvolle Freundschaft, für ihr Vertrauen und ihr Verständnis, dafür, dass sie immer für mich da war (f.j.w.).